

SMC Bulletin

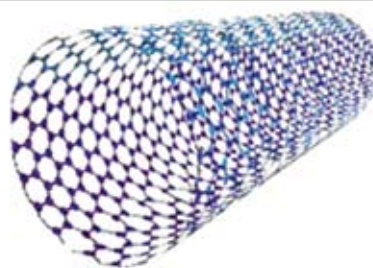
A Publication of the Society for Materials Chemistry

Volume 4

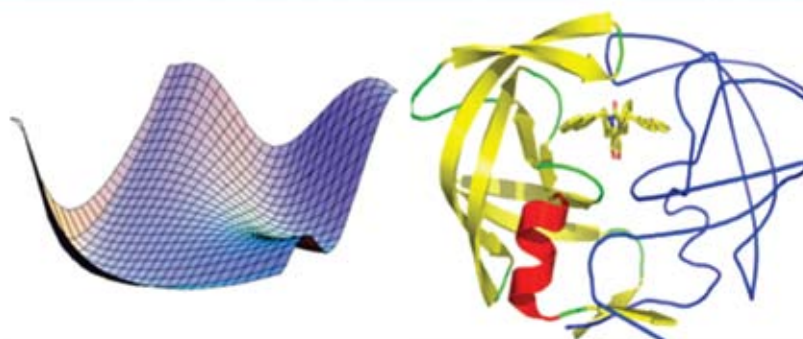
No. 2

August 2013

$$i\hbar \frac{\partial}{\partial t} \Psi = \hat{H} \Psi$$



Computational Materials Chemistry



Society for Materials Chemistry

Society for Materials Chemistry was mooted in 2007 with following aims and objectives:

- (a) to help the advancement, dissemination and application of the knowledge in the field of materials chemistry,
- (b) to promote active interaction among all material scientists, bodies, institutions and industries interested in achieving the advancement, dissemination and application of the knowledge of materials chemistry,
- (c) to disseminate information in the field of materials chemistry by publication of bulletins, reports, newsletters, journals.
- (d) to provide a common platform to young researchers and active scientists by arranging seminars, lectures, workshops, conferences on current research topics in the area of materials chemistry,
- (e) to provide financial and other assistance to needy deserving researchers for participation to present their work in symposia, conference, etc.
- (f) to provide an incentive by way of cash awards to researchers for best thesis, best paper published in journal/national/international conferences for the advancement of materials chemistry,
- (g) to undertake and execute all other acts as mentioned in the constitution of SMC.

Executive Committee

President

Dr. S. K. Sarkar

Bhabha Atomic Research Centre
Trombay, Mumbai, 400 085
sarkarsk@barc.gov.in

Vice-Presidents

Dr. V. K. Jain

Bhabha Atomic Research Centre
Trombay, Mumbai, 400 085
jainvk@barc.gov.in

Prof. Sandeep Verma

Indian Institute of Technology
Kanpur
sverma@iitk.ac.in

Secretary

Dr. P. A. Hassan

Bhabha Atomic Research Centre
Trombay, Mumbai, 400 085
hassan@barc.gov.in

Treasurer

Dr. Sandeep Nigam

Bhabha Atomic Research Centre
Trombay, Mumbai, 400 085
snigam@barc.gov.in

Members

Dr. K. Ananthasivan

Indira Gandhi Centre for Atomic Research
Kalpakkam, 603102

Dr. (Smt.) A. Banerjee

Bhabha Atomic Research Centre
Trombay, Mumbai-400085

Dr. K. Bhattacharya

Bhabha Atomic Research Centre
Trombay, Mumbai-400085

Dr. D. Das

Bhabha Atomic Research Centre
Trombay, Mumbai-400085

Dr. G. K. Dey

Bhabha Atomic Research Centre
Trombay, Mumbai-400085

Dr. P. Sujata Devi

CSIR Central Glass & Ceramic Research
Institute, Kolkata-700032

Dr. C. P. Kaushik

Bhabha Atomic Research Centre
Trombay, Mumbai-400085

Dr. T. Mukherjee

Bhabha Atomic Research Centre
Trombay, Mumbai-400085

Dr. M. C. Rath

Bhabha Atomic Research Centre
Trombay, Mumbai-400085

Dr. (Smt.) S. S. Rayalu

CSIR National Environmental
Engineering Research Institute, Nagapur

Prof. S. D. Samant

Institute of Chemical Technology
Mumbai

Dr. A. K. Tyagi

Bhabha Atomic Research Centre
Trombay, Mumbai-400085

Dr. R. K. Vatsa

Bhabha Atomic Research Centre
Trombay, Mumbai-400085

Co-opted Members

Prof. A. Ajayaghosh

CSIR – National Institute for
Interdisciplinary Science and Technology
Thiruvananthapuram
ajayaghosh@niist.res.in

Prof. A. K. Ganguli

Director, Institute for Nanoscience and
Technology
ashok@chemistry.iitd.ernet.in

Prof. S. Ram

Indian Institute of Technology - Kharagpur
sram @ matsc.iitkgp.ernet.in

Dr. A. K. Tripathi

Bhabha Atomic Research Centre
Trombay, Mumbai-400085
catal@barc.gov.in

Contact address

Society for Materials Chemistry

C/o Chemistry Division

Bhabha Atomic Research Centre, Trombay, Mumbai, 400 085, India

Tel: +91-22-25592001, E-mail: socmatchem@gmail.com

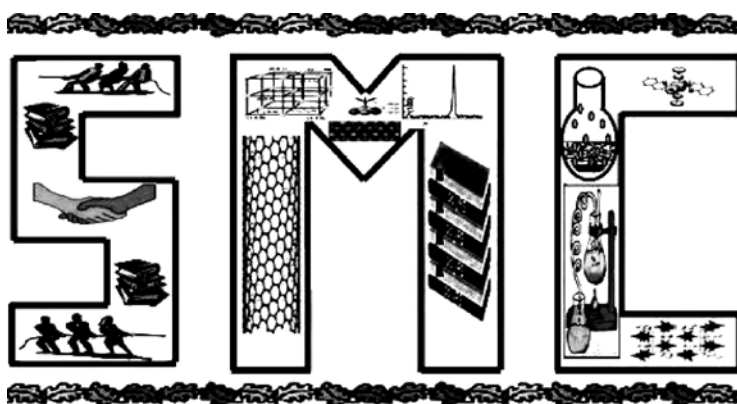
SMC Bulletin

A Publication of the Society for Materials Chemistry

Volume 4

No. 2

August 2013



SOCIETY FOR MATERIALS CHEMISTRY

SMC Bulletin

Vol. 4

No. 2

August 2013

Guest Editors

Dr. Chiranjib Majumder
Chemistry Division
Bhabha Atomic Research Centre
Trombay, Mumbai, 400 085
e-mail: chimaju@barc.gov.in

Dr. Chandra Nath Patra
Theoretical Chemistry Section
Bhabha Atomic Research Centre
Trombay, Mumbai, 400 085
e-mail: chandra@barc.gov.in

Editorial Board

Dr. Arvind Kumar Tripathi
Chemistry Division
Bhabha Atomic Research Centre
Trombay, Mumbai, 400 085
e-mail: catal@barc.gov.in

Dr. Shyamala Bharadwaj
Chemistry Division
Bhabha Atomic Research Centre
Trombay, Mumbai, 400 085
e-mail: shyamala@barc.gov.in

Dr. Manidipa Basu
Chemistry Division
Bhabha Atomic Research Centre
Trombay, Mumbai, 400 085
e-mail: deepa@barc.gov.in

Dr. Aparna Banerjee
Product Development Division
Bhabha Atomic Research Centre
Trombay, Mumbai, 400 085
e-mail: aparnab@barc.gov.in

Dr. Sandeep Nigam
Chemistry Division
Bhabha Atomic Research Centre
Trombay, Mumbai, 400 085
e-mail: snigam@barc.gov.in

Published by

Society for Materials Chemistry
C/o. Chemistry Division
Bhabha Atomic Research Centre, Trombay, Mumbai, 400 085
E-mail: socmatchem@gmail.com,
Tel: +91-22-25592001

Please note that the authors of the paper are alone responsible for the technical contents of papers and references cited therein



Dr. S. K. Ghosh

Swapan Kumar Ghosh received his B.Sc. (Honours) and M.Sc. Degrees from the University of Burdwan, West Bengal. He served as a lecturer in Balurghat College for a year and then joined Bhabha Atomic Research Centre (BARC), Bombay, first as a Trainee and then as Scientific Officer in the year 1976. He did his PhD in 1982 from Indian Institute of Technology (IIT), Bombay under the supervision of Prof. B. M. Deb. He then spent two years (1984-85) at the University of North Carolina, Chapel Hill, working with Robert G Parr. He presently heads the Theoretical Chemistry Section at BARC, Mumbai. He is also a senior Professor and Dean-Academic (BARC), Chemical Sciences at the Homi Bhabha National Institute, Mumbai, and an adjunct Professor at the University of Mumbai-DAE Centre of Excellence for Basic Sciences, Mumbai.

The research work of Dr Ghosh has been in diverse areas of theoretical chemistry encompassing quantum chemistry, soft condensed matter physics and computational materials science. He has made significant contribution to the formulation of quantum chemistry in three-dimensional space using single-particle density quantities as basic variables; developed density functional theory (DFT) for time-dependent many-electron systems involving arbitrary electric and magnetic fields, and provided simpler routes to the direct calculation of electron density and response properties. He has generalized the concepts of electronegativity and chemical hardness, providing a new unified formulation for describing both covalent and ionic binding in molecular systems. He developed a thermodynamic picture of the electron cloud strengthening the foundation of several important chemical concepts that lead to better understanding of chemical binding and reactivity. His work on the DFT of macroscopic systems covers the structure of soft matter under confinement at interfaces and pores, leading to an inhomogeneous density distribution. His contributions to the development of new density functional approaches for inhomogeneous fluids, and their application to the structure of electrical double layer, solvation forces, ordering in colloidal suspensions, and adsorption of fluids in porous material are quite significant.

He has also contributed towards a new mode coupling theory and universal scaling laws for diffusivity in fluid mixtures; dynamics of flexible polymer chains; fluid flow through nanotubes; DFT of homogeneous as well as heterogeneous nucleation, etc. He has also developed a unified approach to describe the dynamics of different types of non-equilibrium processes in condensed phase encompassing reactive as well as nonreactive systems and also a novel mathematical technique to solve the Smoluchowski equation for arbitrary potential with a generalized sink. His current research interest revolves around computational design of energy related materials. He is actively involved in the design of novel materials for hydrogen storage and nuclear waste management.

In essence, his work has provided a single unified framework for theoretical description of many-particle systems (quantum as well as classical) within a single-particle picture, thus broadening the applicability of the density concept to the domain of multiscale materials modelling (involving microscopic, mesoscopic and macroscopic length scales). His work has unified, interlinked and strengthened several diverse approaches in the theory of structure and dynamics, aiming at a common unified view of the microscopic and macroscopic world.

Dr. Ghosh is deeply involved in educational and teaching activities. He has been the Delegation Leader of the Indian team, at the International Chemistry Olympiad in Athens, Greece (2003) and Kiel, Germany (2004). He has organized national symposia on 'Theoretical chemistry' and 'Materials modelling at different length scales', and has taught at BARC Training School for almost 25 years and also at the UM-DAE-Centre of Excellence in Basic Research since its inception. He has mentored a number of students including several PhDs.

Dr Ghosh is a Fellow of the Indian Academy of Sciences, Bangalore; Indian National Science Academy, New Delhi; National Academy of Sciences (India), Allahabad; Maharashtra Academy of Sciences; and the Third World Academy of Sciences, Trieste (TWAS). He has been awarded the TWAS Prize in Chemistry, Silver Medal of the Chemical Research Society of India (of which he is currently one of the Vice Presidents), AV Rama Rao Prize of Jawaharlal Nehru Centre for Advanced Scientific Research, Bangalore, Jagdish Shankar Memorial Lecture Award of INSA and J.C. Bose National Fellowship of DST.

Guest Editorial



Chiranjib Majumder



Chandra Nath Patra

It gives us immense pleasure to edit this special issue of SMC bulletin on “Computational Materials Chemistry”, in the honor of Dr. Swapan K. Ghosh, a theoretical chemist of its own repute, for his seminal contribution in this specific area. The classical concept of ‘Chemistry: An Experimental Science’ has taken a new shape with the emergence of computational chemistry, where theoretical and experimental research go hand-in-hand. Computational chemistry is a rapidly growing field in chemistry and the boundaries of the field are constantly becoming seamless, due to the advent of fast computers along with the development of smart algorithms. Computational chemistry has been viewed as a robust way to investigate the structure and properties of materials that are beyond the capacity of regular experimental conditions. It also helps chemists make predictions before running the actual experiments so that they can be better prepared for making observations. Proposing new experiments, guided by theoretical insight, also constitute a valuable component of research in computational chemistry. Currently, there are two ways to approach chemistry problems: (i) development of new formalism through analytical expressions, and (ii) numerical simulations that can deal with large systems; however, these two are interconnected quite well that led to ingenious amalgamation to several sophisticated theories.

This special issue is a collection of seven articles contributed by distinguished experts in their respective field. This issue is mainly focused on the typical behavior of materials in the gas, liquid and solid phases. The gas phase studies described the fundamental understanding of the quantum size effects on the equilibrium geometries and electronic properties of small molecular clusters along with development of methodologies for the photo-detachment spectroscopy of small clusters. One article has been dedicated to illustrate the dynamical behavior of the structure and properties of methanol in its normal liquid and supercritical states. The description of solid state has been represented in the articles for the effect of organic molecules adsorption on two-dimensional layered structure and phase stability and phase transformations of alloys. The formalism based computational chemistry is presented in the formulation to map the Non-equilibrium processes in Multi-dimensional space onto one dimensional system. The new generation technology based on computational materials science on Genome to Drug Software Initiative has been dedicated towards the simulation of biological systems.

We take this opportunity to thank all the contributors who have spared their valuable time to provide such informative articles for the benefit of all our readers. We also thank the editorial committee of SMC bulletin for inviting us to be guest editors for this special issue. We hope the readers would find this issue interesting and useful.

The next issue of the bulletin will be on the theme of “Catalytic Materials”. We request all our members to come forward and contribute their theme-based articles to this forthcoming issue.

(Chiranjib Majumder and Chandra Nath Patra)

From the desks of the President and Secretary



Dr. Sisir K Sarkar
President



Dr. P. A. Hassan
Secretary

Dear Fellow Members,

Greetings from the new Executive Council of Society for Materials Chemistry (SMC). The present council has taken over the mantle of showcasing the activity of the society on 18th April, 2013 for the next three years. As all of you know that SMC provides a platform to young researchers and active scientists in the area of Materials Chemistry by arranging symposia, workshops and publishing a scientific Bulletin. Last year we have successfully organized the 4th biennial "Interdisciplinary Symposium on Materials Chemistry (ISMC-2012)", at BARC, Mumbai.

Presently preparations are in full swing for organizing the second DAE-BRNS National Workshop on Materials Chemistry focused on Catalytic Materials, NWMC-2013 (CAT-MAT), during 22-23 November, 2013 at the Training School Hostel, Anushaktinagar, Mumbai. This workshop will cover both fundamental and applied aspects namely heterogeneous, homogeneous and enzymatic catalysis related to energy, environment, synthesis, sensors, etc. About 150 young researchers working in the field of chemistry, physics and materials science from BARC as well as other units of DAE, National laboratories, and Institutes/Universities, will be immensely benefited.

Since inception SMC has embarked on bringing out theme-based bulletin issues which serve as a platform to highlight the advances made in the field of materials chemistry and also encourage young researchers / academicians to join our fast growing society already having more than 700 life members. It is really gratifying to note that the present Guest Editors Dr. C. Majumder and Dr. C.N. Patra have taken initiative to bring out this issue on highly relevant area of Computational Materials Chemistry.

Computational materials chemistry is the study of chemical properties of materials using theoretical approaches. Computational methods used include ab initio molecular orbital theory, density functional theory, quantum chemical/classical hybrids, quantum dynamics to investigate structures, energetic, and dynamics of materials. Recent advances in computational techniques and computer technology have significantly enhanced the potential contributions that simulation and modeling can make to materials chemistry research.

The knowledge gained from these types of computational studies is used to help understand the effect of chemical reactivity on the behavior of materials and to help design new materials with novel or improved properties. It underpins technological applications in areas such as reactors, fuel cells, batteries, catalysis, membranes, environmental chemistry, and electronics. Recently, computational chemistry has been playing an important role in the emerging field of nanoscale materials. From breakthrough computer chips to new alloys for automobile engines, advances in materials shape our day-to-day lives and drive economic growth. For us at atomic energy establishment, predicting the performance of advanced materials is essential to success in countless research programmes in national security, energy, lasers and biotechnology.

Innovation in the chemical sciences - particularly starting at the level of basic research - is complex, often involving multiple interfaces with many more areas of science and technology. In today's environment multidisciplinary teams need to work in concert such that the real-time exchange of ideas, issues, and solutions results in concurrent development of multifaceted technologies. By using multiscale modeling that cover the full range of length from nanometers to meters and time scales from trillionths of a second to tens of years, scientists can now simulate the evolution of mechanical and chemical changes in materials. Such changes may start with a defect occurring in a metal's crystalline lattice over a few nanometers in length and in a trillionth of a second. And yet, multiplied millions of times over several years, such defects may combine to cause catastrophic failure of a computer chip, a glass optic, or a reactor pressure vessel.

Finally we want to acknowledge the individual and collective contributions of the authors and editors of this issue. They represent an admirable group of busy but unselfish professionals volunteering their limited time tending to the scientific "commons" on which we all depend. We wish to express our gratitude to each and every members of SMC for their unstinted support and cooperation in the growth of the society.

(Dr. Sisir K Sarkar and Dr. P. A. Hassan)

CONTENTS

Feature articles	Page No.
1. Organic Molecules Adsorption on Single Layer MoS₂: A Theoretical Study <i>Arkamita Bandyopadhyay and Swapan K Pati</i>	1
2. A theoretical account of the photodetachment spectroscopy of anionic boron clusters <i>S. Rajagopala Reddy and S. Mahapatra</i>	5
3. Methanol in its normal liquid and supercritical states: Changes of polarity and hydrogen bonding from firstprinciples simulations <i>Vivek Kumar Yadav and Amalendu Chandra</i>	15
4. Ab initio Molecular Dynamics and DFT studies on (HF)_n [n= 2 - 10] clusters <i>Sukanta Mondal, Sudip Pan and Pratim Kumar Chattaraj</i>	19
5. First-Principles Studies of Phase Stability and Phase Transformations in Alloys <i>Ashok K. Arya</i>	26
6. Genome to Drug Software Initiatives <i>Shashank Shekhar, B. Jayaram</i>	35
7. Mapping the Non-equilibrium processes in Multi-dimensional space onto one dimensional : A Projection Operator Formulation <i>Aniket Patra and Alok Samanta</i>	44
Honours and Awards	48

Organic Molecules Adsorption on Single Layer MoS₂: A Theoretical Study

Arkamita Bandyopadhyay^a, and Swapan K Pati^{a, b}

^aNew Chemistry Unit, ^bTheoretical Sciences Unit, Jawaharlal Nehru Centre for Advanced Scientific Research, Jakkur P.O., Bangalore – 560064, India.

Abstract

We have performed *ab initio* density functional theory (DFT) calculations of single layer MoS₂ and organic molecule-MoS₂ adsorbate systems to find out the changes in the electronic properties of single layer MoS₂. We have performed our calculations for Tetracyanoquinodimethane (TCNQ), Tetracyanoethylene (TCNE) and Tetrathiafulvalene (TTF). We have found that all the molecules are physisorbed on MoS₂ due to the π -stacking interactions. Our calculations show that, there is no significant charge transfer present in case of TCNQ and TCNE and a small but finite amount of charge transfer occurs in case of TTF-MoS₂ system. We find the presence of discrete molecular level near Fermi energy and thus a change in the electronic properties of single layer MoS₂.

Introduction

Because of their possible applications in nanodevices, recently, pure two dimensional (2-D) crystals like graphene, transition metal-dichalcogenites (MoS₂, WS₂, VS₂ etc.), Si or Ge 2-D sheets and boron-nitride sheet have become interesting subjects to study.[1-9] Among the above mentioned materials, a widely studied two dimensional material is graphene: a zero band-gap semiconductor or a semi-metal.[2] Thus, doping on graphene,[10, 11] reducing the dimensionality (1-D or 0-D),[12-14] molecular charge transfer[15-18], defect induced opening of band-gap [19, 20] or combination of all these processes[21, 22] have been well studied to use graphene in opto-electronic devices.

However, single layer Molybdenum di Sulfide (MoS₂) can be used in the field of electronics without any modifications as they are intrinsic semiconductors similar to their bulk three dimensional (3 D) counterpart and also they have high carrier mobility.[4, 5, 23, 24] Also, single layer MoS₂ is easy to fabricate and can be used in different devices. [23-30] Thus from these studies, one can easily predict that modification of band-gap of these systems can make them more versatile towards different device applications and the change in Fermi energy can detect whether they are compatible with a device or not.[31] Previously, many studies, namely, doping metal and non-metal adatoms or different molecules on MoS₂ electron beam mediated creation of vacancies and adding impurity atoms to these vacancies have been shown to modify the electronic properties of single layer MoS₂. [32-37] Herein, we have studied a simple method to tune the electronic properties of single layer MoS₂ by adsorbing organic molecules over MoS₂. Previously, different types of organic molecules (such as thiophene, benzothiophene, benzene, naphthalene, pyridine, quinoline etc.) were deposited on

MoS₂ to study the adsorption energies of these systems.[38, 39] Here, we have selected three molecules for our study, Tetracyanoquinodimethane (TCNQ), Tetracyanoethylene (TCNE) and Tetrathiafulvalene (TTF), where the first two are electron acceptors, while the last molecule is an electron donor. TCNQ and TCNE are electron acceptors because of the presence of 4 cyano groups and TTF is an electron donor molecule because of the presence of S lone pairs of electrons. From our study, we can suggest that all the three molecules get physisorbed on the single layer MoS₂ via van der Waals interactions. Also, we have calculated the charge transfer interactions and analyzed the reasons for the modification of the band-gap of MoS₂ single layer.

Computational Details:

In the present study, first-principle calculations have been performed, to obtain all the electronic properties of the systems, using the density functional theory (DFT) method as implemented in the SIESTA package.[40] Generalized gradient approximation (GGA) in the Perdew–Burke–Ernzerhof (PBE) form[41] has been contemplated for accounting the exchange-correlation function. Double ζ polarized (DZP) numerical atomic-orbital basis sets have been used for Mo, S, C, N and H atoms. Norm-conserving pseudo-potentials[42] are considered for Mo, S, C, N and H, respectively in the fully nonlocal Kleinman–Bylander form. [43] A mesh cut-off of 400 Ry is used for the grid integration to represent the charge density. All the structures are considered to be optimized if the magnitude of the forces acting on all atoms is less than 0.04 eV/Å. We have sampled the Brillouin zone by 5 × 5 × 1 k-points using the Monkhorst-Pack scheme for structural optimization. For electronic property calculations, we have used 10 × 10 × 1 k-points. Periodic boundary condition and the supercell approximation are taken in such a way so that the distance

between an adsorbate molecule and its periodic image is more than 10 Å so that any interactions between adsorbates can be avoided.

Results and Discussion

The molecules those we have considered are shown in Figure 1. We have considered our MoS₂ layer to be nonmagnetic as suggested earlier.[32] In order to figure out the relative stabilities of the systems, we have calculated the adsorption energies of the molecules on MoS₂. By this, we have found that all the molecules are physisorbed on the MoS₂ layer. We have calculated the adsorption energy using the following equation,[15]

$$\Delta E_{\text{adsorption}} = E_{\text{molecule+MoS}_2} - E_{\text{MoS}_2} - E_{\text{molecule}} \quad (2.1)$$

where $\Delta E_{\text{adsorption}}$, $E_{\text{molecule+MoS}_2}$, E_{MoS_2} and E_{molecule} are the adsorption energies, total energies of the optimized molecule-MoS₂ systems, total energy of the MoS₂ layer and total energies of the adsorbate molecules, respectively.

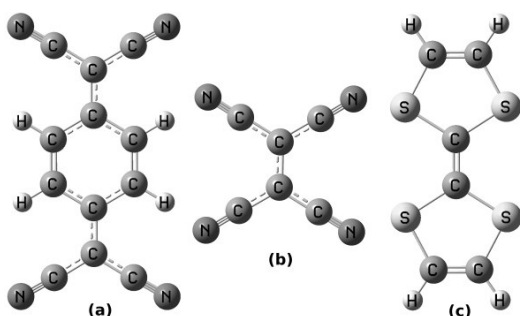


Figure 1: Molecular structure of (a) Tetracyanoquinodimethane (TCNQ) (b) Tetracyanoethylene (TCNE) and (c) Tetrathiafulvalene (TTF) molecules.

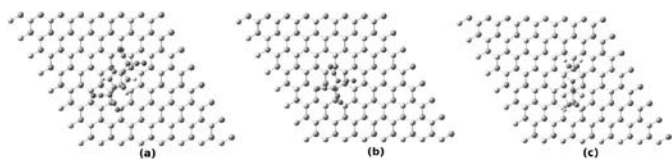


Figure 2: Optimized geometries of (a) TCNQ (b) TCNE (c) TTF on MoS₂ single layer.

From the optimized structures (as given in Figure 2), we find that TCNQ molecule is adsorbed on the MoS₂ layer at about 3.17 Å above the layer. Similarly, TCNE and TTF molecules are stable at distances of 3.12 Å and 3.42 Å, respectively. Also, we find that, all the molecules are almost parallel on the upper sulfur surface of the single layer MoS₂ (figure 3).

There is no chemical bond formation between the molecules and the MoS₂ layer as the distance between them is too long to form a chemical bond. The physisorbed molecules are stable because of the van der Waals

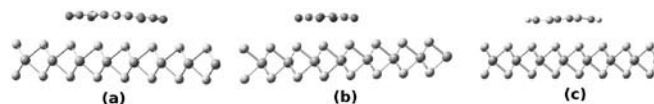


Figure 3: Side-view of (a) TCNQ (b) TCNE (c) TTF molecules on MoS₂ single layer.

interactions, also for TTF, π - π interaction is present between the molecules and the MoS₂ layer. In fact, the adsorption energy values also prove the same. We find that TCNQ has the highest adsorption energy (most stable) on MoS₂ and TCNE has the lowest adsorption energy (least stable). This trend is analogous to the molecular surface area of TCNQ, TCNE and TTF, which varies in the order: TCNQ > TTF > TCNE (as can be seen in figure 1). So it is apparent that larger the surface area, more stable is the molecule on MoS₂ layer, in contrast to graphene, where π -stacking and charge transfer interaction gives the stability to the system.[15] To make this point clear, we have done the Mülliken population analysis and have found out that there is a negligible amount of electron transfer (0.02 e and 0.04 e respectively) from the S atoms of MoS₂ layer to TCNQ and TCNE (as these molecules are electron acceptors), respectively. In fact, there is relatively higher amount of electron transfer (0.14 e) from TTF to the MoS₂ layer. This happens because MoS₂ is a p-type semiconductor. Also, same trend was observed experimentally. [36] We have investigated the effect of concentration of adsorbed molecules on the MoS₂ layer and have found that in case of TCNE and TCNQ, the change of concentration does not change the charge transfer in any significant amount, but in case of TTF when we decreased the size of the supercell size from 192 atoms to 96 atoms, charge transfer increases by a small amount (from 0.14 e to 0.22 e) but the system becomes unstable (due to adsorption energy). This is because of the steric repulsion between the molecules. But further increase in supercell size from our original 192 atoms containing supercell to 288 atoms containing supercell, charge transfer does not change.

In Table 1, we have given all the data for the MoS₂-molecule systems.

Table 1: Adsorption energies, distances and charge transfers between the molecules and single layer MoS₂. In case of TTF, the data correspond to 96/192/288 atoms containing supercells (we have not given data for other systems as there are no significant changes in charge transfer).

Molecule	$\Delta E_{\text{adsorption}}$ (eV)	Distance (Å)	Charge Transfer (e)
TCNQ	-1.76	3.17	-0.02
TCNE	-1.09	3.12	-0.04
TTF	-1.27/-1.42/-1.6	3.47/3.42 /3.42	+0.22/+0.14 /+0.14

In order to find the effects of charge transfer in the electronic properties of the MoS₂ layer, we plotted the band structure, Density of States (DOS), as well as projected Density of States (pDOS) of the pure single layer MoS₂ and the MoS₂-molecule adsorbed systems. We find that MoS₂ has a direct band-gap of 1.809 eV (which is comparable with previous results [5, 23]) at high symmetry K point (0.667, 0.333, 0.000) which does not change much upon adsorption of TCNQ and TCNE (1.81 and 1.807 eV). But, a localized molecular state appears above the Fermi level because of the electron deficient nature of TCNQ and TCNE. In the case of TTF, adsorption on the layer, the band gap of MoS₂ is about 1.804 eV. In this case, one localized molecular level appears below the Fermi level. So, these levels change the band-gap of the composite systems. From the plot of the total density of states, Mo and S atoms' contributions to the DOS and the Mo *d*-orbital and S *p*-orbital contributions to the DOS (see Figure 4), it is clear that near the Fermi level Mo *d*-orbital contribution is maximum.[5] From the figure, it is evident that in all the composite systems, there is a localized molecular level present and the level does not have any contribution from the MoS₂ sheet.

Fermi levels of the systems also have been shifted from the pure MoS₂ layer (-3.45 eV); -4.41 eV and -4.42 eV for TCNQ and TCNE adsorption, while it shifts to -3 eV for the TTF adsorption. This clearly suggests that electron donor molecule can shift the Fermi level up to higher energy by electron donation and electron acceptor molecules can shift the Fermi level down to lower energy value.

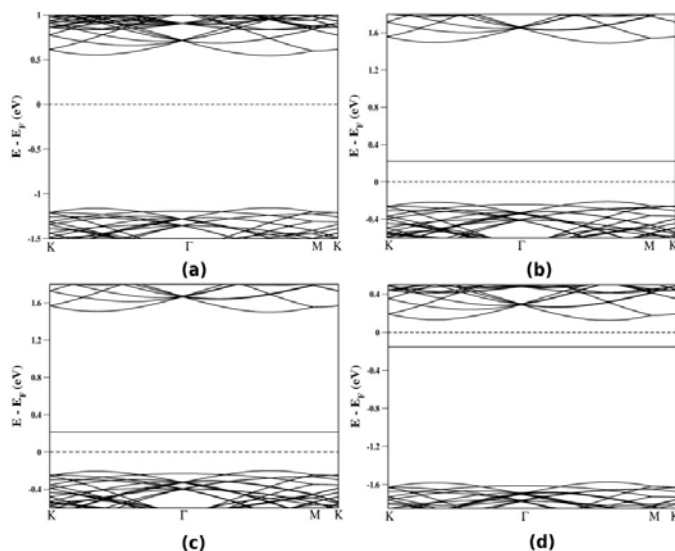


Figure 4: Band structure plots of (a) single layer MoS₂, (b) MoS₂-TCNQ, (c) MoS₂-TCNE and (d) MoS₂-TTF. The straight line corresponds to the mid-gap molecular level. The Fermi level is set to zero the K, M and Γ point have the coordinates (0.667, 0.333, 0.000), (0.5, 0.5, 0.5) and (0.0, 0.0, 0.0) respectively.

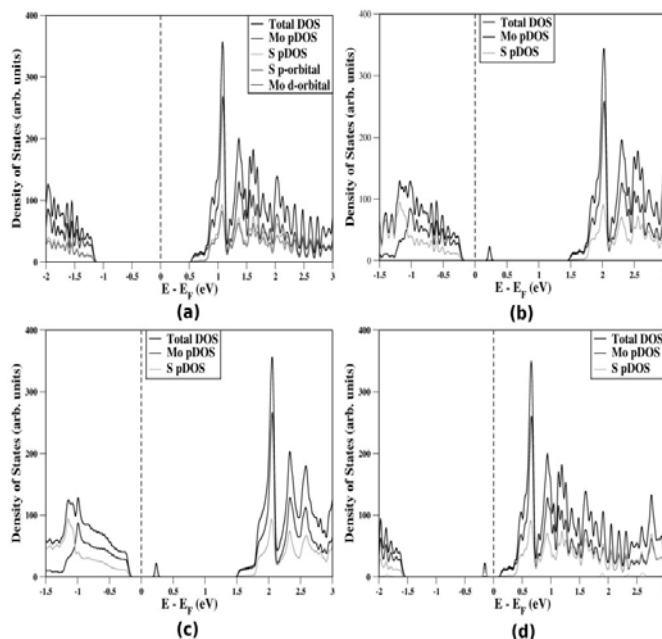


Figure 5: pDOS plots of (a) single layer MoS₂, (b) MoS₂-TCNQ, (c) MoS₂-TCNE and (d) MoS₂-TTF. The Fermi level is set to zero. The Gaussian broadening parameter used is 0.025 eV.

Conclusion

In this study, we have shown that organic donor molecule (TTF) and acceptor molecules (TCNQ and TCNE) can add extra holes and electrons, respectively, to the MoS₂ single layer and as a consequence can modify the electronic properties of the single layer MoS₂. We find that all the composite systems are stable as they have negative adsorption energies and the molecules are physisorbed on the MoS₂ layer. The physisorbed molecules are stable because of the van der Waals and π π - $d\pi$ interactions between the molecules and the MoS₂ layer. Our Mulliken population analysis shows that, when the adsorbed molecule is an electron-donor then there is a small amount of charge transfer from the molecule to MoS₂. Band structure, DOS and pDOS plots evidently showed that there is a presence of isolated localized energy level near the Fermi-energy, which arise from the adsorbed molecule. In case of TCNQ and TCNE, this localized energy level is the acceptor level above the Fermi-energy, and in the case of TTF, it is the donor level below the Fermi-energy.

References:

- Novoselov, K., A. Geim, S. Morozov, D. Jiang, Y. Zhang, S. Dubonos, I. Grigorieva, and A. Firsov, *Science*, 306(2004) 666.
- Geim, A.K. and K.S. Novoselov, *Nat. Mater.*, 6(2007) 183.
- Neto, A.H.C., F. Guinea, N. Peres, K. Novoselov, and A. Geim, *Rev. Mod. Phys.*, 81(2009) 109.
- Helveg, S., J.V. Lauritsen, E. Lægsgaard, I. Stensgaard, J.K. Nørskov, B. Clausen, H. Topsøe, and F. Besenbacher, *Phys.*

- Rev. Lett., 84(2000) 951.
5. Lebègue, S. and O. Eriksson, Phys. Rev. B, 79(2009) 115409.
 6. Han, W.Q., L. Wu, Y. Zhu, K. Watanabe, and T. Taniguchi, App. Phys. Lett., 93(2008) 223103.
 7. Novoselov, K., D. Jiang, F. Schedin, T. Booth, V. Khotkevich, S. Morozov, and A. Geim, Proc. Natl. Acad. Sci. USA, 102(2005) 10451.
 8. Mak, K.F., C. Lee, J. Hone, J. Shan, and T.F. Heinz, Phys. Rev. Lett., 105(2010) 136805.
 9. Xu, M., T. Liang, M. Shi, and H. Chen, Chem. Rev., (2013).
 10. Ci, L., L. Song, C. Jin, D. Jariwala, D. Wu, Y. Li, A. Srivastava, Z. Wang, K. Storr, and L. Balicas, Nat. Mater., 9(2010) 430.
 11. Shinde, P.P. and V. Kumar, Phys. Rev. B, 84(2011) 125401.
 12. Han, M.Y., B. Özyilmaz, Y. Zhang, and P. Kim, Phys. Rev. Lett., 98(2007) 206805.
 13. Dutta, S. and S.K. Pati, J. Mater. Chem., 20(2010) 8207.
 14. Ritter, K.A. and J.W. Lyding, Nat. Mater., 8(2009) 235.
 15. Manna, A.K. and S.K. Pati, Chem. Asian. J., 4(2009) 855.
 16. Dong, X., D. Fu, W. Fang, Y. Shi, P. Chen, and L.J. Li, Small, 5(2009) 1422.
 17. Sun, J., Y. Lu, W. Chen, Y. Feng, and A. Wee, Phys. Rev. B, 81(2010) 155403.
 18. Das, B., R. Voggu, C.S. Rout, and C. Rao, Chem. Commun., (2008) 5155.
 19. Şahin, H. and S. Ciraci, Phys. Rev. B, 84(2011) 035452.
 20. Banhart, F., J. Kotakoski, and A.V. Krasheninnikov, ACS Nano, 5(2011) 26.
 21. Arkamita Bandyopadhyay, S.S.Yamijala., S. K Pati Phys. Chem. Chem. Phys., In Press(2013).
 22. Sharma SRKC Yamijala, A. Bandyopadhyay and S. K Pati, Unpublished, (2013).
 23. Ramakrishna Matte, H., A. Gomathi, A.K. Manna, D.J. Late, R. Datta, S.K. Pati, and C. Rao, Angewandte Chemie, 122(2010) 4153.
 24. Radisavljevic, B., A. Radenovic, J. Brivio, V. Giacometti, and A. Kis, Nature Nanotech., 6(2011) 147.
 25. Wang, H., L. Yu, Y.H. Lee, Y. Shi, A. Hsu, M.L. Chin, L.J. Li, M. Dubey, J. Kong, and T. Palacios, Nano Lett., (2012).
 26. Chang, K. and W. Chen, ACS Nano, 5(2011) 4720.
 27. Feng, C., J. Ma, H. Li, R. Zeng, Z. Guo, and H. Liu, Materials Research Bulletin, 44(2009) 1811.
 28. Yang, S., D. Li, T. Zhang, Z. Tao, and J. Chen, J. Phys. Chem. C, 116(2011) 1307.
 29. Zhou, K.G., N.N. Mao, H.X. Wang, Y. Peng, and H.L. Zhang, Angew. Chemie. Int. Ed., 50(2011) 10839.
 30. Liu, K.K., W. Zhang, Y.H. Lee, Y.C. Lin, M.T. Chang, C.Y. Su, C.S. Chang, H. Li, Y. Shi, and H. Zhang, Nano Lett., 12(2012) 1538.
 31. Shi, H., A. Barnard, and I.K. Snook, J. Mater. Chem., 22(2012) 13119.
 32. Ataca, C. and S. Ciraci, J. Phys. Chem. C, 115(2011) 13303.
 33. Ma, Y., Y. Dai, M. Guo, C. Niu, J. Lu, and B. Huang, Phys. Chem. Chem. Phys., 13(2011) 15546.
 34. Komsa, H.P., J. Kotakoski, S. Kurasch, O. Lehtinen, U. Kaiser, and A.V. Krasheninnikov, Phys. Rev. Lett., 109(2012) 35503.
 35. Sorescu, D.C., D.S. Sholl, and A.V. Cugini, J. Phys. Chem. B, 108(2004) 239.
 36. Dey, S., H.S.S.R. Matte, S.N. Shirodkar, U.V. Waghmare, and C.N.R. Rao, Chem. Asian. J., DOI: 10.1002/asia.201300174(2013).
 37. Ivanovskaya, V.V., A. Zobelli, A. Gloter, N. Brun, V. Serin, and C. Colliex, Phys. Rev. B, 78(2008) 134104.
 38. Moses, P.G., J.J. Mortensen, B.I. Lundqvist, and J.K. Nørskov, J. Chem. Phys., 130(2009) 104709.
 39. Raybaud, P., J. Hafner, G. Kresse, and H. Toulhoat, Phys. Rev. Lett., 80(1998) 1481.
 40. Soler, J.M., E. Artacho, J.D. Gale, A. García, J. Junquera, P. Ordejón, and D. Sánchez-Portal, J. Phys.: Cond. Mat., 14(2002) 2745.
 41. Burke, K., J.P. Perdew, and M. Ernzerhof, Int. J. Quantum Chem., 61(1997) 287.
 42. Troullier, N. and J.L. Martins, Phys. Rev. B, 43(1991) 1993.
 43. Kleinman, L. and D. Bylander, Phys. Rev. Lett., 48(1982) 1425.



Arkamita Bandyopadhyay completed her Bachelors degree in Chemistry at Visva-Bharati University, Santiniketan and obtained M.S. degree from Jawaharlal Nehru Centre for Advanced Scientific Research (JNCASR), Bangalore in 2013. Currently she is working as a Ph.D student in New Chemistry Unit of JNCASR. Her research interests include understanding electronic, optical and charge transfer properties of graphene, inorganic graphitic materials and organic electron donor acceptor systems.



Prof. Swapan K Pati obtained his PhD from Indian Institute of Science, Bangalore followed by postdoctoral work at University of California, Davis, and Northwestern University, USA. He is currently a professor in Jawaharlal Nehru Centre for Advanced Scientific Research, Bangalore. He has been a visiting faculty member to a number of universities in the United States, Europe and Japan. He has been a young affiliate of TWAS since 2007 and received TWAS Chemistry (shared) prize in 2013. He is a recipient of the Materials Research Society of India bronze medal (2007), He was selected for the Swarnajayanti Fellowship by Department of Science and Technology of India (2006-07). He has received Shanti Swarup Bhatnagar Prize awarded by Govt. of India in Chemical Sciences, 2010. Also, he has been elected as a fellow of the Indian Academy of Sciences and a fellow of Indian National Academy of Sciences. His research interests include quantum many-body theory, molecular electronics, nonlinear optical phenomena, quantum magnetism, generalized charge-transfer mechanisms, and hydrogen storage. He is also actively involved in developing new theoretical tools for a holistic understanding of structure-property correlations in a whole range of systems from molecules to materials, including biological and biomimetic systems (see <http://www.jncasr.ac.in/pati/> for more information).

A Theoretical Account of the Photodetachment Spectroscopy of Anionic Boron Clusters

S. Rajagopala Reddy and S. Mahapatra

School of Chemistry, University of Hyderabad, Hyderabad-500 046

E-mail: susanta.mahapatra@uohyd.ac.in;smc@uohyd.ernet.in

Abstract:

Photodetachment spectroscopy of bare boron cluster anions (B_3^- , B_4^- and B_5^-) is theoretically studied in this account. Electronic structure of the cluster anions and potential energy surfaces of the ground and low-lying excited electronic states of the corresponding neutral clusters are calculated by the state-of-the-art *ab initio* quantum chemistry methods. Employing the calculated electronic structure data, parameterized vibronic Hamiltonian of the neutral cluster is constructed in a diabatic electronic basis. First principles nuclear dynamics study is then carried out by time-independent and time-dependent quantum mechanical methods to calculate and assign the photo-detachment bands. Theoretical results are compared with the available gas phase experimental data and the importance of electronic non-adiabatic effects on the vibronic structure of the photo-detachment bands is established.

1. Introduction:

Boron, due to its deficiency of one valence p-electron than its neighbor Carbon exhibits novel structure and bonding properties in its chemical compounds. The structure of boron compounds defies the conventional chemical bonding theory. The bare boron clusters have been studied both theoretically and experimentally during the past decade [1-9]. Boron clusters have been studied by mass [5-8] and photoelectron spectroscopy [9] experiments to understand the structure and bonding properties. To the surprise of scientific community, the structure of bare boron clusters (B_n where $n=3-20$) shown to be planar or quasi planar [10]. The planar or quasi planar geometries of boron clusters are established by extensive photoelectron spectroscopy measurements by Wang et al aided by *ab initio* electronic structure calculations by Boldyrev *et al* [9]. Their stability is explained based on aromaticity, anti aromaticity and conflict aromaticity.

As bare boron clusters have planar or quasi planar structure and show aromaticity or antiaromaticity like hydrocarbons, these are projected to be potential compounds as ligands for inorganic chemistry or building blocks of new solids [9]. Recent Computational studies upon designing potential sandwich-like complexes based on the bare all-boron units B_3^- [11a], B_6^{2-} [11b-c], B_7^- [11d], B_8^{2-} [11e-f] and the successful synthesis of the triple-decker $(Cp^*ReH_2)B_5Cl_5$ and $(Cp^*)^2B_6H_4Cl_2$ [11g-h] compounds containing B_5Cl_5 and $B_6H_4Cl_2$ structural units provide hope that many more compounds with bare boron building blocks may be synthesized in the future. In this article we present theoretical studies of photodetachment

process of anionic bare boron clusters with the hope that the theoretical understanding of experimental studies may inspire further investigations leading to synthesis of new coordination compounds containing the planar bare boron clusters as ligands or building blocks of new solids.

Wang *et al* have measured photodetachment spectrum of B_3^- [12a], B_4^- [12a] and B_5^- [12b] clusters at three different photon wavelengths of 355, 266, and 193 nm. These studies revealed the vibronic band structures of the energetically low-lying electronic states of the corresponding neutral clusters with varying degree of energy resolution. While the combined experimental and computational efforts (stated above) unraveled rich information on the equilibrium structure and properties of the ionic and neutral boron clusters, detailed topography of their energetically low-lying electronic states and structure of the photodetachment bands studied in our group. In this article we discuss on some important findings on the photodetachment spectroscopy of B_n^- with $n=3, 4$ and 5 [13a-c] studied by us by *ab initio* quantum dynamical methods. It is found that vibronic coupling is an important mechanism in the dynamics of excited electronic states of these clusters. Consequently fingerprints of electronic nonadiabatic effect for example, overlapping and broad band structure, excitation of nontotally symmetric vibrational mode etc are derived.

2. Vibronic Hamiltonian:

Nuclear dynamics study is performed here in the framework of multimode vibronic-coupling theory [14a-c]. In the latter, the vibronic Hamiltonian involving a group

of interacting electronic states of a multimode molecular system is constructed in terms of normal coordinates of the vibrational modes in a diabatic electronic basis. In this electronic basis coupling between the states appears in the electronic Hamiltonian and the elements of the coupling matrix are smooth function of nuclear coordinates. This enables to solve the quantum eigenvalue equation numerically and in addition Condon approximation is well suited in a diabatic electronic basis. The elements of the diabatic electronic matrix are expanded in a Taylor series in the coordinates of the vibrational modes around the equilibrium geometry of the reference state. Symmetry selection rules are used to retain the appropriate terms in the series expansion. In general such a vibronic Hamiltonian can be written as

$$\mathcal{H} = \mathcal{H}_0 + \mathcal{U} \quad (1a)$$

In the above equation \mathcal{H}_0 represents the diagonal Hamiltonian of the reference state. In a harmonic approximation it is given by

$$\mathcal{H}_0 = \mathcal{T}_N + \mathcal{V}_0 \quad (1b)$$

with, $\mathcal{T}_N = \frac{1}{2} \sum_i \omega_i \frac{\partial^2}{\partial Q_i^2}$ and $\mathcal{V}_0 = \frac{1}{2} \sum_i \omega_i Q_i^2$, representing the nuclear kinetic energy and electronic potential energy operators, respectively, written in terms of the dimensionless normal displacement coordinates Q of the vibrational modes. The elements of the non-diagonal diabatic electronic matrix can be given by

$$u_{nn}(Q) = E_n^0 + \sum_i \kappa_i^n Q_i + \frac{1}{2!} \sum_{i,j} \gamma_{ij}^n Q_i Q_j \quad (1c)$$

$$u_{nm}(Q) = \sum_i \lambda_i^{n,m} Q_i + \frac{1}{2!} \sum_{i,j} \eta_{ij}^{n,m} Q_i Q_j \quad (1d)$$

In the above equations a second-order Taylor expansion is used for the diagonal (u_{nn}) and off-diagonal (u_{nm}) elements of the electronic matrix. The quantity of E_n^0 represents the vertical detachment energy (VDE) of the electronic state n . κ_i^n and γ_{ij}^n represent the linear and second-order coupling parameters of the state n along the vibrational mode i and i and j . Likewise $\lambda_i^{(n,m)}$ and $\eta_{ij}^{n,m}$ represent the linear and second-order coupling parameters, respectively, between electronic states n and m .

3. Computational details:

The coupling parameters of the Hamiltonian introduced above are calculated by performing extensive *ab initio* calculations of adiabatic electronic energy. For this purpose the equilibrium geometry of the reference electronic ground state of the anionic cluster is optimized by a suitable electronic structure method and the dimensionless normal displacement coordinates (Q) of the vibrational modes are calculated. In these coordinates $Q=0$ represents the equilibrium geometry of the reference state. The adiabatic

electronic energies of the final electronic states of the neutral cluster are then calculated along these vibrational modes employing a suitable quantum chemistry method. These energies are then fitted to the adiabatic form of the diabatic electronic Hamiltonian discussed in Sec. 2 to estimate the parameters [13a-c].

The constructed parameterized vibronic Hamiltonian is then used to carry out first principles nuclear dynamical simulations to calculate the photodetachment bands. Both time-independent matrix diagonalization and time-dependent wavepacket (WP) propagation approaches are used for this purpose. In the time-independent approach, the spectral intensity distribution for an electronic transition to the vibronically interacting manifold of electronic states, according to Fermi's golden rule can be written as

$$P(E) = \sum_n |\langle \psi_n^f | \hat{J} | \psi_0^i \rangle|^2 \delta(E - E_n^f + E_0^i). \quad (2)$$

In the above equation, the final states $|\Psi_n^f\rangle$ correspond to the eigenstates of the vibronic Hamiltonian described in Eq. 1 with eigenenergies E_n^f . $|\Psi_0^i\rangle$ is the initial vibrational and electronic ground state of the reference anion with energy E_0^i . This reference state is given by, $|\Psi_0\rangle = |\Phi_0\rangle|\mathbf{0}\rangle$, with $|\Phi_0\rangle$ and $|\mathbf{0}\rangle$ representing the electronic and vibrational components, respectively. The vibrational motion in the initial electronic state (reference anion) is assumed to be harmonic and, therefore, the vibrational component of the above wavefunction is given by the eigenfunction of \mathcal{H}_0 . The operator \hat{J} in Eq. 2 is the transition dipole operator, which describes the interaction of the detachable electron of the anion with the external laser field of energy E . The expectation value of this operator is treated as constant in the present application in accordance with the applicability of the Condon approximation in a diabatic electronic basis.

The time-independent Schrodinger equation for the vibronically coupled states is solved by representing the Hamiltonian in the direct product harmonic oscillator basis of the reference state. The vibronic eigenstates $|\Psi_n^f\rangle$ in this basis read as

$$|\Psi_n^f\rangle = \sum_{\{K_i\},m} a_{K_1,K_2,\dots,K_f,m}^n |K_1\rangle \dots |K_f\rangle |\phi_m\rangle \quad (3)$$

In the above equation the k^{th} level of the i^{th} vibrational mode is denoted by $|K_i\rangle$ and $|\phi_m\rangle$ denotes the m^{th} electronic state in the interacting electronic manifold of the final electronic states. For each vibrational mode, the oscillator basis is suitably truncated in the numerical calculations. In practice, the maximum level of excitation for each mode is estimated from the convergence behavior of the spectral envelope. The Hamiltonian matrix expressed in a direct product Harmonic oscillator basis is highly sparse. We tri-diagonalized this sparse Hamiltonian matrix by employing

the Lanczos algorithm [15]. The diagonal elements of the resulting eigenvalue matrix give the position of the vibronic lines and the relative intensities are obtained from the squared first component of the Lanczos eigenvectors.

In a time-dependent picture, the spectral envelope described in Eq. 2 is directly calculated as Fourier transform of the time autocorrelation function of the WP propagating on the final electronic states.

$$P(E) \approx \sum_n 2R_n \int_0^\infty e^{iE_n t/\hbar} \langle 0 | \tau^\dagger e^{-iHt/\hbar} \tau | 0 \rangle dt \quad (4)$$

$$\approx \sum_n 2R_n \int_0^\infty e^{iE_n t/\hbar} C^n(t) dt, \quad (5)$$

where τ contains the elements of the transition dipole matrix, $\langle \phi_n | \hat{J} | \phi_0 \rangle$, in a diabatic electronic basis and, $C^n(t) = \langle \psi(0) | \psi(t) \rangle$ represents the time autocorrelation function of the WP, initially prepared on the electronic states n . The wavefunction, $\Psi(t)$ at time t is calculated from the initial wavefunction $\Psi(0)$ by numerically solving the time-dependent Schrödinger equation. The Heidelberg multi-configuration time-dependent Hartree approach (MCTDH) is used to accomplish this task [16].

4. Results and discussions:

A. Photodetachment spectroscopy of B_3^- :

The photodetachment spectrum of B_3^- recorded by Wang *et al* consists of four bands [12a]. Both B_3^- and B_3 possess D_{3h} symmetry at the equilibrium configuration of their electronic ground state [12a, 13a]. The equilibrium geometry of B_3^- is optimized by the second-order Møller-Plesset perturbation (MP2) method using correlation-consistent polarized Valence Triple- ζ (cc-pVTZ) basis set. The coordinates of the normal vibrational modes a_1' and e' (Q) and their frequency (ω) of B_3^- are calculated at the same level of theory. Detachment of an electron from the valence molecular orbitals of B_3^- forms neutral B_3 in its energetically low-lying electronic states of \tilde{X}^2A_1' , \tilde{A}^2A_2'' , \tilde{B}^2E' and \tilde{C}^2E' symmetry. The vertical detachment energies are calculated by the outer valence Green's function (OVGF) method using cc-pVTZ basis set along each of the normal vibrational modes. These detachment energies are equated to the adiabatic energies of the electronic states of the neutral B_3 . All the electronic structure calculations are performed with G03 suite of *ab initio* programs [17]. While the ground \tilde{X}^2A_1' , and the excited \tilde{A}^2A_2'' , \tilde{C}^2E' electronic states originate from one electron transition, the degenerate electronic state \tilde{B}^2E' appearing in the 4.0 - 5.0 eV electron binding energy range is assigned to a shakeup state. The static and dynamic aspects of the Jahn-Teller (JT) and pseudo-Jahn-Teller (PJT) interactions in the \tilde{X}^2A_1' - \tilde{C}^2E' electronic states of B_3 have been investigated at length [13a]. Some of the important findings are the following.

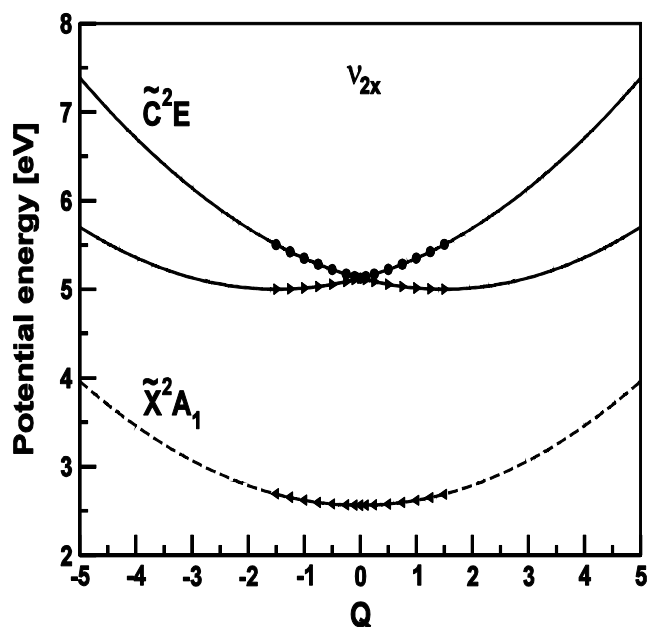


Figure 1: One dimensional cuts of the multidimensional adiabatic potential energy surfaces of the \tilde{X}^2A_1' and \tilde{C}^2E' electronic states of B_3 as a function of the normal displacement coordinate of the x component of the degenerate vibrational mode v_2 . The potential energies obtained from the present vibronic model and computed *ab initio* are shown by the lines and points, respectively.

The adiabatic potential energy surfaces (PESs) of the \tilde{X}^2A_1' - \tilde{C}^2E' electronic states along the normal coordinates of the vibrational modes of reference B_3^- are obtained by diagonalizing the diabatic electronic Hamiltonian of Eq. 1. Apart from the Condon activity, the adiabatic PESs along symmetric vibrational mode v_1 (ring breathing) reveal no significant curve crossings and hence are not shown here for brevity. The symmetric mode cannot lift the degeneracy of \tilde{C}^2E' electronic state but it can shift the potential minimum of this state relative to the equilibrium geometry of the reference anion at $Q=0$. However, symmetry selection rules allow the degenerate vibrational modes (e') to lift the degeneracy of \tilde{C}^2E' electronic state. Therefore, the latter becomes ($E \otimes e$) JT active [18a-c]. Symmetry also allows ($E+A$) $\otimes e$ type of PJT coupling of \tilde{X}^2A_1' - \tilde{C}^2E' electronic states of B_3 along the degenerate vibrational mode. The cuts of the adiabatic PESs of \tilde{X}^2A_1' and \tilde{C}^2E' electronic state along x component of the degenerate vibrational mode v_2 (asymmetric stretching and bending) are shown in Fig. 1. In this figure the points represent the calculated adiabatic energies by the OVGF method employing cc-pVTZ basis set and the solid lines superimposed on them represent energies obtained by fitting these energies to the constructed second-order diabatic electronic Hamiltonian of B_3 . It can be seen that the present vibronic model reproduces the computed electronic energies quite well.

From the above figure, it can be clearly seen that the degeneracy of the electronic state \tilde{C}^2E' is split along degenerate vibrational mode ν_2 . As a result, the two sheets of the JT split potential energy surfaces form conical intersections (CIs) at the D_{3h} configurations. It should be noted here that these intersections are not an isolated point as Fig. 1 reveals. Rather they are a set of points appear along the coordinates of the a_1' vibrational modes at the D_{3h} configurations when the surfaces are viewed along the coordinates of the a_1' and e' vibrational modes simultaneously. These intersections in this particular case are symmetry required. It can be seen from Fig. 1 that upon distortion along Q_{2x} the D_{3h} symmetry of the system breaks and the new energetic minima of lower symmetry appear on the lower adiabatic sheet of the JT split \tilde{C}^2E' electronic state. Within the present second-order vibronic model, energy of these minima is estimated and it amounts to ~ 5.0005 eV. The energetic minimum of the seam of JT CIs is estimated to be ~ 5.125 eV. Therefore, the JT stabilization energy amounts to ~ 0.125 eV.

Theoretically calculated photodetachment bands of the \tilde{X} and \tilde{C} states of B_3^- are plotted in panel b and d along with the corresponding experimental results of Ref. [12a] in panel a and c of Fig. 2, respectively. Theoretical stick spectra are calculated by solving the time-independent quantum eigenvalue equation and are convoluted with a Lorentzian lineshape function of 40 meV full width at the half maximum (FWHM) to generate the spectral envelopes. Both the stick spectra and convoluted envelopes are shown in figs 2(b) and 2(d). It can be seen from Fig. 2 that theoretical results agree very well with the experimental band shape. While the \tilde{X} state of B_3^- could be probed in the experiment at low photon energy (3.496 eV) the vibronic structure of the \tilde{C} state could be probed only by very high energy laser photon of 6.424 eV. As a result, the energy resolution of experimental spectrum of the \tilde{C} state is very poor.

The adiabatic ionization energy of the \tilde{X} state is ~ 2.56 eV. The vertical ionization energy of this state is very close to this value (~ 2.57 eV). This is also obvious from the shape of the \tilde{X} band shown in Fig. 2. The weak progression in this ν_1 band is caused by the symmetric vibrational mode. The lines are ~ 1299 cm^{-1} spaced as compared to the experimental value $\sim 1020 \pm 50$ cm^{-1} [12a]. In contrast to the \tilde{X} band, the theoretical results of Fig. 2(d) exhibit nicely resolved structure of the \tilde{C} band. The adiabatic ionization energy of the \tilde{C} state is ~ 4.96 eV. The resolved vibronic structure of this state contains dominant progression along the degenerate JT active vibrational mode ν_2 . Vibronic lines are ~ 1103 cm^{-1} spaced which is excellent accord with

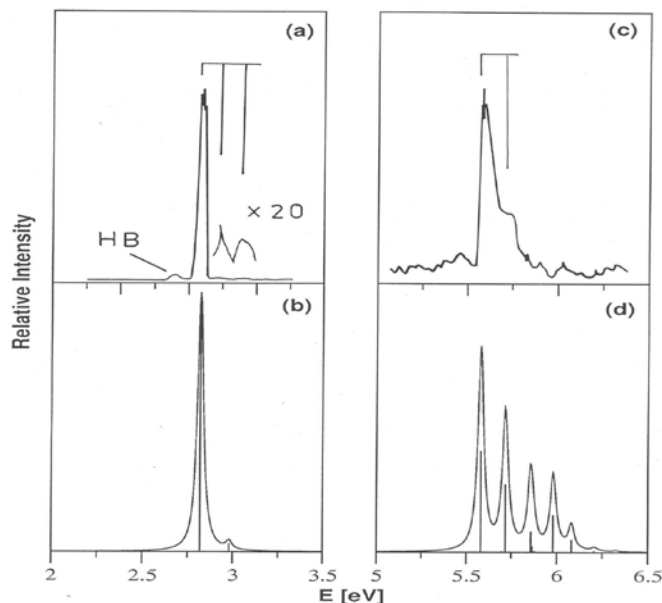


Figure 2: Photodetachment spectrum of B_3^- . Theoretical vibronic level structures of the \tilde{X}^2A_1' and \tilde{C}^2E' states of B_3^- are plotted in panel b and d along with the corresponding experimental results reproduced from Ref. [12a] in panel a and c, respectively. Relative intensity in arbitrary units is plotted as a function of the energy of the final vibronic states of neutral B_3 .

the experimental estimate of $\sim 1100 \pm 80$ cm^{-1} [12a]. The Condon activity of the symmetric ν_1 vibrational mode is very weak in this state. It is found that the PJT, quadratic and bilinear JT coupling makes insignificant contribution and consideration of the linear JT coupling is good enough to reproduce the observed features of this band in the experimental recording.

B. Photodetachment spectroscopy of B_4^- :

The photodetachment spectrum of B_4^- recorded by Wang *et al* revealed four bands in the 1.0 – 5.0 eV energy range [12a]. These bands are predicted to arise from both the singlet and triplet electronic states of neutral B_4 of \tilde{X}^1A_g , \tilde{a}^3B_{2u} , \tilde{b}^3B_{1u} , \tilde{A}^1B_{2u} , \tilde{c}^3B_{2g} and \tilde{B}^1B_{2g} symmetry of the D_{2h} equilibrium symmetry pointgroup. The detachment spectrum recorded at 266 nm revealed complex overlapping structure of the \tilde{a} and \tilde{b} states of B_4 . While the origin of the \tilde{X} , \tilde{a} and \tilde{b} states is predicted successfully, the \tilde{C} band appeared in 193 nm experiment could not be assigned in the experiment [12a]. In its electronic ground state the equilibrium geometry of B_4^- belongs to D_{2h} symmetry point group and \tilde{X}^2B_{1u} and \tilde{X}^2A_g electronic terms, respectively are obtained with Unrestricted Becke 3-Parameter (exchange), Lee, Yang, and Parr (UB3LYP) density functional method and using the augmented correlation-consistent polarized Valence Triple- ζ (aug-cc-pVTZ) basis set of Dunning

[12a, 13b]. The wavefunction of an open-shell molecule like B_4^- suffers from spin contamination. To avoid this, we carried out restricted open-shell MP2 calculations also. The six vibrational modes of B_4^- belong to the following irreducible representation of the D_{2h} symmetry point group, $\Gamma_{vib} = 2a_g + 1b_{3u} + 1b_{2u} + 1b_{1u} + 1b_{3g}$.

While the vibronic selection rules operate in the electronic states of same spin multiplicity, spin vibronic selection rules are applicable to the electronic states of different spin multiplicity. This subject is discussed at length in our earlier publication [13b]. Employing these symmetry rules it has been found that the \tilde{X}^1A_g - \tilde{A}^1B_{2u} and \tilde{X}^1A_g - \tilde{B}^1B_{2g} states of B_4 are coupled through vibrational modes of b_{2u} and b_{2g} symmetry, respectively. The vibrational mode of a_u symmetry can couple the \tilde{A} - \tilde{B} states. The vibrational modes b_{3g} and a_u are symmetry allowed to cause coupling among \tilde{a}^3B_{2u} - \tilde{b}^3B_{1u} and \tilde{a}^3B_{2u} - \tilde{c}^3B_{2g} electronic states, respectively. Furthermore, the \tilde{b}^3B_{1u} - \tilde{c}^3B_{2g} states are symmetrically allowed to be coupled through the vibrational modes of b_{3u} symmetry. Application of spin vibronic selection rules reveal that inter system crossing is allowed between the \tilde{X}^1A_g - \tilde{c}^3B_{2g} , \tilde{A}^1B_{2u} - \tilde{b}^3B_{1u} and \tilde{B}^1B_{2g} - \tilde{a}^3B_{2u} pair of states. We mention that the static spin-orbit coupling strength between the pair of states mentioned above is extremely small ($< 2 \text{ cm}^{-1}$). Therefore, the vibronic coupling among the states of same spin multiplicity is only considered here.

The adiabatic potential energy surfaces of the singlet and triplet electronic states of B_4 are obtained by diagonalizing the diabatic electronic Hamiltonian as described in Sec. 2. In this case the dimension of the Hamiltonian matrix is 6×6 . In contrast to the singlet states, the triplet states show low-energy crossing of the PESs. In order to illustrate, representative one-dimensional cuts of the adiabatic potential energy surfaces of the triplet states of B_4 along the normal displacement coordinates of the totally symmetric (a_g) vibrational modes ν_1 and ν_2 are shown in Fig. 3. The potential energies obtained from the vibronic model are shown by the lines. The adiabatic energies calculated by the complete active space self consistent field (CASSCF) - multi reference internally contracted configuration interaction (MRCI) method are shown by points. It can be seen from the figure that the constructed second-order vibronic model reproduces the *ab initio* energies very well.

Employing the parameters of the Hamiltonian estimated from a fit to the calculated *ab initio* adiabatic electronic energies to the second-order vibronic Hamiltonian of Sec. 2 energetic minimum of the seam of CIs between various pair of states is determined [13b]. The results are given

in Table 1. In the latter the diagonal entries represent the equilibrium minimum of the given state whereas, the off-diagonal entries refer to the energetic minimum of the seam of intersections between the pair of states represented by the second row and first column of the Table.

Table 1: Equilibrium minimum (diagonal entries) and minimum of the seam of various CIs (off-diagonal entries) of the PESs of electronic states of B_4 estimated from the present second-order coupling model.

Singlet States			Triplet states				
	\tilde{X}^1A_g	\tilde{A}^1B_{2u}	\tilde{B}^1B_{2g}		\tilde{a}^3B_{2u}	\tilde{b}^3B_{1u}	\tilde{c}^3B_{2g}
\tilde{X}^1A_g	-	8.18	-	\tilde{a}^3B_{2u}	-	3.34	6.07
\tilde{A}^1B_{2u}	-	3.80	5.10	\tilde{b}^3B_{1u}	-	3.27	11.32
\tilde{B}^1B_{2g}	-	-	4.29	\tilde{c}^3B_{2g}	-	-	4.09

The curve crossing of the \tilde{a}^3B_{2u} - \tilde{b}^3B_{1u} electronic states seen in Fig. 3 develops into CIs in multidimensions as discussed in Sec. 4. A. In this case the CIs are symmetry allowed rather than required as in case of the JT system B_3 . To illustrate, three dimensional perspective view of these two states is shown in Fig. 4 plotted along ν_2 and ν_6 vibrational modes. It can be seen that the degeneracy of the two states is retained along the symmetric mode ν_2 (a_g), whereas, it is lifted along the coupling vibrational mode ν_6 (b_{3g}) and the lower adiabatic surface develops new energetic minima.

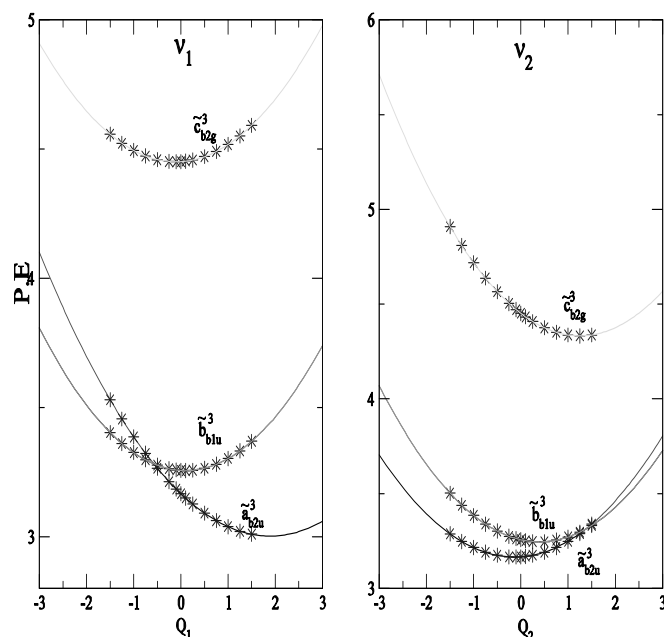


Figure 3: One-dimensional plot of the multidimensional adiabatic potential energy surfaces of the \tilde{a}^3B_{2u} - \tilde{b}^3B_{1u} and \tilde{c}^3B_{2g} electronic states of B_4 as a function of the dimensionless normal displacement coordinates of the totally symmetric vibrational modes.

The broadband vibronic spectrum of the low-lying electronic states of B_4 is shown in Fig. 5 along with the

recorded 193 nm detachment spectrum of Wang et al [12a, 13c]. The theoretical results in Fig. 5 are obtained with 6×6 diabatic Hamiltonian and by propagating wave packets employing the MCTDH method, including all six vibrational degrees of freedom. In order to make sure that the ground state geometry of the reference anion B_4^- does not suffer from spin contaminations, we have optimized the anionic geometry at the UB3LYP, ROMP2 and UCCSD(T) level of theory employing the aug-cc-pVTZ basis set. The adiabatic electronic energies of B_4 are then calculated using the above geometries and Hamiltonian parameters are determined. Theoretical detachment spectra obtained using the set of parameters obtained with UB3LYP and ROMP2 reference geometries are shown in panel a and b of Fig. 5, respectively [13c]. It can be seen that both the results agree extremely well with each other revealing negligible spin contamination in the theoretical results.

The \tilde{X} band (the first band in Fig. 5) revealed a broad structure in all experimental recordings using laser photon of different wavelengths (355, 266, 193 nm) in the experiment [12a]. This broad and diffuse structure arises from a large geometry change of neutral B_4 in the \tilde{X} state relative to the equilibrium geometry of reference B_4^- in its electronic ground state. Our estimate shows that all adjacent B-B bonds are shortened by ~ 0.04 Å and the B-B-B angles are reduced by $\sim 13^\circ$ in the neutral \tilde{X} state. In addition, the bond between the diagonally opposite B

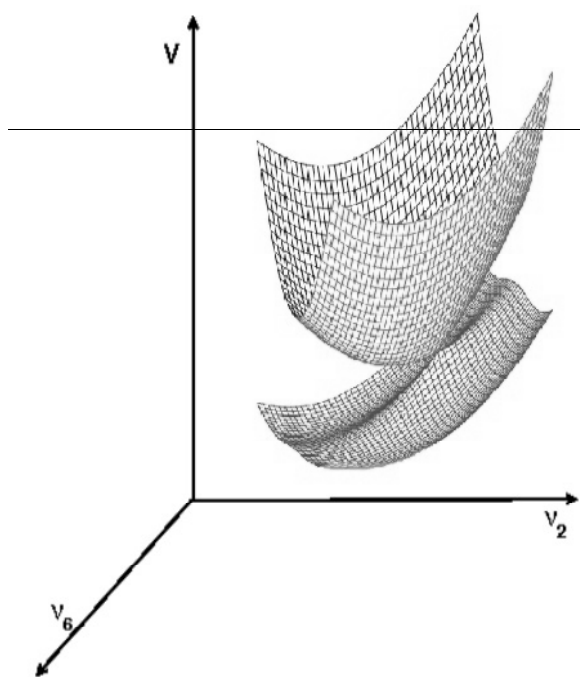


Figure 4: Three-dimensional perspective view of the \tilde{a}^3B_{2u} - \tilde{b}^3B_{1u} conical intersections of B_4 .

atoms elongates by ~ 0.25 Å in the neutral \tilde{X} state. In order to estimate the excitation of the vibrational modes we also performed the calculation of stick vibronic spectrum of this state by a matrix diagonalization approach. Our findings revealed that the symmetric mode ν_2 form the dominant progression in this band [13c]. Peak spacing of ~ 423 cm^{-1} corresponding to this mode was found from the stick spectrum [13c]. In addition the combination $(\nu_1 + \nu_2)$ mode also forms the ~ 1590 cm^{-1} progression in this band. The \tilde{X} state is not linearly coupled with the \tilde{A} and \tilde{C} states. The combination mode $\nu_3\nu_6$ couples this state with the \tilde{A} state. However, no noticeable effect of this coupling on the vibronic structure of this band is observed [13c].

The second band in Fig. 5 is equally broad and diffuse and can be assigned to the vibronic structure of the coupled \tilde{a}^3B_{2u} - \tilde{b}^3B_{1u} electronic states based on the estimate of their vertical detachment energies. These states are coupled through the ν_6 (b_{3g}) vibrational mode and also the interstate bilinear coupling through the $\nu_3\nu_4$ combination mode. It can be seen from Table I that the energetic minimum of the seam of \tilde{a} - \tilde{b} CIs (cf. Fig. 4) is quasi-degenerate with

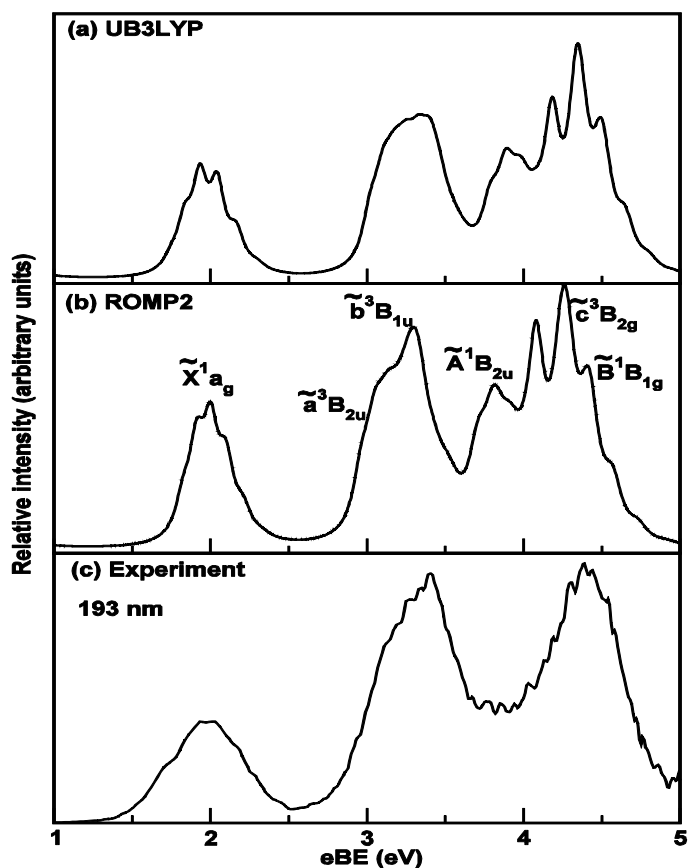


Figure 5: The photo detachment bands of B_4 obtained by the time-dependent WP propagation approach (see, text for details) and employing a 6×6 vibronic Hamiltonian.

the equilibrium minimum of the \tilde{b} state. The latter causes the strong nonadiabatic mixing of the vibrational levels of the \tilde{a} and \tilde{b} states and contributes to the composite broad and diffused vibronic band of these two electronic states. Detailed analysis revealed that the vibrational mode ν_2 forms the major progression ($\sim 741 \text{ cm}^{-1}$) in the \tilde{a} state and very weak excitation of ν_1 vibrational mode ($\sim 1150 \text{ cm}^{-1}$) in the \tilde{b} state is found [13c].

The third detachment band in Fig. 5 is due to the overlapping \tilde{A} , \tilde{c} and \tilde{B} electronic states of B_4 . These states are vertically located within $\sim 1.0 \text{ eV}$. The coupling of \tilde{A} and \tilde{B} electronic states is not revealed by the electronic structure data. The \tilde{c} state is strongly coupled to the \tilde{b} state through ν_5 vibrational mode of b_{3u} symmetry. Despite this, as can be seen from Table I that the minimum of the \tilde{b} - \tilde{c} intersection occurs $\sim 7.24 \text{ eV}$ above the minimum of the \tilde{c} state. Therefore, nonadiabatic coupling has essentially no impact on the overlapping structure of the third band. Although the overall structure of this band is in good accord with the experiment, the structure in the theoretical result found between $3.7 - 4.25 \text{ eV}$ is missing in the experimental results. Vibrational mode ν_2 in the \tilde{A} and ν_1 in \tilde{B} and \tilde{c} electronic states form the major progression. Peak spacings of ~ 767 , ~ 1234 and $\sim 1237 \text{ cm}^{-1}$ respectively, are extracted from the stick vibronic structure of the third band.

C. Photodetachment spectroscopy of B_5^- :

The cluster anion B_5^- belongs to the C_{2v} symmetry point group at the equilibrium minimum of its electronic ground state. Ionization of electron from its valence molecular orbitals produces the neutral B_5 cluster in its ground \tilde{X}^2B_2 and low-lying excited \tilde{A}^2A_1 , \tilde{B}^2B_2 , \tilde{C}^2A_1 , \tilde{D}^2B_1 and \tilde{E}^2A_1 electronic states. The electronic structure of reference B_5^- is optimized at the MP2/aug-cc-pVTZ level of theory to calculate the equilibrium geometry and normal vibrational modes of its electronic ground state. The nine vibrational modes of B_5 transforms to, $\Gamma_{vib} = 4a_1 + 1a_2 + 1b_1 + 3b_2$ irreducible representations of the C_{2v} symmetry point group.

The adiabatic energies of the mentioned six electronic states of B_5 are calculated along the normal coordinates of each of these vibrational modes. The calculations are performed by the CASSCF(11,10)-MRCI method by using *ab initio* software MOLPRO [19]. These electronic energies are employed to construct a second-order diabatic vibronic Hamiltonian of the six electronic states of B_5 using the symmetry selection rules. According to the latter coupling of the \tilde{X} state with the \tilde{A} , \tilde{C} and \tilde{E} states is allowed by the vibrational modes of b_2 symmetry. Likewise \tilde{X} - \tilde{D} coupling is caused by the a_2 vibrational modes. The b_2 vibrational

modes also couple \tilde{A} - \tilde{B} , \tilde{B} - \tilde{C} and \tilde{B} - \tilde{E} electronic states. The \tilde{A} - \tilde{D} , \tilde{C} - \tilde{D} and \tilde{D} - \tilde{E} electronic states are coupled by the b_1 vibrational modes. The topography of these coupled electronic states is examined in detail and various stationary points on them are determined [13b]. Analogous to the data given in Table I for B_4 , the energetic minimum of various intersection seams and equilibrium minimum of the states estimated from the vibronic Hamiltonian of B_5 are collected in Table II. To illustrate, the adiabatic potential energy functions of the six electronic states of B_5 are plotted in Fig. 6, along the symmetric vibrational modes (a_1). Crossing of various electronic states can be readily seen from figure.

Table 2. Equilibrium minimum (diagonal entries) and minimum of the seam of various CIs (off-diagonal entries) of the PESs of the six energetically low-lying electronic states of B_5 extracted from the constructed second-order vibronic model.

	\tilde{X}^2B_2	\tilde{A}^2A_1	\tilde{B}^2B_2	\tilde{C}^2A_1	\tilde{D}^2B_1	\tilde{E}^2A_1
\tilde{X}^2B_2	-	4.10	-	7.10	16.67	7.45
\tilde{A}^2A_1	-	3.50	4.21	-	14.75	-
\tilde{B}^2B_2	-	-	4.15	5.73	5.26	9.05
\tilde{C}^2A_1	-	-	-	4.83	5.52	-
\tilde{D}^2B_1	-	-	-	-	5.09	5.44
\tilde{E}^2A_1	-	-	-	-	-	5.44

The broadband spectral envelope of B_5 obtained by propagating wavepackets using the MCTDH method [17] is shown in the panel (a) of Fig. 7. The 193 nm experimental recording of Ref. 12(b) is shown in the panel (b) of Fig. 7. It can be seen from this figure that the broadband theoretical spectrum agrees fairly well with the experimental band structures. The vibrational structure and nuclear dynamics of \tilde{X} state are studied by us at length using a matrix diagonalization method in coupled and uncoupled state situations [13c]. Line spacings of ~ 724 and $\sim 658 \text{ cm}^{-1}$ corresponding to progression of ν_3 and ν_4 vibrational modes, respectively, are observed in the uncoupled spectrum. The \tilde{X} state is coupled to \tilde{A} , \tilde{C} and \tilde{E} states by the vibrational modes of b_2 (ν_7 , ν_8 and ν_9) symmetry. From Table 2 it can be seen that the intersections of \tilde{X} state with the \tilde{C} and \tilde{E} states occur at higher energies except the \tilde{A} state. Some increase in the stick line density is observed in the \tilde{X} - \tilde{A} coupled states stick spectrum arising from electronic nonadiabatic effects. Weak excitations of nontotally symmetric modes ν_7 , ν_8 and ν_9 of b_2 symmetry, respectively are extracted from the stick spectrum of the \tilde{X} - \tilde{A} coupled electronic states.

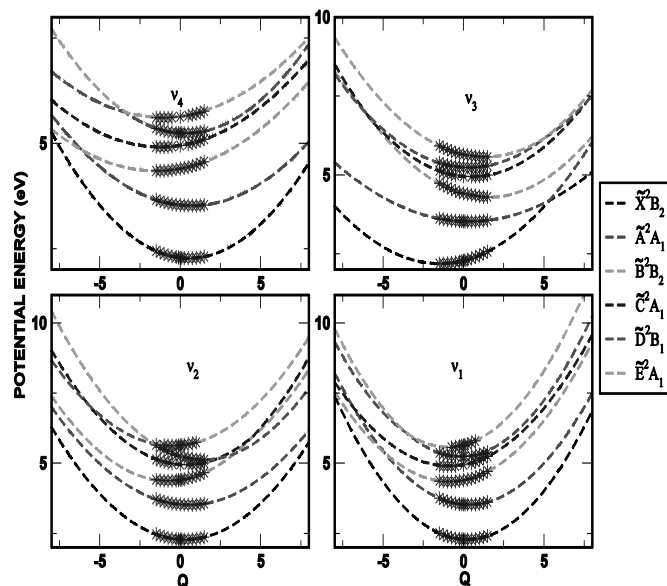


Figure 6: Same as in Fig. 3 for the \tilde{X}^2B_2 , \tilde{A}^2A_1 , \tilde{B}^2B_2 , \tilde{C}^2A_1 , \tilde{D}^2B_1 and \tilde{E}^2A_1 electronic states of B_5 along the totally symmetric vibrational modes.

The vibrational mode ν_4 (a_1 symmetry) forms the dominant progression with $\sim 530 \text{ cm}^{-1}$ spacing in uncoupled \tilde{A} state. This is in very good accord with the experimental value of this spacing of $\sim 530 \text{ cm}^{-1}$. In addition to the significant interstate $\tilde{X}-\tilde{A}$ coupling by ν_7 and ν_3 modes, the $\tilde{A}\tilde{A}$ state is also coupled to the \tilde{B} state by ν_7 vibrational mode. The equilibrium minimum of \tilde{A} state occurs ~ 0.6 and ~ 0.7 eV below the minimum of $\tilde{X}-\tilde{A}$ and $\tilde{A}-\tilde{B}$ CIs, respectively. As a consequence, strong nonadiabatic effects cause a huge increase of line density in the coupled state spectrum of the $\tilde{A}\tilde{A}$ state and as a result the spectral envelope becomes broad and diffuse. Weak excitation of ν_3 mode is also observed in the coupled states stick spectrum of $\tilde{A}\tilde{A}$ state.

The \tilde{B} band is found to be very broad and diffuse in the 193 nm recording of Wang et al [12b]. No vibrational progressions could be resolved from the experimental band structure of this state. In the uncoupled state theoretical spectrum of \tilde{B} state vibrational modes ν_1 , ν_2 , ν_3 and ν_4 are found to form dominant progressions with energy spacings of ~ 1242 , ~ 901 , ~ 723 and $\sim 337 \text{ cm}^{-1}$ respectively. The \tilde{B} state is coupled to \tilde{A} , \tilde{C} and \tilde{E} states through the vibrational modes of b_2 symmetry. From Table 2 it can be seen that equilibrium minimum of \tilde{B} state occurs ~ 0.06 , ~ 1.58 and ~ 4.90 eV below the minimum of the $\tilde{A}-\tilde{B}$, $\tilde{B}-\tilde{C}$ and $\tilde{B}-\tilde{E}$ CIs, respectively. The effect of $\tilde{A}-\tilde{B}$ coupling on the vibronic structure of the \tilde{B} band is found to be very strong. This mainly contributes to the observed broad and diffuse structure of the \tilde{B} band.

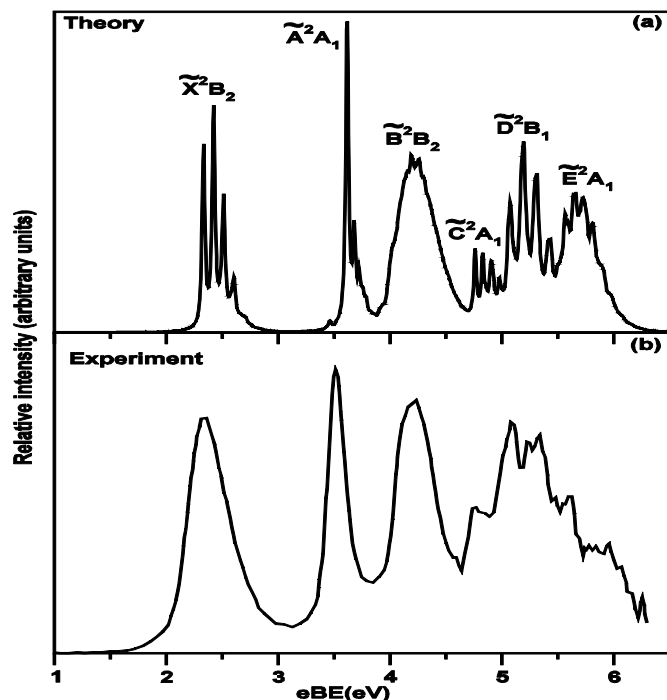


Figure 7: Broadband spectral envelope (panel (a)) of the low-lying six electronic states of B_5 cluster obtained by the WP propagations employing a second-order vibronic model. The 193 nm experimental recording of Ref. 12(b) is shown in panel (b).

Both one electron detachment channels as well as multi-electron transitions are found by us in the third band marked C in the energy range between 4.7 and 6.2 eV [13b]. No assignment of these features is available from an analysis of the experimental spectrum. We have found two one-electron detachment channels leading to \tilde{C}^2A_1 and \tilde{D}^2B_1 electronic states of B_5 and several shake-up states exist in this energy range. We, however, mention that along with one electron detachment states \tilde{C} and \tilde{D} , we considered the shake-up state \tilde{E} in the theoretical calculations of the C band. The latter state is found to have some contribution in the observed structure of the C band between 5.4 and 6.0 eV. The structures between 4.7 and 5.4 eV are found to be formed by the \tilde{C} and \tilde{D} electronic states of B_5 .

The existence of the \tilde{C}^2A_1 state does not have any clear evidence in the literature [12b]. In our CASSCF (11,10)-MRCI calculations, we found this state at ~ 4.96 eV of VDE. Now, the hump in the experimental results, between ~ 4.5 and 5.0 eV can only be obtained with the CASSCF(11,10)-MRCI electronic structure data, as shown in Fig. 7. We, therefore, conclude (as confirmed by more test calculations) the existence of the \tilde{C}^2A_1 state in this energy region. The vibrational modes ν_1 and ν_4 form detectable progression in the state. Line spacings of ~ 1191 and ~ 474

cm^{-1} , respectively, are extracted from the spectrum of the \tilde{C} state. The vibrational mode ν_2 form extended progression in the \tilde{D} state. Line spacing of $\sim 964 \text{ cm}^{-1}$ has been found from its spectrum. Progression of vibrational modes ν_1, ν_3 , and ν_4 is extracted from the spectrum of the \tilde{E} state. Peak spacings of $\sim 1239, \sim 723$, and $\sim 471 \text{ cm}^{-1}$ corresponding to the excitation of these modes, respectively, are found from this spectrum

Conclusions:

We have presented a brief theoretical account of the photodetachment spectroscopy of anionic boron clusters (B_n^- , $n=3, 4$ and 5). The theoretical study involves construction of vibronic Hamiltonians of the electronic ground and excited states of the corresponding neutral clusters through state-of-art *ab initio* quantum chemistry calculations. Employing these Hamiltonians the nuclear dynamics is studied subsequently from first principles by solving quantum eigenvalue equation. Theoretically calculated vibronic structures of the photodetachment bands are reported and compared with the available experimental recordings. The theoretical results are generally found to be in good accord with the experiment. Some of our findings are the following.

Contribution of nonadiabatic effects due to coupling among electronic states is found to be substantial in the detailed structure of the photodetachment bands, in particular, of excited electronic states.

Vibrational progression of $\sim 1229 \text{ cm}^{-1}$ along the symmetric vibrational mode ν_1 is observed in the detachment spectrum of the \tilde{X}^2A_1' state of B_3 as compared to its experimental value of $\sim 1020 \pm 50 \text{ cm}^{-1}$. Vibrational progression of $\sim 1103 \text{ cm}^{-1}$ due to the degenerate vibrational mode ν_2 is found in the JT split \tilde{C}^2E' electronic manifold of B_3 . This compares very well with its experimental value of $\sim 1100 \pm 80 \text{ cm}^{-1}$. The JT stabilization energy $\sim 0.125 \text{ eV}$ of the \tilde{C}^2E' state is estimated from constructed second-order vibronic model.

The nonadiabatic coupling effects are small in the electronic states of B_4 . Some significant effect of this coupling is found in the a^3B_{2u} and b^3B_{1u} states of B_4 only. The symmetric vibrational mode ν_1 and ν_2 forms progression in all the six low-lying electronic states of B_4 considered here. The photodetachment spectra calculated by employing reference equilibrium geometries calculated by the UB3LYP and ROMP2 methods are in excellent agreement with experiment indicating negligible effect of spin-contamination in theoretical results.

In contrast to B_4 , the nonadiabatic coupling effects are far more significant in the photodetachment bands of

B_5 . In addition to the totally symmetric modes, coupling vibrational modes are also excited in the vibronic bands of B_5 . Nontotally symmetric vibrational modes ν_7, ν_8 and ν_9 are weakly excited in the \tilde{X} band. The symmetric vibrational modes are weakly excited in \tilde{A} band. Energy spacings of $\sim 530 \text{ cm}^{-1}$ due to ν_4 vibrational mode, in agreement with the experimental estimate of $\sim 530 \text{ cm}^{-1}$ have been extracted from the \tilde{A} band. While the dominant vibrational progression is caused by the vibrational mode ν_3 in the \tilde{X} band, the same is caused by the vibrational mode ν_4 in the \tilde{A} band. Vibrational mode ν_3 forms strongest progression in the \tilde{B} band. The complex C band is formed by the overlapping \tilde{C}, \tilde{D} and \tilde{E} electronic states of B_5 . Vibrational modes $\nu_1, \nu_4; \nu_2; \nu_1, \nu_3$ and ν_4 form progression in the \tilde{C}, \tilde{D} and \tilde{E} states, respectively.

Acknowledgment:

This study is in part supported by a research grant from the Department of Science and Technology, New Delhi (Grant No. DST/SF-04/2006). SM acknowledges T. S. Venkatesan and K. Deepika for their association with the work on B_3^- . The computational facilities provided under the UPE and HPCF programs of the University Grant Commission and the Department of Science and Technology, New Delhi, respectively, in CMSD of the University of Hyderabad are gratefully acknowledged. S.R.R. also thanks the Council of Scientific and Industrial Research for a senior research fellowship.

References:

1. H. Kato and K. Yamashita, Chem. Phys. Lett. 190, 361 (1992).
2. I. Boustani, Int. J. Quantum Chem. 52, 1081 (1994).
3. A. Ricca and C. W. Bauschlicher, Jr., Chem. Phys. 208, 233 (1996).
4. I. Boustani, Phys. Rev. B 55, 16426 (1997).
5. L. Hanley, J. L. Whitten, and S. L. Anderson, J. Phys. Chem. 92, 5803 (1988).
6. L. Hanley and S. L. Anderson, J. Phys. Chem. 91, 5161 (1987).
7. S. A. Ruatta, P. A. Hintz, and S. L. Anderson, J. Chem. Phys. 94, 2833 (1991).
8. P. A. Hintz, S. A. Ruatta, and S. L. Anderson, J. Chem. Phys. 92, 292 (1992).
9. A. N. Alexandrova, A. I. Boldyrev, H. J. Zhai, and L. S. Wang, Coord. Chem. Rev. 250, 2811 (2006).
10. B. Kiran, S. Bulusu, H. J. Zhai, S. Yoo, X. C. Zeng, and L. S. Wang, Proc. Natl. Acad. Sci. U.S.A. 102, 961 (2005).
11. (a) Li-Ming Yang, Jian Wang, Yi-bong Ding and Chinchung Sun, J. Phys. Chem. A 111, 9122 (2007); (b) A. N. Alexandrova, A. I. Boldyrev, H-J Zhai, L-S. Wang, J. Chem. Phys. 122, 054313, (2005); (c) Q. S. Li, Q. Jin, J. Phys. Chem. A 107, 7869, (2003); (d) Q. S. Li, L. F. Gong, J. Phys. Chem. A

- 108, 4322, (2004); (e) A. N. Alexandrova, H-J Zhai, L-S Wang, A. I. Boldyrev, *Inorg. Chem.* **43**, 3552, (2004); (f) S. D. Li, J. C. Guo, C. Q. Miao, G. M. Ren, *Angew. Chem., Int. Ed.* **44**, 2158, (2005); (g) Le Guennic, B.; Jiao, H.; Kahlal, S.; Saillard, J.-Y.; Halet, J.-F.; Ghosh, S.; Shang, M.; Beatty, A. M.; Rheingold, A. L.; Fehlnert, T. P. *J. Am. Chem.Soc.* **126**, 3203, (2004); (h) Ghosh, S.; Beatty, A. M.; Fehlnert, T. P. *J. Am. Chem. Soc.* **123**, 9188, (2001);
12. (a) H. J. Zhai, L. S. Wang, A. N. Alexandrova, A. I. Boldyrev, and V. G. Zakrzewski, *J. Phys. Chem. A* **107**, 9319 (2003).; (b) H. J. Zhai, L. S. Wang, A. N. Alexandrova, and A. I. Boldyrev, *J. Chem.Phys.* **117**, 7917 (2002);
13. (a) T. S. Venkatesan, K. Deepika and S. Mahapatra, *J. Comput. Chem.* **27**, 1093 (2006); (b) S. Rajagopala Reddy and S. Mahapatra, *J. Chem. Phys.* **136**, 024322, (2012); (c) S. Rajagopala Reddy and S. Mahapatra, *J. Chem. Phys.* **136**, 024323, (2012);
14. (a) H. Köppel, W. Domcke and L. S. Cederbaum, *Adv. Chem. Phys.* **57**, 59 (1984); (b) S. Mahapatra, *Acc. Chem. Res.* **42**, 1004 (2009); (c) S. Mahapatra, *Int. Rev. Phys. Chem.* **23**, 483 (2004).
15. J. Cullam and R. Willoughby, Lanczos algorithm for large symmetric eigenvalue problems (Birkhauser, boston, 1985) Vol I and II.
16. (a) G. A. Worth, M. H. Beck, A. Jackle, and H. -D. Meyer, The MCTDH Package, Version 8.2, (2000), University of Heidelberg, Heidelberg, Germany. H. -D. Meyer, Version 8.3 (2002), Version 8.4 (2007). See <http://mctdh.uni-hd.de>. (b) H. -D. Meyer, U. Manthe, and L. S. Cederbaum, *Chem. Phys. Lett.* **165**, 73 (1990). (c) U. Manthe, H. -D. Meyer, and L. S. Cederbaum, *J. Chem. Phys.* **97**, 3199 (1992). (d) M. H. Beck, A. Jackle, G. A. Worth, and H. -D. Meyer, *Phys. Rep.* **324**, 1 (2000).
17. M. J. Frisch, G. W. Trucks, H. B. Schlegel et al., GAUSSIAN 03, Revision B. 05, Gaussian, Inc., Pittsburgh, PA, 2003.
18. (a) H. A. Jahn, E. Teller, *Proc. R Soc. Lond. Ser. A* **161**, 220, (1937); (b) I. B. Bersuker, *The Jahn-Teller Effect*, (Cambridge University Press, Cambridge, UK, 2006); I. B. Bersuker, *Chem. Rev.* **101**, 1067 (2001). (c) H. Köppel, L.S. Cederbaum, and S. Mahapatra, *Theory of the Jahn-Teller Effect: Handbook of High-Resolution Spectroscopy*, John Wiley & Sons, (2011);
19. H.-J. Werner, P. J. Knowles, R. D. Amos, A. Bernhardsson et al., MOLPRO version 2002.1, a package of *ab initio* programs, 2002, see <http://www.molpro.net>.



Rajagopala Reddy Seelam received his M.Sc (2008) in chemistry from the School of Chemistry of the University of Hyderabad. Afterwards he joined in the Ph. D program of the School and working in the group of Prof. Susanta Mahapatra. He works in the broad area of nonadiabatic chemistry and his main research interests are electronic structure calculations, gas phase spectroscopy, and vibronic interactions in polyatomic molecules.



Susanta Mahapatra received his M.Sc. (1991) in chemistry from the Banaras Hindu University and a Ph.D. (1996) in theoretical chemistry from I. I. T. Kanpur with N. Sathyamurty. He did postdoctoral work with L. Z icked at the University of Potsdam (1996-1997) and with H. Köppel and L. S. Cederbaum at the University of Heidelberg (1997-2000) and joined the faculty of the School of Chemistry, University of Hyderabad, in October 2000 where he is currently a professor. His research mainly focuses on the quantum mechanical studies of nonadiabatic chemical dynamics.

Methanol in its normal liquid and supercritical states: Changes of polarity and hydrogen bonding from first principles simulations

Vivek Kumar Yadav and Amalendu Chandra

Department of Chemistry, Indian Institute of Technology, Kanpur, India 208016.

Abstract

Supercritical methanol behaves very differently from normal liquid methanol. For example, supercritical methanol dissolves ionic solutes less effectively and nonpolar solutes more effectively than liquid methanol. Here we discuss our recent results of first principles theoretical studies on the changes of hydrogen bonding properties and polarity in methanol as one moves from normal liquid to its supercritical states.

1 Introduction

Methanol is the simplest organic liquid having a hydrogen bonded network structure [1,2]. However, above its critical temperature (513 K) and pressure (78.5 bar), commonly known as supercritical methanol, the solvent has very different structural, solvation and dynamical properties [1-10]. For example, supercritical methanol dissolves ionic solutes less effectively and nonpolar solutes more effectively than normal liquid methanol. Additionally, the density of supercritical methanol can be changed from liquid-like to gas-like densities to tune its solvent properties without any liquid- gas phase transition. Due to this large variation in solvation properties, supercritical methanol has found applications in many chemical processes of technological and industrial importance [11, 12]. Here we briefly review our recent results of *ab initio* simulations of methanol in its liquid and supercritical states [13-15]. In particular, we look at the changes of its solvent properties with respect to hydrogen bonding and polarity of methanol molecules as one moves from normal liquid to supercritical states. Our study is based on the method of *ab initio* molecular dynamics [16, 17]. For the supercritical methanol, We have considered three different densities ranging from 0.768 to 0.348 g cm⁻³ at a supercritical temperature of 523 K [15]. We note that the use of *ab initio* many-body potentials in molecular simulations is especially important for supercritical fluids since the commonly used empirical potential models are usually parameterized for normal liquid state and use of such empirical potentials may not be adequate for supercritical states. In the next section, we have presented more details of the *ab initio* simulations of supercritical methanol. The results of our study are discussed in the two subsequent sections for hydrogen bonded structures and their relations to spectral observables like vibrational stretch frequencies and also for polarity of methanol molecules. Finally, our conclusions are briefly summarized in the last section.

2 Details of *ab initio* molecular dynamics simulations and time series analysis

In *ab initio* molecular dynamics simulations, the forces on the nuclei are obtained directly from an electronic structure calculation performed 'on the fly' via adiabatic dynamics principle [16, 17]. In this method, the force (F_i) on particle i at time t is given by

$$F_i(t) = -\nabla \langle \Psi_e(t) | H_e | \Psi_e(t) \rangle \quad (1)$$

where Ψ_e and H_e are the electronic wave function and the electronic Hamiltonian operator, including the nuclear repulsion terms, of the system under investigation. In the present study, the *ab initio* molecular dynamics simulations are performed by using the Car-Parrinello molecular dynamics (CPMD) method [16]. This method combines a quantum mechanical treatment of the electrons within the framework of density functional theory and a classical treatment of the nuclei. The forces on the nuclei are calculated on the fly as the simulation progresses without depending on any predefined interaction potentials. We have used the CPMD code [18] in the present study to carry out the *ab initio* simulations of supercritical methanol at varying density. The equations of motion of Car-Parrinello molecular dynamics were numerically integrated by using a time step of 5 a.u. for liquid methanol at 300 K and 3 a.u. for supercritical methanol at 523 K. For the supercritical methanol, simulations are performed for three different densities of 0.768, 0.563 and 0.348 g cm⁻³. All hydrogen atoms were assigned the mass of deuterium to reduce the influence of quantum effects on the calculated properties. Also, use of deuterium mass ensured that electronic adiabaticity and energy conservation were maintained throughout the simulations. The quantum electronic structure calculations have been carried out using two different density functionals: The well-known BLYP [19] functional and its dispersion corrected version BLYP-D [20, 21]. Further details of the simulations are available in

We dedicate this work to Dr. Swapan K. Ghosh on his 64th Birthday.

Refs. [13-15]. Our primary goals are to study the polarity and hydrogen bonding aspects of supercritical methanol and how these properties compare with those of normal liquid methanol. For polarity, we have calculated the dipole moments by using the Wannier Function Centre (WFC) method details of which are available in Refs. (xx). Regarding the hydrogen bonding properties, we are particularly interested in finding the correlations of hydrogen bonds and spectral observables like vibrational stretch frequencies. For this purpose, we have employed the wavelet analysis method [22, 23]. The details of this method for calculations of hydroxyl frequencies can be found Refs. [13-15, 24, 25].

3. Hydrogen bonds and hydroxyl stretch frequencies of supercritical methanol

It is known that the hydrogen bonds in liquid methanol causes a red shift to its hydroxyl stretch frequency compared to that in an isolated methanol molecule. The stretch frequency increases as the associated hydrogen bond becomes longer or weaker. Hence, studies of such correlations between the length of hydrogen bonds and stretch frequencies of the hydroxyl group of methanol and how such correlations change as one moves to supercritical states from the normal liquid state would reveal important information about the changes of hydrogen bonded structures and their implications on experimental observables such as vibrational spectroscopy for supercritical methanol. In Figs. 1 and 2, we have shown the results of such frequency-structure correlations through the contour plots of the conditional probability of observing a particular OD covalent stretch frequency for a given D..O distance (figures taken from Refs.[13, 15]). It may be noted that we are dealing with CD_3OD in place of CH_3OH , hence we are talking about OD frequency rather than OH frequency. Here the oxygen of D..O is the nearest to the D atom, i.e. it is the hydrogen bond distance in the event of the chosen OD mode being hydrogen bonded. Fig.1 shows the results for density 0.768 g cm^{-3} and Fig.2 shows the results for the two lower densities. The frequency, on average, is seen to increase with the D..O distance, particularly on the lower D..O distance side. However, the rate of increase gradually decreases as the density is lowered or as the D..O distance is increased. Also, with decreasing density, the maximum probability moves to a larger distance-higher frequency value. The distributions for ambient and supercritical water at the same density (Fig.1) also reveal a clear change in the shape with increase of temperature. In the supercritical state, the distribution is extended to larger D..O distance which can be attributed to weaker and less number of hydrogen bonds at the supercritical temperature. The vertical dashed line in these

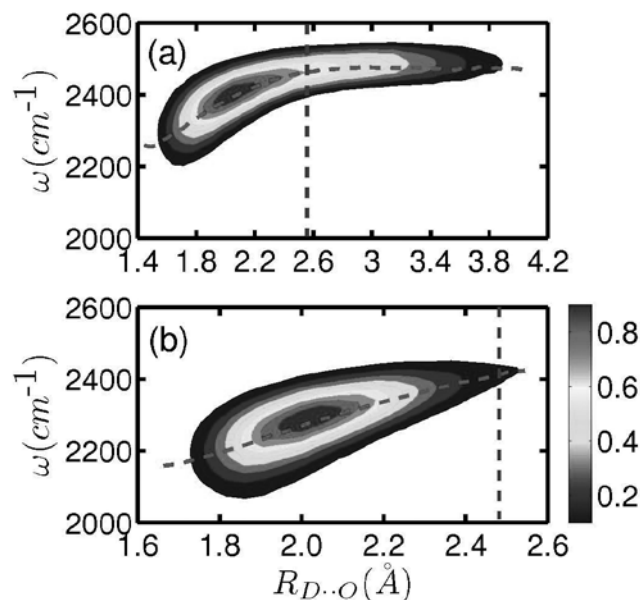


Fig.1. The joint probability distributions of hydroxyl OD frequency and D..O distance in supercritical and liquid deuterated methanol at density 0.768 g cm^{-3} . The results of (a) and (b) are for $T = 523\text{K}$ and 300 K . The results are for the BLYP functional. (Reproduced from Refs. [13, 15]).

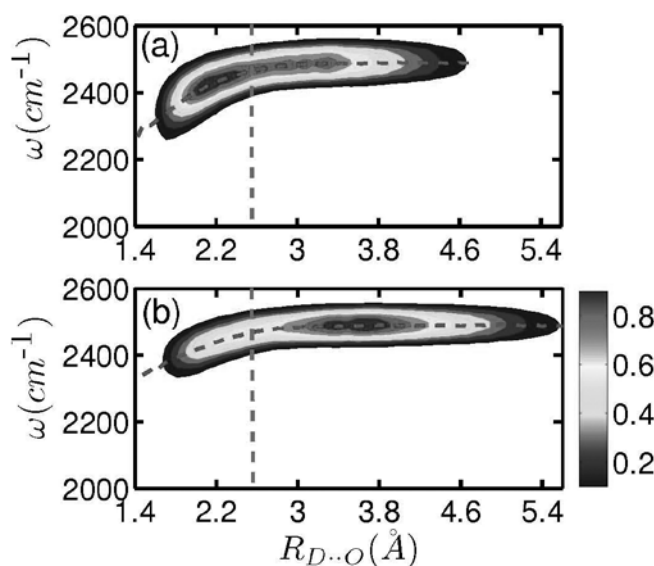


Fig. 2. The joint probability distributions of hydroxyl OD frequency and D..O distance in supercritical deuterated methanol at 523K for methanol densities of (a) 0.532 and (b) 0.348 g cm^{-3} , respectively. The results are for the BLYP functional. (Reproduced from Ref. [15])

figures divides the hydrogen-bonded and non-hydrogen-bonded states as given by the geometric criterion used to define the hydrogen bonds in methanol systems [13-15]. It can be seen that while the major part of the probability distribution falls on the left side of the dividing line for the normal liquid methanol, an opposite behaviour is observed

for the supercritical methanol at lower densities. For the low density systems, major part of the frequency-distance probability distribution falls in the non-hydrogenbonded region. The number of hydrogen bonds per water is found to be 1.25 (1.42), 1.02 (1.25) and 0.55 (0.95) for the densities 0.768, 0.563 and 0.348 g cm⁻³, respectively, at 523 K for the BLYP (BLYP-D) functional [15] and it is around 2.0 for normal liquid methanol [13, 14]. Thus, it is clear that the hydrogen bonds play less significant roles in determining the vibrational spectral properties in the hydroxyl stretch region for supercritical methanol at low densities.

4 Molecular dipole moments of supercritical methanol

Calculation of molecular dipole moments is an important aspect of the studies of methanol since it is known that the solvation properties of methanol changes as we move from normal liquid to supercritical conditions. We calculated the changes of dipole moments of methanol molecules on increase of temperature at the same density and also on decrease of density at the same supercritical temperature. We have calculated the dipole moments of individual molecules by using the so-called maximally localized Wannier functions and Wannier Function Centers method as mentioned earlier. In Fig.3, we have shown the dipole distributions of supercritical methanol for varying density. As expected, the distributions move

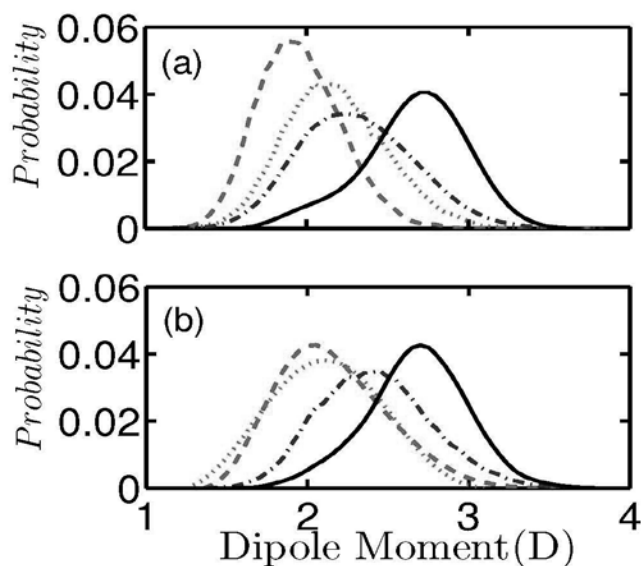


Fig.3. The distributions of molecular dipole moments in supercritical deuterated methanol. The dashed-dotted, dotted, and dashed curves are for densities 0.786, 0.563, and 0.348 g cm⁻³, respectively, at 523K. The results of (a) and (b) are for the BLYP and dispersion corrected BLYP-D functionals, respectively. The corresponding distributions for liquid methanol under ambient conditions at 300K, are also shown by the solid curves in (a) and (b). (Reproduced from Ref. [15]).

towards lower values upon decreasing the density at supercritical temperature. The average dipole moments are found to be 2.25 (2.38), 2.04 (2.12) and 1.95 (2.08) D for densities 0.768, 0.563 and 0.348 g cm⁻³, respectively, at 523 K for the BLYP (BLYP-D) functional [15]. For normal liquid methanol at 300 K, the average dipole moment is found to be 2.75 D by using the same method for the BLYP functional which can be compared with the experimental value of 2.87 D for liquid methanol [26]. The present results clearly reveal a reduction of the polarity due to diminished polarization effects upon increasing the temperature and decreasing the density. At higher density supercritical methanol, hydrogen bonds still exist to a noticeable extent as confirmed by our hydrogen bond calculations which lead to substantial polarization effects. The number of such hydrogen bonds in methanol is diminished at lower densities at the supercritical temperature and hence the electric field induced by surrounding methanol molecules through hydrogen bonds is also substantially diminished. This diminished electric field reduces the polarization of the electronic charge distributions which, in turn, reduces the molecular dipole moments in these supercritical methanol systems [15].

5 Concluding remarks



In this study, we have made a brief review of our recent *ab initio* molecular dynamics studies of the hydrogen bonding, vibrational frequencies and polarity of normal and supercritical methanol for varying density [13-15]. Among other properties, we have looked at the frequency-structure correlations of methanol molecules in both supercritical and normal liquid methanol. It is found that hydrogen bonds still persist to some extent in the supercritical state of methanol. However, at lower density of supercritical methanol, the number of hydrogen bonds decreases so much that the free or dangling OH modes play more dominant roles in determining the solvation and vibrational properties of supercritical methanol [15]. The dipole moment of methanol is also reduced significantly with increase of temperature and decrease of density [15]. The reduced hydrogen bonding and dipole moments, combined with enhanced thermal effects, are believed to be primary reasons for very different solvent properties of supercritical methanol than those of normal liquid methanol.

Acknowledgment

We gratefully acknowledge financial supports from Department of Science and Technology (DST) and Council of Scientific and Industrial Research (CSIR), Government of India.

References

1. M.M. Hofmann and M.S. Conradi, J. Phys. Chem. B 102, 263(1998).
2. T. Yamaguchi, C.J. Benmore and A.K. Soper, J. Chem. Phys. 112, 8976(2000).
3. D. S. Bulgarevich, Y. Horikawa, and T. Sako, J. Super critical Fluids 46, 206 (2008).
4. D. S. Bulgarevich, K. Otake, T. Sako, T. Sugeta, Y. Takebayashi, C. Kamizawa, D. Shintani, A. Negishi, and C. Tsurumi, J. Chem. Phys. 116, 1995(2002).
5. T. Ebukuro, A. Takami, Y. Oshima and S. Koda, J. Super critical Fluids 15, 73 (1999).
6. M. Yao and Y. Hiejima, J. Mol. Liq. 96, 207(2002).
7. T. Yamaguchi, N. Matubayasi, and M. Nakahara, J. Phys. Chem. A 108, 1319 (2004).
8. M. Chalaris and J. Samios, J. Phys. Chem. B 103, 1161(1999).
9. J.-M. Andanson, P. A. Bopp, and J.-C. Soetens, J. Mol. Liq. 129, 101(2006).
10. T. Yamaguchi, N. Matubayasi, and M. Nakahara, J. Mol. Liq. 119, 119(2005).
11. C. A. Eckert, B. L. Knuston, P. G. Debenedetti, Super critical fluids as solvents for chemical and materials processing, Nature 383(1996) 313-318 and references there in.
12. T. Nakagawa, H. Ozaki, T. Kamitanaka, H. Takagi, T. Matsuda, T. Kitamura and T. Harada, J. Super critical Fluids, 27, 255(2003).
13. V.K. Yadav, A. Karmakar, J. Roy Choudhuri and A. Chandra, Chem. Phys. 408,36(2012).
14. V.K. Yadav and A. Chandra, Chem. Phys. 415, 1(2013).
15. V.K. Yadav and A. Chandra, J. Chem. Phys. 138, 224501(2013).
16. R. Car, M. Parrinello, Phys. Rev. Lett. 55, 2471(1985).
17. D. Marx, J. Hutter, *Ab Initio* Molecular Dynamics: Basic Theory and Advanced Methods (Cambridge University Press, Cambridge, 2009).
18. J. Hutter, A. Alavi, T. Deutsch, M. Bernasconi, S. Goedecker, D. Marx, M. Tuckerman, and M. Parrinello, CPMD Program, MPI für Forschung und IBM Zurich Research Laboratory.
19. A.D.Becke, Phys. Rev. A38(1988) 3098; C.Lee, W.Yang, and R.G.Parr, Phys. Rev. B 37, 785(1988).
20. S. Grimme, J. Comput. Chem. 25, 1463(2004); J. Comput. Chem. 27, 1787 (2006).
21. S. Grimme, J. Antony, T. Schwabe, and C. Muck-Lichtenfeld, Org. Biomol. Chem. 5, 741(2007).
22. L. V. Vela-Arevalo, S. Wiggins, Int. J. Bifur. Chaos. 11, 1359(2001).
23. A. Semparathi and S. Keshavamurthy, Phys. Chem. Chem. Phys. 5, 5051(2003).
24. B.S.Mallik, A.Semparathi, and A. Chandra, J. Phys. Chem. A 112,5104(2008)
25. B. S. Mallik and A. Chandra, J. Phys. Chem. A 112, 13518(2008).
26. A.L. McClellan, Tables of Experimental Dipole Moments, Raha Enterprises, El Cerrito, CA(1989).

	<p><i>Vivek Kumar Yadav</i> obtained his B.Sc. and M.Sc. from D.D.U. Gorakhpur University, Gorakhpur, in 2001 and 2003, respectively. He obtained an M. Phil. in Chemistry from the University of Delhi, Delhi, in 2006. Subsequently, he joined the Chemistry Department of IIT Kanpur for his Ph.D. in 2007. He has submitted his Ph.D. thesis and he should be joining a research group outside India for his postdoctoral research in near future. His Ph.D. work involves theoretical studies of the dynamics of hydrogen bonded fluids under normal and supercritical conditions through <i>ab initio</i> molecular dynamics simulations.</p>
	<p><i>Amalendu Chandra</i> received his B.Sc and M.Sc. from the University of Burdwan, India, in 1984 and 1986, respectively, and his Ph.D. from Indian Institute of Science, Bangalore, in 1991. He was an Izaak Walton Killam postdoctoral fellow at the University of British Columbia for two years before joining the faculty of Department of Chemistry, Indian Institute of Technology Kanpur, in 1993. He is currently holding the position of Sajani Kumar Roy Memorial Chair Professor at IIT Kanpur. He is a Fellow of Indian Academy of Sciences, Bangalore, and Indian National Science Academy, New Delhi. He received the Shanti Swarup Bhatnagar Prize from the Council of Scientific and Industrial Research in 2007 and J.C. Bose National Fellowship from the Department of Science and Technology in 2013. His research interests include theoretical and computational studies of chemical dynamics in liquids, interfaces and clusters using both classical and quantum methods.</p>

Ab initio Molecular Dynamics and DFT studies on (HF)_n [n = 2 - 10] clusters

Sukanta Mondal, Sudip Pan and Pratim Kumar Chattaraj*

Department of Chemistry and Center for Theoretical Studies, Indian Institute of Technology,
Kharagpur, 721302, India.

*E-mail: pkc@chem.iitkgp.ernet.in,

Abstract

A detailed study is carried out on (HF)_n [n = 2 - 10] clusters using density functional theory and *ab initio* molecular dynamics simulation. Obtained minimum energy structures of (HF)_n clusters are investigated by simulation at 298 K in a 10 ps time scale. Our study reveals that (HF)₄ and (HF)₆ clusters are the most stable among all the studied systems and for the (HF)_n systems, where n is greater than 8, the structures are deformed resulting in the formation of (HF)₈ ring at larger time scale. Thorough study is also carried out to understand the nature of bonding therein, taking (HF)₄ cluster as a case study. Different reactivity descriptors based on conceptual density functional theory lend additional insights into the characteristics of those clusters.

1. Introduction

Hydrogen fluoride is an important component of numerous pharmaceutical products, refrigerants, herbicides and fluorescent light bulbs. Water and hydrogen fluoride are among the most widely studied hydrogen bonded materials in all physical states. Clusters of hydrogen-bonded molecules are extremely important as model systems in the study of intermolecular interactions and chemical reactivity [1, 2]. The study of HF clusters can also be useful in understanding condensed phase properties. There have been several studies on HF clusters. Solid hydrogen fluoride is composed of zigzag chains of the HF molecule [3]. In the gas phase, the cyclic structures of (HF)_n are believed to be more stable than their linear counterparts for n ≥ 3 [4]. In an experimental study, Janjen and Bartell found out ring like six membered structure of HF in gas phase [5]. From the experimental evidence Duff and Holzer reassigned the previously inferred C_{4h} configuration [6] of the HF tetramer by a chain like geometry and added that HF forms ring like six membered structures too in SF₆ liquid at 300 K [7]. They also found very low concentration (molar ratio 1 in 1000) of HF monomer. It is reported that the most probable structure of HF at 293 K is a zigzag chain with six or seven molecules and at lower temperature (190 K) just before solidification the chains become longer and may contain eight HF molecules [8]. Zhang et al. [9] studied HF vapor by MC simulation using a modified central force model potential developed by Klein and McDonald [10] and reported that (HF)₄ is a very important species in physical hydrogen fluoride vapor. In the year 2003, Guedes et al. [11] reported (HF)₂₋₁₀ clusters with their geometries but did not mention

their bonding and stability and how do they change with time. We analyze here the bonding pattern of HF rings by considering (HF)₄ as a representative. We introduce a few more HF ring clusters with the help of thermochemical data and conceptual density functional theory (CDFT). Finally, we do an *ab initio* molecular dynamics simulation to see the fate of these HF clusters through a small (picosecond) time window.

2. Theory and computation:

Stability of molecular systems can be analyzed by using hardness (η) and electrophilicity (ω) in conjunction with the associated electronic structure principles like the maximum hardness principle [12-15] (MHP) and minimum electrophilicity principle [15, 16] (MEP). For an N-electron system, the electronegativity [17-18] (χ), hardness [19, 20] (η) and electrophilicity (ω) [21] can be defined as follow:

$$\chi = -\mu = -\left(\frac{\partial E}{\partial N}\right)_{v(\vec{r})} \quad (1)$$

$$\eta = \left(\frac{\partial^2 E}{\partial N^2}\right)_{v(\vec{r})} \quad (2)$$

$$\omega = \frac{\mu^2}{2\eta} = \frac{\chi^2}{2\eta} \quad (3)$$

Here E , μ and $v(\vec{r})$ are the total energy of the N-electron system, chemical potential and external potential, respectively.

A finite difference approximation to Eqs.1 and 2 can be expressed as:

$$\chi = \frac{I + A}{2} \quad (4)$$

$$\text{and} \quad \eta = I - A \quad (5)$$

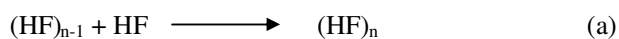
where I and A are the ionization potential and electron affinity of the system, respectively, and are calculated by utilizing the energies of the corresponding frontier molecular orbitals through Koopmans' theorem [22]. It is known that the validity of Koopmans' theorem is within the Hartree-Fock theory but one can use the same approach with the help of Janak's theorem [23] in Kohn-Sham computations.

The scaled hardness, $\tilde{\eta}$ [24] has been calculated as

$$\tilde{\eta} = \frac{\eta}{\chi^{1/3}} \quad (6)$$

HF rings are modeled according to the structures previously reported by Guedes et al. [11] and $\{(HF)_m\}_p$ ring clusters are modeled by arranging HF rings. Graphical software, GaussView 5 [25] is used for the modeling and analysis of different input and output geometries. All the optimizations, frequency calculations and molecular dynamics simulations are done using Gaussian 09 package [26]. All the modeled structures are optimized using the ω B97X-D [27] functional containing empirical dispersion in conjunction with 6-311+G(d,p) basis set. Harmonic vibrational frequencies are calculated at the same level of theory. Absence of any imaginary frequency confirms that the structures correspond to minima on the potential energy surface.

Working equations (7) and (8) are employed to calculate the clustering energy, clustering enthalpy and free energy change with an increase in the number of HF units for the formation of HF clusters by using the scheme (a).



$$\Delta E_{(HF)_n} = -[E_{(HF)_n} - \{E_{(HF)_{n-1}} + (E_{HF})\}] \quad (7)$$

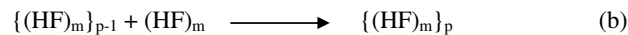
where E is clustering energy for the formation of $(HF)_n$.

$$\Delta X_{(HF)_n} = [X_{(HF)_n} - \{X_{(HF)_{n-1}} + (X_{HF})\}] \quad (8)$$

Where $\Delta X_{(HF)_n}$ is clustering enthalpy, when $X=H$, and it is clustering free energy when $X=G$. $X_{(HF)_n}$, $X_{(HF)_{n-1}}$ and X_{HF} denote enthalpy (when $X=H$) and free energy (when $X=G$) of $(HF)_n$ cluster, $(HF)_{n-1}$ cluster and HF monomer, respectively.

Working formulae (9) and (10) are used to calculate the clustering energy, clustering enthalpy and free energy

change with an increase in the number of $(HF)_m$ rings for the formation of $\{(HF)_m\}_p$ clusters by using the following schematic equation (b):



$$\Delta E_{\{(HF)_m\}_p} = -[E_{\{(HF)_m\}_p} - \{E_{\{(HF)_m\}_{p-1}} + (E_{(HF)_m})\}] \quad (9)$$

$$\Delta X_{\{(HF)_m\}_p} = [X_{\{(HF)_m\}_p} - \{X_{\{(HF)_m\}_{p-1}} + (X_{(HF)_m})\}] \quad (10)$$

where ΔE and ΔX carry the same meaning as above for the formation of $\{(HF)_m\}_p$ clusters.

Dynamics of the HF clusters are studied through *ab initio* molecular dynamics simulation [28], using Atom Centered Density Matrix Propagation (ADMP) [29-31] technique included in the Gaussian 09 program package. The simulations are performed at DFT-D-B3LYP/6-31G(d) [32-35] level of theory with initial geometries corresponding to minimum energies (calculated at ω B97X-D/6-311+G(d,p) level) of different HF clusters. Simulation is done at 298 K to see the dynamical behavior of the HF rings in gaseous state. Initial nuclear kinetic energies of the systems are generated by using a Boltzmann distribution. Velocity scaling thermostat is used to maintain the temperature throughout the simulation. We used default random number generator seed, implemented in G09 to initiate the initial mass weighted Cartesian velocity. In all the cases simulation is done by keeping the fictitious electronic mass as 0.1 amu.

3. Results and Discussion

3.1. DFT study on $(HF)_n$ clusters

All the HF clusters are modeled by maintaining planar geometrical shapes, e.g., for six HF units, hexagon; using Gauss View 5 [25]. $\{(HF)_3\}_2$, $\{(HF)_4\}_2$, $\{(HF)_3\}_3$ and $\{(HF)_5\}_2$ structures are modeled by arranging energy minima $(HF)_3$, $(HF)_4$, $(HF)_5$ rings. All the energy minima structures are given in Figure S1 (see Supplementary Information). Among these HF clusters, it is observed that in $\{(HF)_5\}_2$ the $(HF)_5$ rings are not planar. We have tried to get $\{(HF)_5\}_2$ with planar $(HF)_5$ rings but it resulted in structures with imaginary harmonic vibrational frequencies. Through the correction of these imaginary harmonic vibrational frequencies by following the displacement vector of vibration leads to the non planar $(HF)_5$ ring containing structure with no imaginary frequency.

Clustering energy (ΔE , kcal/mol), clustering enthalpy (ΔH , kcal/mol) and clustering free energy (ΔG , kcal/mol) for the formation of $(HF)_n$ clusters are given in Table 1.

ΔE and ΔH values of $(\text{HF})_n$ indicate that $(\text{HF})_n$ systems are stable. Scaled hardness ($\tilde{\eta}$, eV) and electrophilicity (ω , eV) of $(\text{HF})_n$ clusters are calculated and provided in Table 1. As we go from dimer to tetramer the value of ΔE increases and then decreases up to $(\text{HF})_{10}$ (in case of octamer and nonamer a little increase is observed); which indicates that the tetramer is the most stable among all the studied clusters. In all the cases, the calculated ΔH values are negative and for tetramer, pentamer and hexamer, we get negative free energy changes at 298K and hence these three HF rings are more stable in comparison to others. However, other clusters may become stable at lower temperature where favorable ΔH term dominates over unfavorable $T\Delta S$ term. ΔE , ΔH and ΔG values for the formation of tetramer units suggest that the tetramer is the most stable HF ring compound in gas phase supporting the work of Zhang et al [9]. From the scaled hardness and electrophilicity values, it is clear that from dimer to decamer, tetramer contains the highest and the lowest hardness and electrophilicity values, respectively, whereas octamer contains the highest and the lowest hardness and electrophilicity values, respectively, from heptamer to decamer. According to both maximum hardness principle and minimum electrophilicity principle, tetramer is the most stable and octamer is reasonably more stable than the other larger analogues.

Table 1. Clustering energy (ΔE , kcal/mol), clustering enthalpy (ΔH , kcal/mol), clustering free energy, scaled hardness ($\tilde{\eta}$, eV) and electrophilicity (ω , eV) of $(\text{HF})_n$ ($n=2$ to 10) clusters.

System	ΔE	ΔH	ΔG	$\tilde{\eta}$	ω
$(\text{HF})_2$	4.946	-3.976	2.098	8.389	1.098
$(\text{HF})_3$	10.946	-9.346	0.051	9.202	1.096
$(\text{HF})_4$	13.277	-11.693	-2.516	9.264	1.087
$(\text{HF})_5$	10.701	-9.709	-1.876	9.221	1.127
$(\text{HF})_6$	9.166	-8.182	-1.210	9.102	1.163
$(\text{HF})_7$	8.814	-7.511	0.782	9.042	1.187
$(\text{HF})_8$	8.815	-7.555	0.321	9.045	1.175
$(\text{HF})_9$	8.844	-7.439	0.611	8.954	1.200
$(\text{HF})_{10}$	8.588	-7.293	-0.186	8.921	1.211

Among the clusters of type $\{(\text{HF})_m\}_p$, it is observed (Table 2) that $\{(\text{HF})_3\}_2$ has higher tendency to be formed as the value of ΔE is the highest and ΔH is most negative among others. But in all these clusters calculated free energy change is positive which indicates that these clusters may not be achievable at 298K.

Table 2. Clustering energy (ΔE , kcal/mol), clustering enthalpy (ΔH , kcal/mol), clustering free energy, scaled hardness ($\tilde{\eta}$, eV) and electrophilicity (ω , eV) of $\{(\text{HF})_m\}_p$ ($m=3$ to 5, $p=2, 3$) clusters.

System	ΔE	ΔH	ΔG	$\tilde{\eta}$	ω
$\{(\text{HF})_3\}_2$	2.971	-1.658	7.388	8.719	1.228
$\{(\text{HF})_4\}_2$	2.222	-0.845	9.452	8.793	1.248
$\{(\text{HF})_3\}_3$	6.153	-3.556	17.523	8.536	1.289
$\{(\text{HF})_5\}_2$	2.194	-0.985	9.423	8.752	1.289

3.2. Nature of bonding:

It is known that the stabilization in $(\text{HF})_n$ clusters originates from the H-bonding between two adjacent HF units. To get more insight into the bonding, we have performed NPA charge calculation and have generated plots of electron density, total electrostatic potential, Laplacian of electron density by taking $(\text{HF})_4$ as a case study with the aid of the Multiwfn package [36]. The NPA charges at all centers of $(\text{HF})_n$ clusters studied at $\omega\text{B97X-D/6-311+G(d,p)}$ level are provided in Table 3 whereas surface map of electron density and contour plots of total electrostatic potential and Laplacian of electron density are

Table 3. The NPA charge ($Q_{K'}$, au) at each center of $(\text{HF})_n$ clusters calculated at $\omega\text{B97X-D/6-311+G(d,p)}$ level.

Clusters	$Q_{H'}$, au	$Q_{F'}$, au
HF	+0.549 e ⁻	-0.549 e ⁻
$(\text{HF})_2$	+0.558 e ⁻ (H-bond-ed), +0.569 e ⁻ (free)	-0.556 e ⁻ (H-bonded), -0.571 e ⁻ (free)
$(\text{HF})_3$	+0.576 e ⁻	-0.576 e ⁻
$(\text{HF})_4$	+0.578 e ⁻	-0.578 e ⁻
$(\text{HF})_5$	+0.580 e ⁻	-0.580 e ⁻
$(\text{HF})_6$	+0.581 e ⁻	-0.581 e ⁻
$(\text{HF})_7$	+0.581 e ⁻ , +0.582 e ⁻	-0.580 e ⁻ , -0.581 e ⁻ , -0.583 e ⁻
$(\text{HF})_8$	+0.581 e ⁻ , +0.582 e ⁻	-0.581 e ⁻ , -0.582 e ⁻
$(\text{HF})_9$	+0.580 e ⁻ , +0.581 e ⁻ , +0.582 e ⁻ , +0.583 e ⁻	-0.577 e ⁻ , -0.579 e ⁻ , -0.580 e ⁻ , -0.581 e ⁻ , -0.584 e ⁻ , -0.589 e ⁻
$(\text{HF})_{10}$	+0.579 e ⁻ , +0.580 e ⁻ , +0.581 e ⁻ , +0.582 e ⁻ , +0.583 e ⁻	-0.577 e ⁻ , -0.578 e ⁻ , -0.579 e ⁻ , -0.581 e ⁻ , -0.582 e ⁻ , -0.585 e ⁻ , -0.586 e ⁻

shown in Figures 1 and 2 respectively. The NPA charges on H and F centers of a single HF molecule are $+0.549 e^-$ and $-0.549 e^-$, respectively. Table 3 presents the charges on H and F centers which gradually change with an increase in the cluster size up to $(\text{HF})_7$. Due to symmetric structures, all H atoms are equivalent to each other and all F atoms are also equivalent to each other in $(\text{HF})_n$; $n=3-6$. However, for clusters having $n>6$, more than one nonequivalent H and F atoms exist resulting in different charges on them. The higher charge separation in H-bonded $(\text{HF})_n$ clusters results due to the pulling of electron cloud from H center by F atom and thus by increasing the positive charge on H and negative charge on itself.

In the upper portion of the electron density plot (Figure 1) different heights and colors of the shaded surface represent different values of electron density, whereas the lower portion shows the colored filled map for the same. Figure 1 shows that the electron density is accumulated on highly electronegative F atom with almost no electron density in between two HF units.

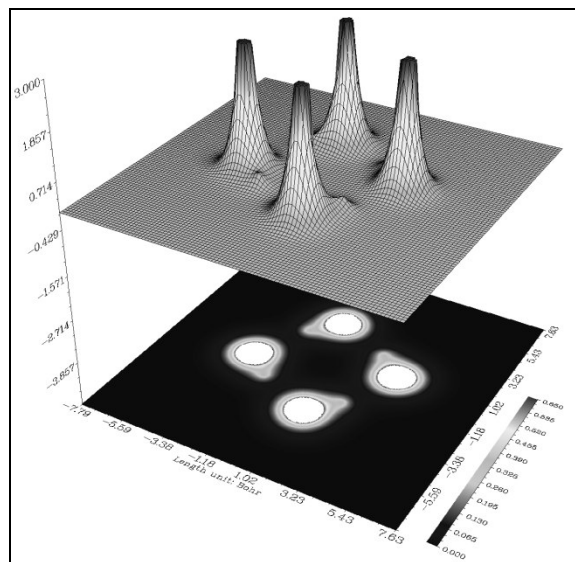


Figure 1. Shaded surface map with projection of electron density of $(\text{HF})_4$ cluster generated at $\omega\text{B97X-D/6-311+G(d,p)}$ level.

The bold blue line in Figure 2(a) shows the van der Waals (vdW) surface. From the contour plot of total electrostatic potential, it is clear that the H atoms in $(\text{HF})_4$ are positively charged whereas F atoms are negatively charged, since the local vdW surface near the H atoms largely intersects the solid green line, the region has a positive electrostatic potential whereas such type of intersection is absent closed to F atoms. This aspect of the plot is well correlated with NPA charge on each atom. An analysis of the Laplacian of electron density, $\nabla^2\rho(\mathbf{r})$ provides additional insights into the bonding situation

(Figure 2(b)). The blue dashed lines represent areas of charge concentration ($\nabla^2\rho(\mathbf{r}) < 0$) while the green solid lines show areas of charge depletion ($\nabla^2\rho(\mathbf{r}) > 0$) [37]. Further, area of charge concentration between two atoms implies the presence of covalent bond. Figure 2(b) shows the presence of strong covalent bonding between H and F atoms in HF molecule whereas the interaction between two HF molecules is dominantly of ionic type having hardly any covalent contribution.

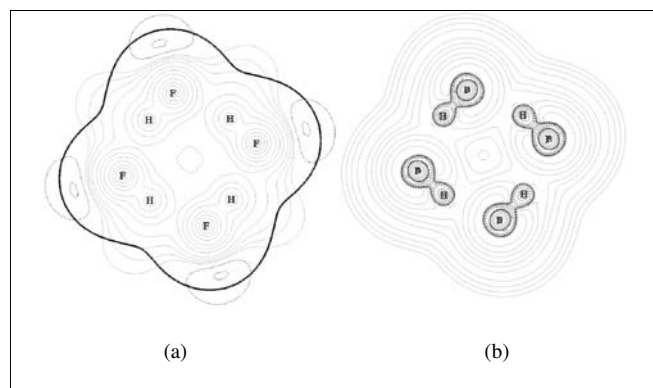


Figure 2. Contour plot of total electrostatic potential (a) and Laplacian of electron density (b) of $(\text{HF})_4$ cluster studied at $\omega\text{B97X-D/6-311+G(d,p)}$ level. (Solid lines represent the region of positive electrostatic potential whereas dotted lines represent the region of negative electrostatic potential in (a) and green solid lines show areas of the charge depletion ($\nabla^2\rho(\mathbf{r})>0$) and blue dotted lines show areas of the charge concentration ($\nabla^2\rho(\mathbf{r})<0$ in (b)).

3.3. *ab initio* simulation:

An *ab initio* simulation is done at 298 K for all the HF clusters. In this section, we have discussed the occurred structural changes of the $(\text{HF})_n$ rings and $\{(\text{HF})_m\}_p$ rings within a stipulated time scale. First we run the simulation up to 2 picoseconds (ps) for all the clusters. It is observed that except for heptamer, hexamers [both $(\text{HF})_6$ and $\{(\text{HF})_3\}_2$ rings], and tetramer some structural changes occur in all other studied systems. But the observed structural change in octamer is less significant. Then we proceed up to 4 ps with the systems in which structural changes are observed at 2ps. At 3 ps the $(\text{HF})_3$ forms a chain isomer and at 4 ps the pentamer decomposes to form tetramer whereas no further structural change is observed in octamers [for both $(\text{HF})_8$ and $\{(\text{HF})_4\}_2$]. But remaining systems, viz., decamers [$(\text{HF})_{10}$ and $\{(\text{HF})_5\}_2$] and nonamers [$(\text{HF})_9$ and $\{(\text{HF})_3\}_3$] undergo significant structural deformation. In Figure 3, all the structures starting from trimer to octamers are given.

In the case of decamers [$(\text{HF})_{10}$ and $\{(\text{HF})_5\}_2$] and nonamers [$(\text{HF})_9$ and $\{(\text{HF})_3\}_3$], it is observed that up to 2 ps, $(\text{HF})_{10}$ remains intact without any structural deformation

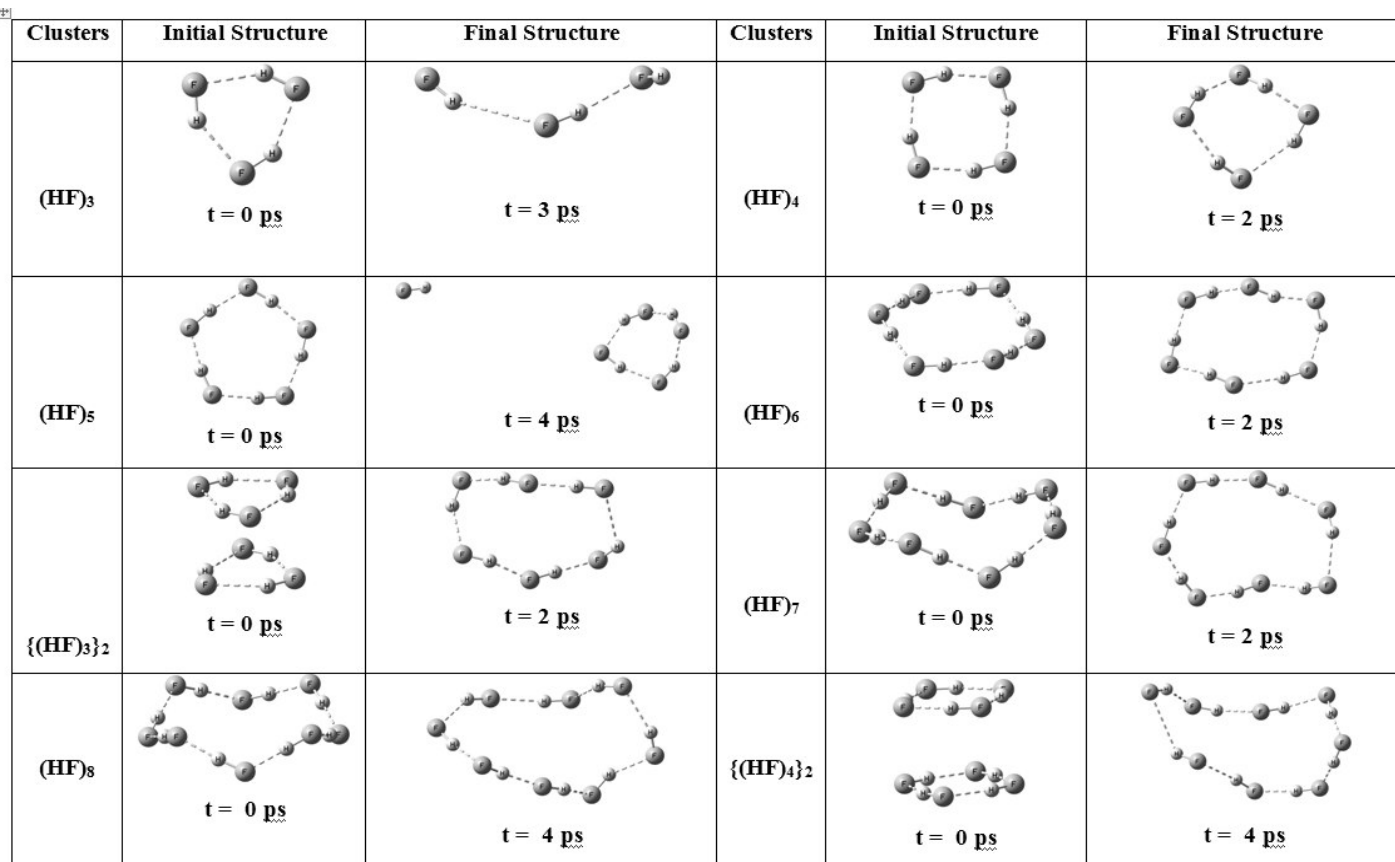


Figure 3: Initial structures (optimized local minima structures) and their simulated structures of (HF)_n isomers (n = 3 to 8) at the mentioned time.

but {(HF)₅}₂ ruptures to form one heptamer and a trimer chain which are connected through hydrogen bond. Similar phenomenon is observed in case of nonamers; a little deformation is observed in (HF)₉ but {(HF)₃}₃ takes a strained ribbon like geometry. Then at 4 ps we observed that (HF)₁₀ decomposes to form octamer and dimer which remain together through hydrogen bond, whereas {(HF)₅}₂ forms heptamer where one HF monomer remains hydrogen bonded to the heptamer and other two monomers move apart. The pictures of nonamers are different, (HF)₉ remains as it is but {(HF)₃}₃ decomposes from the ribbon like strained geometry to form octamer and monomer in which the monomer unit remains hydrogen bonded to the octamer. After that we continued the simulation for longer time (up to 10 ps). When simulation stopped at 10 ps we have observed that all the decamers and nonamers decomposed to form octamer. (HF)₁₀ decomposes to form octamer and dimer, the dimer remains hydrogen bonded to the octamer. The detailed pictures are given in Figure 4 at different time steps.

4. Conclusion:

(HF)₄ (as suggested by Zhang et al.) [9] and (HF)₆ are the most and the second most stable ring

clusters, respectively, among all (HF)_n {n = 3 to 10} ring clusters. At 3 ps, (HF)₃ ring cluster attains linear chain configuration. (HF)₈ is found to be the most stable one among the other isomer of octamer [(HF)₄]₂, nonamers [(HF)₉ and {(HF)₃}₃] and decamers [(HF)₁₀ and {(HF)₅}₂]. (HF)₈ is the resulting ring cluster, which is obtained by ab initio simulation of (HF)_n clusters (where n ≥ 8) up to 10 ps time scale. NPA calculation shows that charge separation between hydrogen and fluorine of (HF)_n (n ≤ 6) changes gradually up to n=6. Major interaction among HF units in (HF)_n ring clusters is electrostatic in nature.

5. Acknowledgments:

We are delighted to dedicate this paper to Professor Swapan Kumar Ghosh on his sixty fourth birthday. We thank Indo-EU (HYPOMAP) project, UGC and CSIR for financial assistance. One of us (P.K.C.) would like to thank the DST, New Delhi, for the J.C. Bose National Fellowship. We would like to thank Drs. Chiranjib Majumder and Chandra Nath Patra for kindly inviting us to write this article.

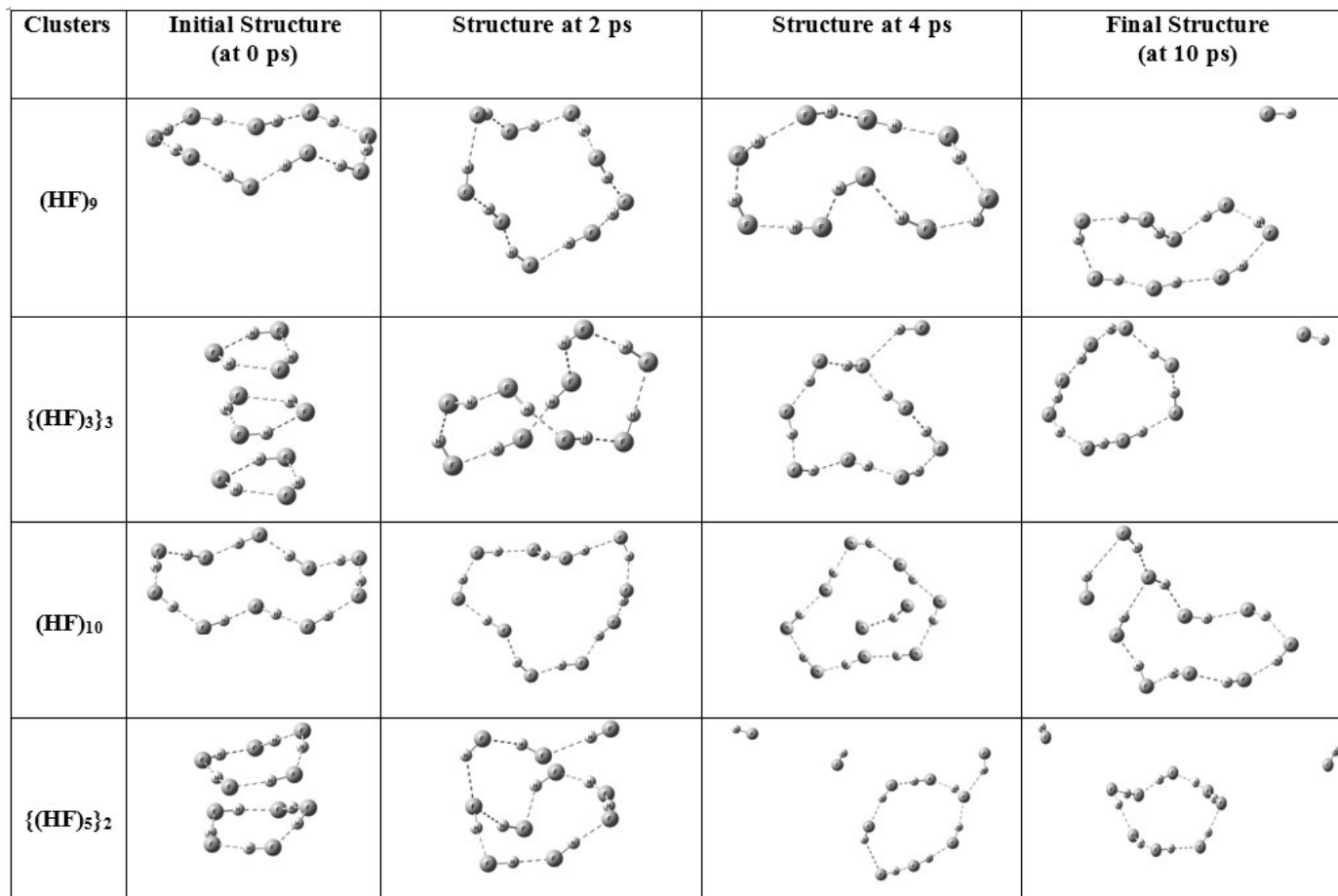





Figure 4: Initial structures (optimized local minima structures) and their simulated structures of (HF)_n isomers (n>8) at the mentioned time.

References:

- Cotton, F. A.; Wilkinson, G. *Advanced Inorganic Chemistry*, 5th ed. Wiley, New York, **1988**, Chap. 3.
- Scheiner, S. *Hydrogen Bonding: A Theoretical Perspective*, Oxford University Press, New York, **1997**.
- Johnson, M. W.; Sandor, E.; Arzi, E. *Acta Cryst.* **1975**, B31, 1998-2003.
- Dyke, T. R.; Howard, B. J.; Klemperer, W. *J. Chem. Phys.* **1972**, 56, 2442-2454.
- Janzen, J.; Bartell, L. S. *J. Chem. Phys.* **1969**, 50, 3611-3618.
- Huong, P. V.; Couzi, M. *J. Chim. Phys.* **1969**, 66, 1309-1311.
- Duff, Le. Y. and Holzer, W. *J. Chem. Phys.* **1974**, 60, 2175-2178.
- Desbat, B. P.; Huong, V. *J. Chem. Phys.* **1983**, 78, 6377-6383.
- Zhang, C.; Freeman, L. D. and Doll, J. D. *J. Chem. Phys.* **1989**, 91, 2489-2497.
- Klein, M. L. and McDonald, I. R. *J. Chem. Phys.* **1979**, 71, 298-308.
- Guedes, R. C.; do Couto, P. C. and Costa Cabral, B. J. *J. Chem. Phys.* **2003**, 118, 1272-1281.
- Pearson, R. G. *J. Chem. Edu.* **1987**, 64, 561-567.
- Parr, R.G.; Chattaraj, P. K. *J. Am. Chem. Soc.* **1991**, 113, 1854-1855.
- Ayers, P. W.; Parr, R. G. *J. Am. Chem. Soc.* **2000**, 122, 2010-2018.
- Pan, S.; Solà, M. and Chattaraj, P. K. *J. Phys. Chem. A*, **2013**, 117, 1843-1852.
- (a) Chamorro, E.; Chattaraj, P. K.; Fuentealba, P. *J. Phys. Chem. A* **2003**, 107, 7068-7072. (b) Parthasarathi, R.; Elango, M.; Subramanian, V.; Chattaraj, P. K. *Theo. Chem. Acc.* **2005**, 113, 257-266.
- Geerlings, P.; De, P. F.; Langenaeker, W. *Chem. Rev.* **2003**, 103, 1793-1873.
- Parr, R. G.; Donnelly, R. A.; Levy, M.; Palke, W. E. *J. Chem. Phys.* **1978**, 68, 3801-3807.
- Chattaraj, P. K.; Sarkar, U.; Roy, D. R. *Chem. Rev.* **2006**, 106, 2065-2091.
- Chattaraj, P. K.; Roy, D. R. *Chem. Rev.* **2007**, 107, PR46-PR74.
- Parr, R. G.; Szentpaly, L. v.; Liu, S. *J. Am. Chem. Soc.* **1999**, 121, 1922-1924.
- Koopmans, T. A. *Physica.* **1933**, 1, 104-113.
- Janak, J. F. *Phys. Rev. B.* **1978**, 18, 7165-7168.
- Ghanty, T. K. and Ghosh S. K. *J. Phys. Chem. A*, **2002**, 106, 4200-4204.
- GaussView, Version 5, R. Dennington, T. Keith, J. Millam, *Semichem Inc.* Shawnee Mission KS. **2009**.

26. M.J. Frisch et al., Gaussian09, Revision A.1, Gaussian, Inc.: Pittsburgh, PA, 2009.
27. Chai, J.-D.; Head-Gordon, M. *Phys. Chem. Chem. Phys.* **2008**, *10*, 6615-6620.
28. Marx, D.; Hutter, J.; In Proceedings of Modern Methods and Algorithms of Quantum Chemistry, Julich, Grotendorst, E.; Ed., John von Neumann Institute for Computing: Jurich, Germany, 2000.
29. Schlegel, H. B.; Millam, J. M.; Iyengar, S. S.; Voth, G. A.; Daniels, A. D.; Scuseria, G. E.; Frisch, M. J. *J. Chem. Phys.* **2011**, *114*, 9758-9763.
30. Iyengar, S. S.; Schlegel, H. B.; Millam, J. M.; Voth, G. A.; Scuseria, G. E.; Frisch, M. J. *J. Chem. Phys.* **2011**, *115*, 10291-10302.
31. Schlegel, H. B.; Iyengar, S. S.; Li, X.; Millam, J. M.; Voth, G. A.; Scuseria, G. E.; M. J. *J. Chem. Phys.* **2002**, *117*, 8694-8704.
32. Becke, A. D. *J. Chem. Phys.* **1993**, *98*, 5648-5652.
33. Lee, C.; Yang, W.; Parr, R.G. *Phys. Rev. B*, **1988**, *37*, 785-789.
34. Stephens, P. J.; Devlin, F. J.; Chabalowski, C. F.; Frisch, M. J. *J. Phys. Chem.* **1994**, *98*, 11623-11627.
35. Grimme, S. *J. Comput. Chem.* **2006**, *27*, 1787-1799.
36. Lu, T.; Chen, F. W. *J. Comput. Chem.* **2012**, *33*, 580-592.
37. Bader, R. F. W.; MacDougall, P. J. and Lau, C. D. *H. J. Am. Chem. Soc.* **1984**, *106*, 1594-1605.

	<p>Sukanta Mondal received his B.Sc. (Chemistry Honors) degree from the University of Burdwan, West Bengal. He did his M.Sc. (Chemistry) from the Department of Chemistry, University of Pune, Maharashtra. Then he joined the research group of Professor P. K. Chattaraj to pursue Ph.D. in the Department of Chemistry, Indian Institute of Technology, Kharagpur, as a UGC (Government of India) Fellow. At present he is working as a Senior Research Fellow in the same research group.</p>
	<p>Sudip Pan received his B.Sc. (Chemistry Honors) and M.Sc. (Chemistry) degrees from the Vidyasagar University, West Bengal. He joined the research group of Professor P. K. Chattaraj for his Ph.D. degree in the Department of Chemistry, Indian Institute of Technology, Kharagpur, as a CSIR (Government of India) Fellow. At present he is working as a Senior Research Fellow.</p>
	<p>Pratim Kumar Chattaraj obtained his B.Sc. and M.Sc. degrees in Chemistry from Burdwan University and his Ph.D. degree from Indian Institute of Technology Bombay. Presently he is a professor in the Department of Chemistry, Indian Institute of Technology Kharagpur and also the Convener of the Center for Theoretical Studies there. He was a postdoctoral research associate in the University of North Carolina (Chapel Hill). His research interests include density functional theory, the theory of chemical reactivity, aromaticity in metal clusters, ab initio calculations, quantum trajectories, and nonlinear dynamics. He has been invited to deliver special lectures at several international conferences and to contribute chapters to many edited volumes. Professor Chattaraj is a member of the editorial board of <i>J. Mol. Struct. (Theochem)</i>, <i>J. Chem. Sci.</i> and <i>Ind. J. Chem.</i> Among others, he was the Head of the Department and a council member of the Chemical Research Society of India. He is a Fellow of the Indian Academy of Sciences (Bangalore), the Indian National Science Academy (New Delhi), the National Academy of Sciences, India (Allahabad), and the West Bengal Academy of Science and Technology. He is a J. C. Bose National Fellow. He has edited several books, <i>Chemical reactivity theory: A density functional view, Aromaticity and metal clusters, and Quantum trajectories</i>, published by Taylor and Francis Books, Inc./CRC Press, Boca Raton, FL, and a special issue each of <i>J. Chem. Sci.</i> (on "Chemical Reactivity") and <i>J. Mol. Struct. (Theochem)</i> (with Professor A. J. Thakkar, on "Conceptual aspects of electron densities and density functionals"). He is the Editor of the book series on "Atoms, Molecules, and Clusters: Structure, Reactivity, and Dynamics" and of a two volume set (with Professor S. K. Ghosh) on "Concepts and Methods in Modern Theoretical Chemistry, Volume I: Electronic Structure and Reactivity; Volume II: Statistical Mechanics" both published by Taylor and Francis Books.</p>

First-Principles Studies of Phase Stability and Phase Transformations in Alloys

Ashok K. Arya

Materials Science Division, Bhabha Atomic Research Centre, Mumbai 400085, INDIA

Email: aarya@barc.gov.in

Abstract

The present article gives a glimpse of computational work related to phase stability and phase transformations in alloys using electronic structure methodologies based on density functional theory along with statistical mechanical tools. The latter are needed to study finite temperature effects on alloy phase stability. Two kinds of phase transformations, viz., displacive or order-disorder transformation involving clustering and ordering processes and displacive transformation involving homogeneous distortion or shuffling of atomic planes have been discussed. The computational methodology and the results of displacive transformations in Al-Li, Ni-Mo, Ni-Mo-X alloys and displacive transformation in pure Zr are briefly presented.

1. Introduction

In the modern world metallic alloys are used in an enormous variety of applications. The reasons for this ubiquitous use revolve around the possibility of modifying the properties - strength, ductility, corrosion resistance, thermal and electrical properties to meet specific engineering requirements. Tailoring properties of materials for the intended applications is one of the important aspects in the present day materials research. Since most commercial alloys are complex multiphase mixtures, it is important to have the knowledge of all the possible alloy phases that can occur in a given system: terminal solid solutions, possible ordered intermetallic phases and other disordered solid solutions. Hence, the study of alloy phase stability and order-disorder transformations is a major area of research today. The relationship between these two aspects of the alloy theory has been very aptly described by de Fontaine [1]—*“The phenomenon of ordering is intimately related to the problem of alloy phase stability for the following reason: Crystalline compounds may quite generally be considered as ordered superstructures of a lattice (or a set of sublattices) of some parent disordered phase. The theoretical study of solid state phase stability, thus, involves the energetics of all relevant lattices, of all possible states of perfect order on the various lattices (ground state superstructures) and of states of partial order (and disorder).”* A formidable problem in the context of the assessment of phase stability is that the relative stability among the competing crystal structures is usually dictated by very small energy differences between large values of the cohesive energy. Apart from this, a correct prediction implies the prediction of the lowest free energy structure among the chosen structural alternatives. This, in turn, stipulates a prior algorithm to generate all probable structures. Even when all these difficulties are overcome, it is needed to incorporate the roles of variables

like temperature and pressure in realistic terms. These are, indeed, difficult tasks.

The success of a theory of phase stability is largely determined by its ability to make predictions that are consistent with experimental observations. There is a need to be able to calculate phase stability from first-principles if the basic microscopic parameters that dictate the free energy of a phase are to be properly understood. It should also be possible to make use of such calculations for predicting phase diagrams in systems where the experimental determination of such diagrams is difficult. The understanding and prediction of phase stability in respect of disordered and ordered alloys in terms of electronic structure calculations constitute an area of considerable importance in materials science. Total energy calculations based on the *density functional theory* (DFT), which use only atomic numbers as inputs, have been very successful in the estimation of 0 K ground state properties of the elements and of ordered compounds. In fact, the implementation of the DFT by many an investigator, combined with the development of efficient linear methods for studying the electronic structure of solids, has led to fully ab initio calculations of the total energy at 0 K of pure solids, relatively simple compounds and disordered alloys. By making it possible to assess a wide range of physical properties quite close to the corresponding experimentally obtained values, these quantum mechanical total energy computations have provided very favorable evidence in support of the DFT, which can be applied, together with appropriate statistical models, to address the difficult problem of alloy stability at nonzero temperatures. A more general method for calculating the equilibrium state of matter at finite temperatures is the quantum molecular dynamics method which has been to be useful for arriving at band

structures and bonding details in respect of solids and liquids at finite temperatures.

The remaining part of this article deals with deployment of DFT based ab-initio calculations in conjunction with statistical mechanical methods to study finite temperature phase stability and order-disorder phase transformations in binary Al-Li and Ni-Mo, and ternary Ni-Mo-X (X=Al, Cr, Mn, V) alloys. The last section deals with a displacive (martensitic) structural transformation in pure Zr involving structural change from hexagonal close-packed to omega (hexagonal) structure.

2. Alloy Phase Stability

Our first-principles approach to ground state phase stability followed by the configurational thermodynamics of alloys can be schematically illustrated [2]. The steps are as follows :

1. Determination of total energies E_T^Φ of various possible superstructures (Φ) as function of volume (V), of a given alloy system, by using any electronic structure calculation method, *e.g.*, (full-potential)-linear augmented plane wave method, (full-potential)-linear muffin-tin orbital method, other plane wave based methods (pseudopotential or projector augmented wave potential).
2. Determination of configurationally averaged effective pair (or cluster) interactions which serve as inputs to the calculation of configurational energy of the system. These EPIs / ECIs can be obtained either starting from some judiciously chosen ordered configurations (Φ) or starting from a completely disordered state in which all possible configurations can be realized. Accordingly, we have used the following two alternative routes.
 - Connolly-Williams or Inversion Method (IM) [3]: In this method, the internal energy of a given configuration is expanded as a rapidly convergent sum of effective cluster interactions ($J_\gamma(V)$) weighted by corresponding cluster correlation (ECI) functions (ξ_γ^Φ),

$$E_{coh}^\Phi(V) = \sum_{\gamma=0}^{\gamma_{max}} J_\gamma(V) \cdot \xi_\gamma^\Phi$$

here the summation is over all the subclusters (γ) of a basic cluster selected. We have used tetrahedron-cluster approximation for bcc and tetrahedron-octahedron - cluster approximation for the fcc lattice. This approximations can account for first and second nearest neighbor (NN) pair interactions. The above equation can be inverted to yield the volume dependent ECIs $J_\gamma(V)$.

- Augmented Space Recursion (ASR) + Orbital Peeling (OP) [4]: In ASR, the recursion is performed in the augmented space (Hilbert (H) + Configurational (C)) using a tight-binding Hamiltonian which is sparse in nature. The ASR in conjunction with orbital peeling technique is a first-principle tool for obtaining configurationally averaged effective pair interactions (EPI's) upto an arbitrary coordination shell. For example, we have calculated EPI's upto the fourth NN pairs for Ni-Mo alloys, as will be discussed below.
- 3. Determination of configurational free energy by either using mean-field based methods, *e.g.*, Static Concentration Wave (SCW) model or using the generalized (cluster-based) mean field method, *e.g.*, Cluster Variation Method (CVM). The former takes into account only long-range correlations but neglects local correlations.
 - In the SCW model [5], the occupation probability, $N(\mathbf{r})$, at any position, \mathbf{r} , is expanded as a sum of static concentration waves as:

$$N(\mathbf{r}) = \sum_{j=1}^N Q(\mathbf{k}) \cdot e^{-i\mathbf{k}_j \cdot \mathbf{r}}$$

where $Q(\mathbf{k})$'s are the concentration wave amplitudes given by

$$Q(\mathbf{k}) = \frac{1}{N} \sum_{j=1}^N N(\mathbf{r}_j) \cdot e^{i\mathbf{k}_j \cdot \mathbf{r}}$$

The internal energy, in the pair approximation upto an arbitrary coordination shell, is given as

$$E = \frac{N}{2} \sum_{l=1}^N J(\mathbf{k}_l) \cdot Q(\mathbf{k}) \cdot Q^*(\mathbf{k})$$

where the star (*) indicates the complex conjugate of the amplitude of the corresponding concentration wave, N is the total number of lattice sites and $J(\mathbf{k})$, the Fourier transforms of the pair interactions.

The expression for the configurational entropy, in the mean-field approximation, is given as

$$S = -k_B \sum_{i=1}^N [N(\mathbf{r}_i) \ln N(\mathbf{r}_i)] [(1 - N(\mathbf{r}_i)) \ln(1 - N(\mathbf{r}_i))]$$

where k_B is the Boltzmann constant. The free energy ($F=E-TS$) is, thus obtained as a function of temperature (T), composition (c) and order parameter (η).

- Cluster Variation Method (CVM) [6]: In the CVM, one divides the whole lattice into smaller units (clusters (γ)) and the configuration of an N-point system is then classified into groups with the number of clusters having same configuration. The probability density, $P(\{\sigma_i\})$ of a γ -cluster to occur in $\{\sigma_i\}$ configuration is given by: $P(\{\sigma_i\}) = N_\gamma(\{\sigma_i\}) / N_\gamma$, where the numerator is the number of γ -clusters having the $\{\sigma_i\}$ configuration and the denominator denotes total number of such clusters. The configurational energy and entropy are expressed in terms of such probability densities of all groups of clusters and their sub-clusters.

Instability analysis: An alloy system which is amenable to thermodynamic analysis should be such that the structure of the ordered intermetallic phase can be generated by replacement of atoms in the lattice of the parent disordered solid solution (coherent structures). The process of collection of solute atoms in a localized region for attaining local solute enrichment - known as clustering - may occur simultaneously or sequentially with ordering which involves the organization of solvent and solute atoms in a superlattice structure. In such situations free energy of the ordered phase can be expressed as a function of the order parameter, which in turn is related to the amplitude of the concentration wave associated with ordering. In order to examine the presence of clustering and ordering instabilities of the solid solution with concentration waves of appropriate wave vectors, the minimized value of the free energy is plotted against the solute concentration to check for the presence of inflection points. Depending on the values of the effective pair interaction parameters, the free energy-composition plots for the random as well as the ordered fcc solid solutions may exhibit the following four possibilities [7, 8]:

- The disordered solid solution is metastable with respect to both ordering and clustering
- The disordered solid solution is initially unstable with respect to ordering but metastable against clustering. The ordering of the solid solution to the optimum level can, subsequently, introduce a clustering instability in the ordered structure.
- The disordered solid solution is initially unstable with respect to clustering but metastable with respect to ordering. In this situation, clustering occurs first which may make the solute-enriched regions unstable with respect to ordering.
- The disordered solid solution is unstable with respect to both clustering and ordering.

A solution is considered stable, critical or unstable according to whether the second derivative of free energy $F'' > 0$, $F'' = 0$, or $F'' < 0$, respectively. $F'' = 0$ corresponds to the point at which the instability develops in the solution. The instability lines in the T-c plane are defined as follows:

- T_i^- : The line below which the solid solution is unstable with respect to congruent ordering.
- T_i^+ : The line above which the ordered solid solution becomes unstable with respect to spontaneous congruent disordering.
- T_{cs} : The line below which spinodal clustering instability develops only after the system undergoes ordering to a certain extent.
- T_s : The line below which the disordered phase becomes unstable with respect to clustering and the two equilibrium phase boundaries (T_{eq} 's) defining the ordered, disordered and the two-phase region.

2.1 Al-Li System

The precipitation of the metastable δ' -phase ($L1_2$ -structured Al_3Li phase) from dilute Al-Li alloys has been chosen in the present work, as in this system the interplay between the clustering and the ordering processes has been investigated theoretically as well as experimentally. Experimental work in dilute Al-Li alloys has focused attention on the mechanism of the formation of the δ' -phase from the fcc solid solution. Our first-principles calculations [2] for different superlattice structures in the system have yielded ground state physical properties like formation energies, bulk moduli, equilibrium lattice parameters and cohesive energies (Fig. 1), which show excellent agreement with the available experimental values.

The effective multisite interactions have been determined by using Connolly-Williams prescription in the tetrahedron-octahedron (TO) cluster approximation (Fig. 2) for the fcc lattice. The values for the first and the second ($J_2(1)$ and $J_2(2)$) nearest neighbour interactions for the fcc alloys, at an average equilibrium volume of 107.0 (a.u.)^3 , are 4.882×10^{-3} and $-1.463 \times 10^{-4} Ry$ respectively. The $L1_2$ structure is generated by the superimposition of three (100) concentration waves. The special point, k , for the $L1_2$ ordering is $[100]^*$. The resulting Landau plots (free energy versus order parameter, see Fig. 3(a)) have pointed out the temperatures below which instabilities with respect to ordering develops. Free energy-composition plots have been used for identifying the positions of the phase boundaries and of the critical spinodal. The results of this

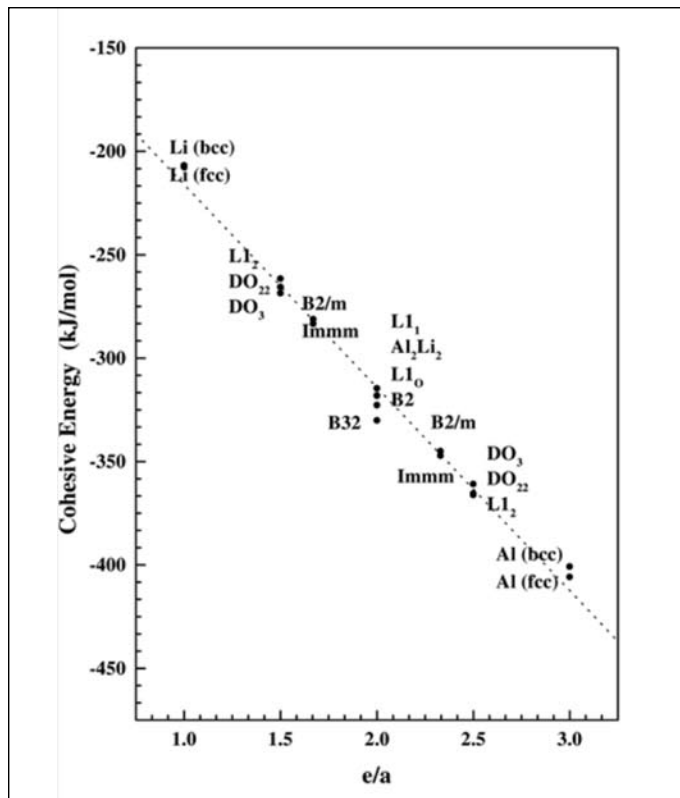


Figure 1: The cohesive energies of various fcc-based and bcc-based coherent ordered structures of Al-Li system plotted as a function of electrons/atom ratio. These cohesive energies have been calculated from first-principles local-density based Tight-binding linear muffin-tin orbital (TB-LMTO) method.

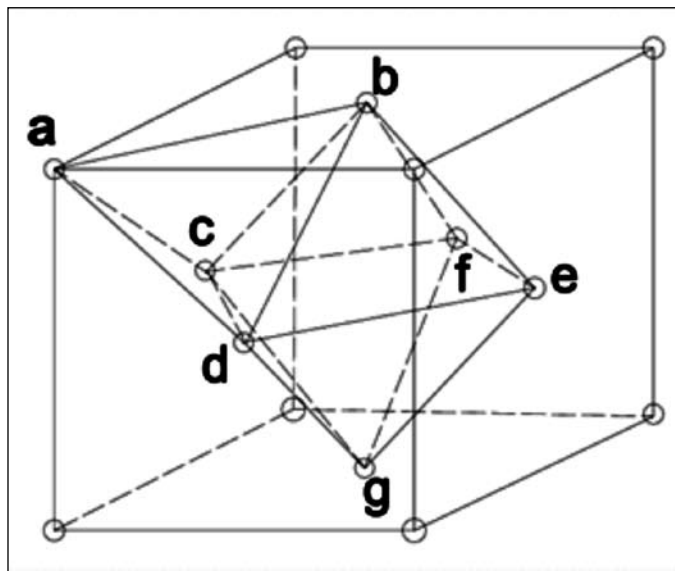


Figure 2: The octahedron (bcdefg)-tetrahedron (abcd) (OT) cluster approximation for the fcc lattice which has been used for the calculation of EPIs and free energy.

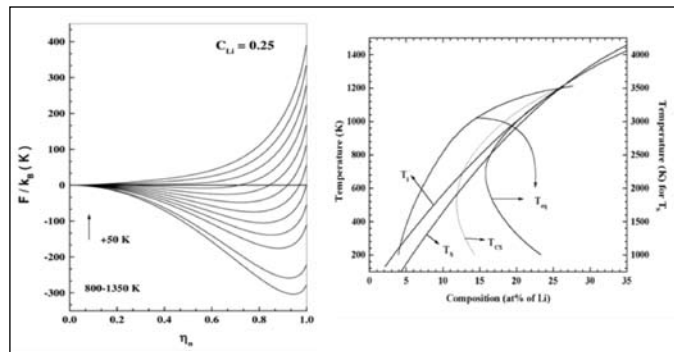


Figure 3: (a) The free energy (F) of ordering for the $L1_2$ structured Al_3Li phase plotted as a function of order parameter (η) at various temperatures. (b) The instability diagram showing different in stability domains (conditions) where a different phase reaction becomes operative for the precipitation of $L1_2$ phase.

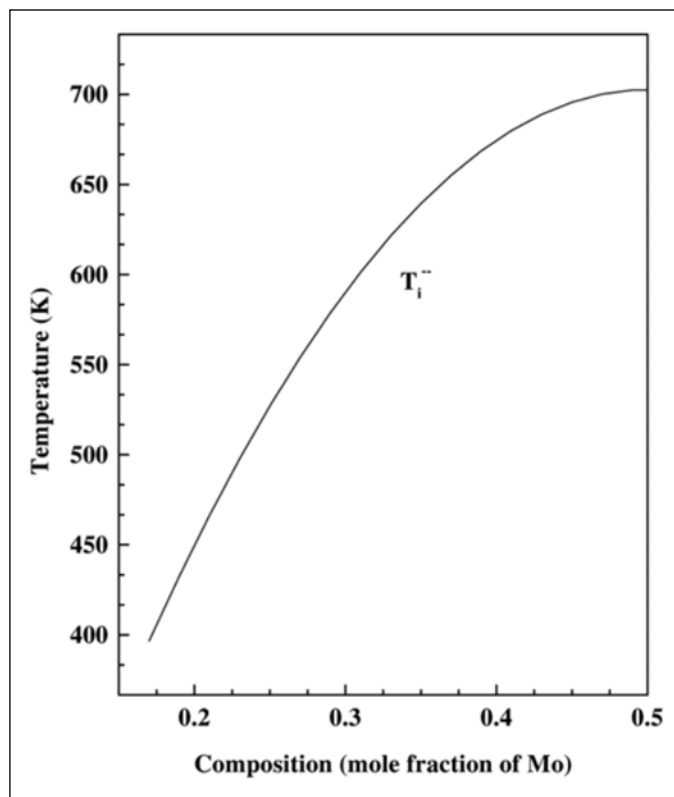


Figure 4: The ordering instability temperature (T_i) corresponding to onset of $(1\frac{1}{2}0)^*$ ordering instability in the Ni-Mo alloys plotted as a function of concentration of Mo.

theoretical investigation have been presented in the form of a phase diagram in which different instability lines have been marked (Fig. 3(b)) [2].

It is possible to construct common tangents between the free energy-composition curves corresponding to the α - and the δ' -phases and the compositions marked by the points where the common tangents touch the $F(c)$ curves indicate the metastable phase boundaries of the

two phases. The Landau plots generated from the present first-principles analysis show the conditions at which the disordered solid solution develops instability with respect to $L1_2$ ordering. The temperature corresponding to the onset of instability is defined as T_i^- has been obtained from $F(\eta)$ plots. We have also plotted, in Fig. 3(b), the *conditional spinodal* line (T_{cs}) below which spinodal clustering instability develops after ordering has occurred to a certain extent. The T_{cs} instability line has been determined from the free energy versus composition curves for the ordered δ' -phase at different temperatures.

2.2 Ni-Mo system

This alloy system is particularly interesting from the objective of studying ordering reactions in which several fcc-based superstructures compete with each other and involves both short range ordering (SRO) and long range ordering (LRO) processes. Further, one also observes, in this system, a competition between a first order and a second order phase transformation [9].

The Ni-Mo alloys exhibit three stable ordered intermetallic phases, *viz.*, Ni_4Mo - $D1a$ ($B2/m$), Ni_3Mo - $D0_a$ ($Pm\bar{m}n$) and $NiMo$ (δ') - ($I4/amd$) and two metastable ordered phases, *viz.*, Ni_3Mo - $D0_{22}$ ($I4/mmm$) and Ni_2Mo - Pt_2Mo type ($Immm$). The various cohesive properties and the zero-temperature stability sequence of a series of fcc-based ordered Ni_cMo_{1-c} compounds have been obtained using first-principles TB-LMTO electronic structure calculations [2, 10].

The configurationally-averaged concentration dependent EPIs upto the fourth nearest neighbor pairs have been obtained using the ASR+OP technique at 20, 25, 33 and 50 at% Mo-concentrations. The coherent LRO structures which are observed in the Ni-Mo alloy system belong to the $\langle 1\frac{1}{2}0 \rangle$ family and can be distinguished in terms of different stacking sequence of (420) planes that contain either all Ni or all Mo atoms. We have used SCW model in conjunction with ASR+OP method to model the free energies of all these superstructures as a function of T , c and η and studied the relative stabilities and ordering behavior of these competing ordered phases [10].

The concentration wave description of these superstructures is obtained by Fourier transforming the concentration delta function $N(\mathbf{p})$, which is equal to unity at plane $\mathbf{p} = 0, N, 2N$ etc. and zero elsewhere ($\mathbf{p} = 1, 2, \dots, N-1$), so that the concentration Fourier spectrum is given by

$$N(\mathbf{k}) = \frac{1}{N} \sum_{\mathbf{p}=0}^{N-1} N(\mathbf{p}) \cdot \exp[-2\pi\mathbf{k}\mathbf{p}] = \frac{1}{N}$$

For each structure, there are exactly $N(=2,3,4,5)$ Fourier waves of same amplitude. Our results on the ordering temperature as a function of composition are shown in Fig. 4. Since an alloy in this system experiences ordering tendencies corresponding to different \mathbf{k} -vectors, it is necessary to examine these in terms of Landau plots with respect to different \mathbf{k} -vectors. This point is illustrated for

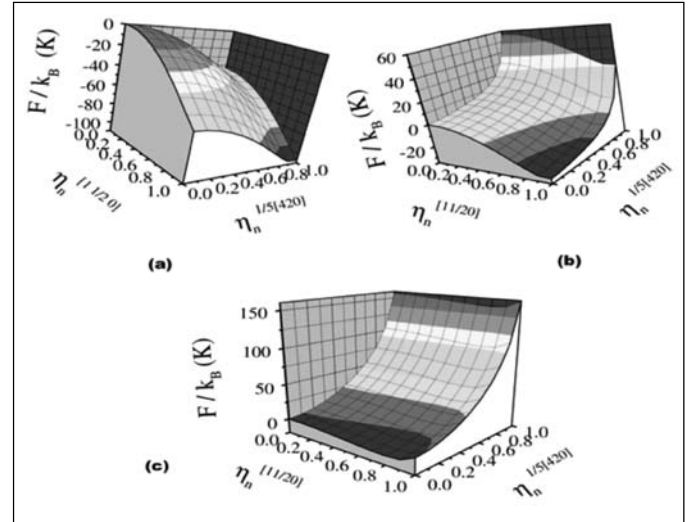


Figure 5: The ordering free energy of the Ni_4Mo -based alloys, exhibiting the $\langle 1\frac{1}{2}0 \rangle^*$ and the $\frac{1}{5}\langle 420 \rangle^*$ ordering tendencies, plotted as a function of order parameters for the corresponding ordering processes at (a) 200 K (b) 400 K and (c) 600 K.

the Ni_4Mo alloy in which the second order $\langle 1\frac{1}{2}0 \rangle^*$ ordering and the first order $\frac{1}{5}\langle 420 \rangle^*$ ordering compete. We have calculated the free energy of these alloys $\left(\eta_n^{[1\frac{1}{2}0]}, \eta_n^{[\frac{1}{5}420]}\right)$ at a given temperature as

$$F^{Ni_4Mo} \left(\eta_n^{[1\frac{1}{2}0]}, \eta_n^{[\frac{1}{5}420]} \right) = \frac{1}{2} \left[F^{N_4M} \left(\eta_n^{[\frac{1}{5}420]} \right) + F^{N_2M_2} \left(\eta_n^{[1\frac{1}{2}0]} \right) \right]_{at_{c_{Mo}} = 0.20}$$

Fig. 5 shows our results at temperatures 200K, 400K and 600K. Though $D1a$ is the stable equilibrium structure at $c_{Mo}=0.20$, a stronger tendency for the development of $\langle 1\frac{1}{2}0 \rangle^*$ ordering can be noticed in the initial stages of ordering as reflected by a larger negative curvature of the free energy surface at $\eta_n^{[1\frac{1}{2}0]} = \eta_n^{[\frac{1}{5}420]} = 0$ along the $\eta_n^{[1\frac{1}{2}0]}$ axis.

At $T=200K$, the curvature of the free energy surface is negative in both the directions which suggest that homogeneous ordering is possible for both the ordering processes. A mixed state consisting of concentration waves with wave vector ranging from $\langle 1\frac{1}{2}0 \rangle^*$ to $\frac{1}{5}\langle 420 \rangle^*$ is encountered on the path of the ordering process at these temperatures.

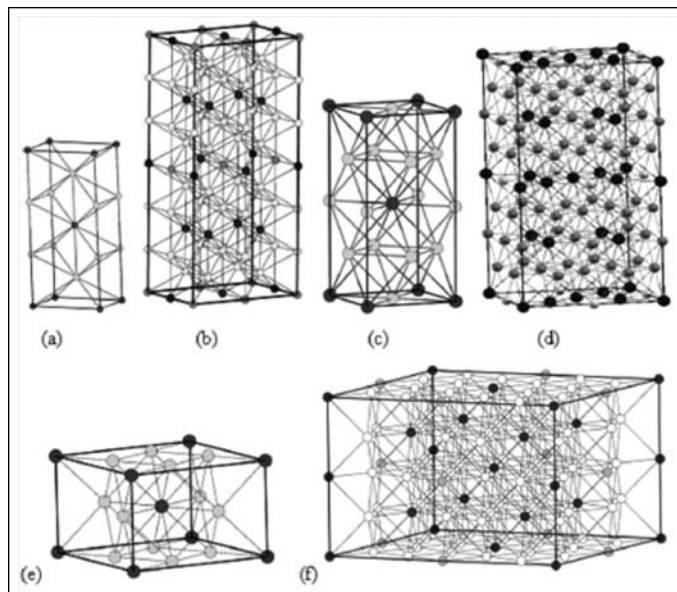


Figure 6: Unit cells of (a) Ni_2Mo ($I\text{mmm}$) and (b) its supercell ($\text{Ni}_{16}\text{Mo}_6\text{X}_2$); (c) Ni_3Mo ($I4/m\text{mm}$) and (d) its supercell ($\text{Ni}_{24}\text{Mo}_6\text{X}_2$); (e) Ni_4Mo ($I4/m$) and (f) its supercell ($\text{Ni}_{32}\text{Mo}_6\text{X}_2$). Ni: grey circles, Mo: dark circles, X: white circles.

2.3 Ni-Mo-X Systems

There has been a great deal of interest in studying the effect of ternary additions (*e.g.*, Cr, V, Ta, *etc.*) on the ordering behavior of Ni-Mo alloys [11]. A partial substitution of Mo by elements with $e/a < 6$, which reduces the overall e/a ratio to 8.75, stabilizes the Ni_3Mo (D_{022}) structure vis-a-vis the phase mixture of Ni_4Mo (D1a) and Ni_2Mo (Pt_2Mo -type) structures. A further decrease in the e/a ratio to 8.25 stabilizes the Ni_3Mo (L_1) structure. However, no explanation was given for this preference in a rigorous manner. On the other hand, the general tendency of the Ni_3Mo alloy and some of its ternary derivatives to decompose into a mixture of the Ni_2Mo and the Ni_4Mo phases, avoiding the D_{022} structure which satisfies the stoichiometry, has been rationalized in terms of nearly equal stabilities associated with the competing structures. An important point regarding the stability of ordered phases in Ni-Mo-X alloys (where X refers to a third element such as Al, Cr, Mn or V) is that the long range order (LRO) state of the binary alloy of Ni_3Mo composition comprises a phase mixture of Ni_4Mo (D1a) and Ni_2Mo (Pt_2Mo -type). The stoichiometric Ni_3Mo (D_{022}) phase appears only in alloys wherein Mo is partially substituted by Al, Cr or Mn.

The selection of the ternary element and its concentration are expected to have a strong influence on the relative phase stabilities of the competing superlattice structures. With this in mind, we have investigated the effect of four

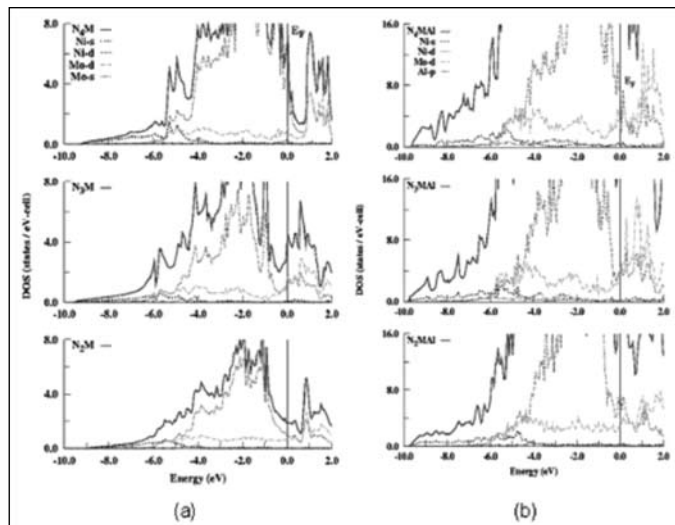


Figure 7: Total, site- and l -projected DOS for (a) binary Ni-Mo intermetallics, where only s - and d - states of both Ni and Mo atoms are shown and for (b) ternary Ni-Mo-Al, where partial densities of Ni- s , Ni- d , Mo- d and Al- p states are shown.

ternary additives, *viz.*, Al, Cr, Mn and V on the relative phase stability of D_{022} , D1a and Pt_2Mo -type intermetallics using a first-principles electronic structure method. For our calculations, we have taken three binary intermetallic structures, *viz.*, Pt_2Mo -type Ni_2Mo , D_{022} - Ni_3Mo and D1a- Ni_4Mo and their ternary analogues (Ni-Mo-X, X=Al, Cr, Mn and V), *viz.*, $\text{Ni}_{16}\text{Mo}_6\text{X}_2$, $\text{Ni}_{24}\text{Mo}_6\text{X}_2$ and $\text{Ni}_{32}\text{Mo}_6\text{X}_2$, respectively (see Fig. 6).

The energy of formation (E_{form}) of a given intermetallic is calculated by subtracting weighted sum of cohesive energies of constituent elements from the cohesive energy of the intermetallic. The question of whether it is D_{022} or it is the phase mixture of D1a and Pt_2Mo which is more stable can now be answered by comparing $E_{\text{form}}(\text{Ni}_3(\text{Mo},\text{X}))$ and sum of $E_{\text{form}}(\text{Ni}_4(\text{Mo},\text{X}))$ and $E_{\text{form}}(\text{Ni}_2(\text{Mo},\text{X}))$, where X = Al, Cr, Mn and V. For binary Ni-Mo, it is seen that $E_{\text{form}}(\text{Ni}_3\text{Mo})$ (-0.220 eV/atom) is greater than $E_{\text{form}}(\text{Ni}_4\text{Mo}) + E_{\text{form}}(\text{Ni}_2\text{Mo})$ (-0.238 eV/atom), indicating that a phase mixture D1a + Pt_2Mo will be more stable than the D_{022} phase. For all ternary intermetallics, one observes that $E_{\text{form}}(\text{Ni}_3(\text{Mo},\text{X})) < E_{\text{form}}(\text{Ni}_4(\text{Mo},\text{X})) + E_{\text{form}}(\text{Ni}_2(\text{Mo},\text{X}))$ indicating that ternary D_{022} phase is energetically favored as compared to phase mixture of D1a and Pt_2Mo structures in all the ternary analogues. The effect of ternary addition (Al, Cr, Mn, V) is, thus, seen to stabilize the D_{022} structure and the tendency of the third element for stabilizing D_{022} structure is observed to be strongest in the case of Al followed by V.

The addition of third element modifies the nature of bonding operative in the binary intermetallics as can be

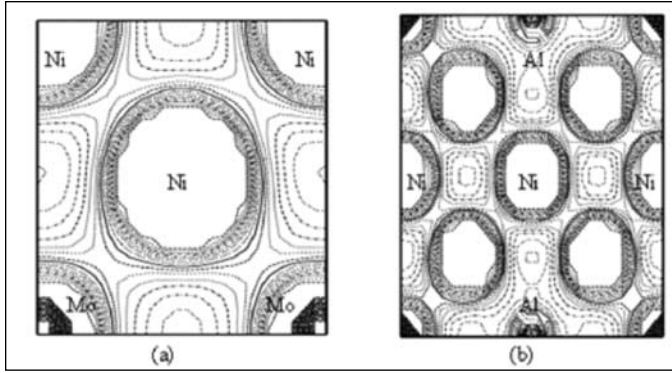


Figure 8: Valence charge density contour plots, ranging between 0.001e to 0.1e, on (100) plane in binary Ni_3Mo ($D0_{22}$) and (b) its ternary superstructure $Ni_{24}Mo_6Al_2$. The enhanced charge density along Ni-Al bond in (b) reflects covalent character of bonding on Al addition.

seen in Fig. 7, where we have plotted total and *site-* and *l-*projected density of states (DOS) for binary intermetallics and those of ternary analogues with only Al as the third element, for the sake of brevity. In binary compounds, the lower part of the valence band is dominated by Ni-s. The mixing of *d-d* states is responsible for metallic bonding in these binary intermetallics, as also evidenced by DOS at the Fermi level ($\rho(E_F)$). The higher the $\rho(E_F)$, the more metallic is the bonding. In the case of Ni-Mo-Al ternary intermetallics, the occupied part of DOS has broadened a little (by ≈ 0.7 eV) as compared to their binary analogues and the lower part of the valence band exhibit larger mixing of Ni-s and Al-p states in the $D0_{22}$ structure than that in $D1a$ structure imparting covalent character to the bonding. Similarly, the valence charge density contour plots on (100) plane of binary Ni_3Mo ($D0_{22}$) and its ternary superstructure $Ni_{24}Mo_6Al_2$ (Fig. 8) clearly distinguish the nature of bonding operative in these two systems. While in binary Ni_3Mo , there is metallic σ *d-d* interactions, the ternary analogue exhibit enhanced charge density along Ni-Al bond. Thus, it may be concluded that Al stabilizes the $D0_{22}$ structure by contributing to covalent bonding in the ordered phase.

3. Martensitic transformation in Pure Zr

An important example of martensitic transformation is the pressure induced α (hcp) \rightarrow ω (hexagonal) transformations in pure Zr and Zr rich alloys [12]. On the one hand, these materials has significant technological implications in aerospace, medical, and nuclear fields due to its high strength, light weight, and corrosion resistance. On the other hand, formation of ω phase reduces toughness and ductility properties of these materials. Thus, there exists a substantial interest both from an industrial, applied and an academic point of view to develop accurate and

effective methods to understand atomistic pathway for this martensitic phase transformation.

In all experimental observations, the $\alpha \rightarrow \omega$ transformation pathways are always inferred from the orientation relationships (OR) between the parent and daughter phases because of experimental difficulties involved in it. Such an approach may result in multiple transformation pathways for a given set of orientation relations, instead of indicating appropriate transformation pathway. In view of experimental work performed so far, there have been three suggestions for orientation relations (ORs) about the formation of omega structure (ω) from hcp structure (α) in pure Zr. The first OR predicted by Silcock[13], which is a direct transformation pathway without any intermediate state and also involving significant atomic shuffle and relatively small strain, is

$$(0001)_\alpha || (11\bar{2}0)_\omega \text{ and } [11\bar{2}0]_\alpha || [0001]_\omega$$

The second structural model was predicted by Usikov and Zilbershtein[14] in which the $\alpha \rightarrow \omega$ transformation proceeds via the β -phase. The OR's were derived by a lattice correspondence matrix which was the product of known $\alpha \rightarrow \beta$ and $\beta \rightarrow \omega$ transformation matrices. Two omega variants were predicted by this procedure,

$$\text{Variant 1: } (0001)_\alpha || (11\bar{1}1)_\omega ; [10\bar{1}0]_\alpha || [10\bar{1}1]_\omega$$

$$\text{Variant 2: } (0001)_\alpha || (11\bar{2}0)_\omega ; [11\bar{2}0]_\alpha || [0001]_\omega$$

It is worth noting that the Variant 2 is the same as that predicted by Silcock's model. Afterwards Rabinkin *et al.*[15] gave another diffusionless displacive model for $\alpha \rightarrow \omega$ transformation and concluded that only three

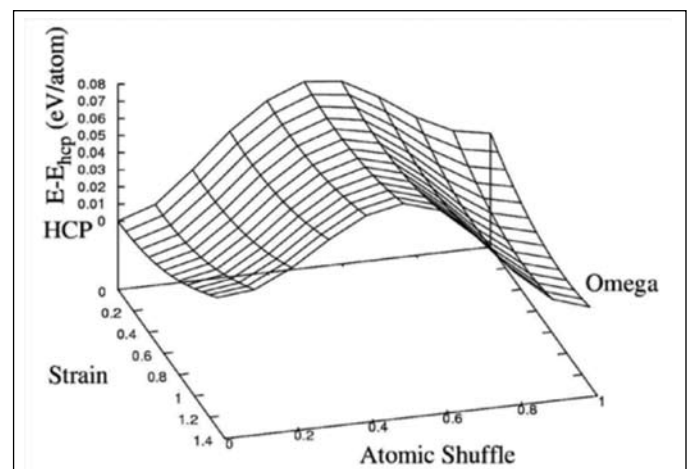


Figure 9: The calculated $\alpha \rightarrow \omega$ transformation landscape for pure Zr at ambient condition where points (0,0,0) and (1,1,0.005) correspond to hcp and omega phases, respectively.

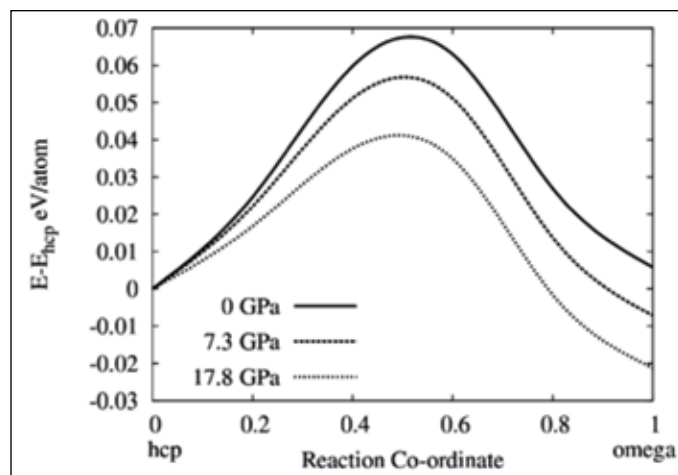


Figure 10: Enthalpy barrier as a function of pressure for the $\alpha \rightarrow \omega$ transformation pathway as described by Silcock.

crystallographically equivalent variants corresponding to Variant 2 were possible. In this investigation, the $\alpha \rightarrow \omega$ transformation energy landscape as well as the enthalpy barrier as a function of pressure for pure Zr is calculated within the DFT using the nudged elastic band (NEB) method. The NEB method generates a discretized pathway connecting the initial and final states (by generation of chain of images), and relaxes it to pass through the transition state to guarantee that the final pathway lies along the minimum energy pathway and produces the true energy barrier.

Using the calculated equilibrium structural parameters for α phase, a 12 atom orthorhombic $a \times c \times 3\sqrt{3}$ supercell with atoms occupying 3 different $4(d)$ Wyckoff positions was made. Starting from that cell, a ω structure was made by shuffle of 3 atoms (occupying $(0001)_\alpha$ plane) by 0.814 \AA along $[11\bar{2}0]_\alpha$, while the other 3 shuffle in opposite direction $[\bar{1}\bar{1}20]_\alpha$. This shuffle is accompanied by a strain $e_{xx} = 0.05$ along $[1\bar{1}00]_\alpha$ and $e_{yy} = -0.05$ along $[11\bar{2}0]_\alpha$ to produce a hexagonal ω cell with the correct c/a ratio. The calculated $\alpha \rightarrow \omega$ transformation landscape is shown in Fig. 9.

Fig. 10 shows the variation of enthalpy along the $\alpha \rightarrow \omega$ transformation path for the Silcock pathway as a function of pressure. Our calculation shows that the α phase is slightly lower in energy than the ω at 0 GPa. As pressure increases, the enthalpy of ω phase drops relative to the α phase and the pathway decreases its enthalpy barrier. The ab-initio calculated NEB barriers at 0K for this pathway is 68 meV/atom [16].

4. Epilogue

It is to be noted that a major shortcoming of many of the ab initio phase diagram calculations concerns the

inadequate treatment of local volume and elastic relaxations and the neglect of vibrational modes. Even in crystalline solids atoms are in perpetual motion; they move from lattice site to lattice site by diffusion at nonzero temperatures and also vibrate about their equilibrium positions. In a multicomponent system like an alloy, a given lattice site is occupied by atoms of different species at different times. If a large atom replaces a small one, the environment of the lattice site responds by expanding. Likewise, when a small atom replaces a large atom, the neighboring atoms relax towards the lattice site in question. It should be possible to address the accompanying strain fluctuations within the same type of first-principles framework that is pertinent to fluctuations in concentration. However, the treatment of local relaxations of this kind presents a very difficult problem and not many attempts appear to have been made to include this effect in first principles calculations of phase stability and phase diagrams.

Acknowledgment

The author wishes to thank his collaborators S. Banerjee, G.K. Dey, G.P. Das and P.S. Ghosh for their support.

References

1. D. de Fontaine in *Solid State Physics*, (eds.) H. Ehrenreich, F. Seitz and D. Turnbull (Academic Press, New York, 1994), Vol. 47 p.33.
2. A. Arya, S. Banerjee and G.P. Das, in *Frontiers in Materials Modelling and Design*, Eds. Vijay Kumar, S. Sengupta and B. Raj (Springer Verlag, Heidelberg, 1997).
3. W. Connolly and A.R. Williams, *Phys. Rev.*, **B27**, 5169 (1983); and in *The electronic structure of complex systems*, (eds.) W. Temmerman and P. Phariseau, (Plenum Press, New York, 1984) p.581.
4. A. Mookerjee in *Methods of Electronic structure calculations*, O.K. Andersen, V. Kumar and A. Mookerjee (eds.), [Proceedings of the Mini-workshop held in ICTP, Trieste, August 1992] (World Scientific, 1993).
5. A.G. Khachatryan in *Theory Of Structural Transformations In Solids*, Willey, New York (1983).
6. G. Inden and W. Pitsch W. in *Phase Transformation in Materials*, (ed.) P. Haasen, (VCH Press, New York, 1991).
7. W.A. Soffa and D.E. Laughlin in *Physical Properties and Thermodynamic Behaviour of Minerals*, NATO ASI series C, **Vol. 225**, 213 (1988).
8. W.A. Soffa and D.E. Laughlin, *Acta Metall.*, **37**, 3019 (1989).
9. S. Banerjee, U.D. Kulkarni and K. Urban, *Acta Metall.*, **37(1)**, 35 (1989).
10. A. Arya, S. Banerjee and G.P. Das, I. Dasgupta, T. Saha-Dashupta and A. Mookerjee, *Acta Mater.*, **49**, 3575 (2001).
11. A. Arya, G.K. Dey and S. Banerjee, *Acta Mater.*, **50**, 3301 (2002).

12. S.K. Sikka, Y.K. Vohra and R. Chidambaram, *Prog. Mater. Sci.*, **27**, 245 (1982).
13. Z. J.M. Silcock, *Acta Metall.*, **6**, 481 (1958).
14. M.P. Usikov and V.A. Zilbershtein, *Phys. Stat. Solidi (a)*, **19**, 53 (1973).
15. A. Robinkin, M. Talianker and O. Botsteirg, *Acta Metall.*, **29**, 691 (1981).
16. P. S. Ghosh, A. Arya and G.K. Dey, "Solid State Physics: Proceedings of the 57th DAE Solid State Physics Symposium 2012", AIP Conf. Proc., **1512**, 48-49 (2013).



Dr. Arya joined Materials Science Division, BARC in 1987 and obtained his PhD degree from Indian Institute of Technology, Bombay in the year 1997, which was followed by his post-doctoral stint at University of California at Los Angeles. He has been working in the area of computational materials science. His research interests include alloy phase stability, phase transformations, defects in solids and solid surfaces and interfaces.

Genome to Drug Software Initiatives

Shashank Shekhar¹, B. Jayaram^{1,2,3*}

¹Supercomputing Facility for Bioinformatics & Computational Biology, ²Department of Chemistry, ³Kusuma School of Biological Sciences, Indian Institute of Technology, Hauz Khas, New Delhi-110016, India
Email: bjayaram@chemistry.iitd.res.in; Website: www.scfbio-iitd.res.in

Abstract

Recent advances in human genome sequencing grant us the opportunity to sketch a computational pathway from Genome → Gene → Protein → Drug to develop personalized medicine almost in an automated way. Currently however, without the help of any database, neither a gene can be predicted nor the structure of its protein product. Also existing drug design softwares fall severely short of expectations. Addressing these issues, we at SCFBio, IIT Delhi have come up with a scientific solution, the “Gene to Drug” pathway. With a vision to developing personalized medicine using *Gene to Drug* pathway in an automated mode, particularly to cut the cost, time and effort involved in drug discovery and also to decipher the molecular level principles in the process, we undertook a massive endeavor of creating new science and novel software using physico-chemical approaches configured in a high performance computing (HPC) environment. Our efforts have resulted in a whole genome analysis methodology and software based on DNA energetics (*ChemGenome*: <http://www.scfbio-iitd.res.in/bioinformatics/genefinding.htm>), an all atom energy based computational protocol for protein tertiary structure prediction (*Bhageerath* and *Bhageerath-H*: <http://www.scfbio-iitd.res.in/bhageerath/index.jsp> and http://www.scfbio-iitd.res.in/bhageerath/bhageerath_h.jsp) and a binding free energy based methodology for protein/DNA targeted lead molecule design (*Sanjeevini*: <http://www.scfbio-iitd.res.in/sanjeevini/sanjeevini.jsp>). These softwares are web-enabled and made freely accessible from the SCFBio site to the entire global community of interested scientists and students. With the help of these softwares one can design a lead molecule which could be improved iteratively in combination with experiment. The *Gene to Drug* pathway is a major step towards finding the right medicine for the right disease for the right person in an automated way with a potential to help the society in a big way.

Introduction

The growing databases of genomic sequences of pathogens and humans afford us an opportunity to dream that *in silico* suggestions of candidate drugs with high levels of affinity, specificity to the biomolecular target and low toxicity to humans will be forthcoming almost in an automated assembly line within hours in the foreseeable future. The challenges to overcome to facilitate this include, (i) higher levels of accuracies in genome annotation, (ii) evolution of algorithms for automated identification of druggable targets in the genome or proteome, (iii) generation of accurate tertiary/quaternary structures of protein targets and, (iv) design of small molecules with high levels of affinity and selectivity to the target with proper ADMET (Absorption, Distribution, Metabolism, Excretion & Toxicity) profiles. We describe, in this article the progress achieved in each of the above areas and the conceivability of a “Genome to hit” assembly line *in silico* (Fig. 1).

Background

The science and the software behind “Genome to Hits” assembly line which comprises six steps (Fig. 2),

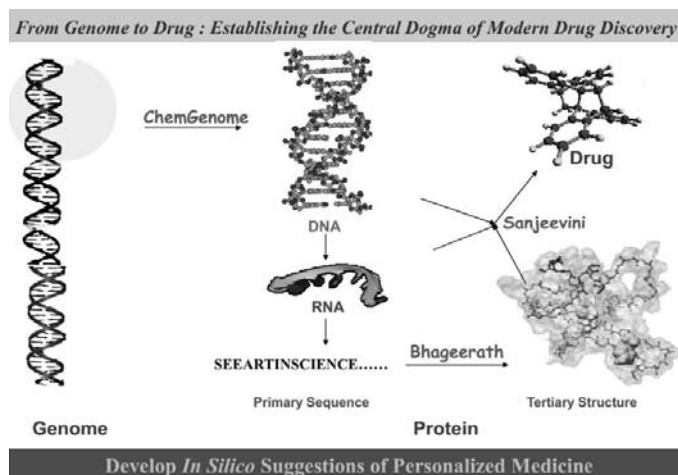


Figure 1. Genome to drug: an assembly line in the making at www.scfbio-iitd.res.in.

is classifiable into three major areas of research viz. (a) genome annotation, (b) protein tertiary structure prediction and (c) structure based drug design.

I. Genome Annotation. An organism’s genome is an information resource, which can be best understood if properly annotated. The annotation bridges the gap

Input the HBV Genome sequence to ChemGenome

Hepatitis B virus, complete genome
NCBI Reference Sequence: NC_003977.1
>gi|21326584|ref|NC_003977.1| Hepatitis B virus, complete genome

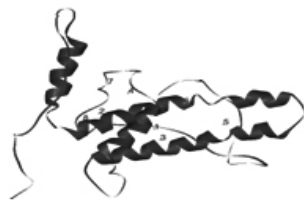
ChemGenome 3.0 output

Five protein coding regions identified

Gene 2 (BP: 1814 to 2452) predicted by the ChemGenome 3.0 software encodes for the HBV precore/core protein(Gene Id: 944568)



>gi|77680741|ref|YP_355335.1| precore/core protein [Hepatitis B virus]
MQLFPLCLIISCSCPTVQASKLCLGWLWGMIDIDPYKEFGASVELLSFLPSDFFPSIRDLLDTASALY
REALESPHCHSPHHTALRQAILCWGELMNLATWVGSNLEDPASRELVVSYNVNMGLKIRQLLW
FHISCLTFGRETVLEYLVSFGVWIRTPPAYRPPNAPILSTLPETTIVRRRGRSPRRRTPSRRRRSQS
PRRRRSQSRESQC



Input Protein Structure to Active site identifier (ASF/Sanjeevini)

10 potential binding sites identified

Scan a million compound library

RASPD/Sanjeevini calculation with an average cut off binding affinity to limit the number of candidates. (Empirical scoring function which builds in Lipinski's rules and Wiener index)

RASPD output

2057 molecules were selected with good binding energy from one million molecule database corresponding to the top 5 predicted binding sites.



Out of the 2057 molecules, top 40 molecules are given as input to ParDOCK/Sanjeevini for atomic level binding energy calculations. Out of this 40, (with a cut off of -7.5 kcal/mol), 24 molecules are seen to bind well to precore/core protein target. These molecules could be tested in the Laboratory.



Mol. ID	Binding Energy (kcal/mol)
0001398	-10.14
0004693	-8.78
0007684	-10.05
0007795	-9.06
0008386	-8.38
0520933	-8.21
0587461	-10.22
0027252	-8.39
0036686	-8.33
0051126	-8.73
0104311	-9.3
0258280	-7.8
0000645	-7.89
0001322	-8.23
0001895	-9.49
0002386	-8.53
0003092	-8.35
0001084	-8.68
0002131	-8.07
0540853	-11.08
1043386	-10.14
0088278	-9.16
0043629	-7.5
0097895	-8.04

24 hit molecules for precore/core protein target of HBV which can be iteratively procured/synthesized, tested and further optimized in silico for obtaining lead molecules

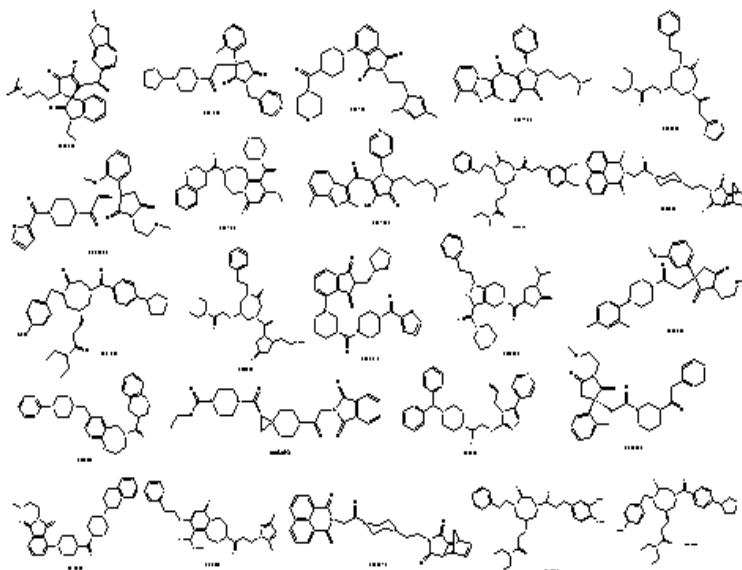


Figure 2. Flow diagram illustrating the steps involved in Dhanvantari pathway to achieve hit molecules from genomic information.


between the genomic sequence and the biology of the organism [1]. The announcement of the human genome [2] changed the outlook of current biomedical research. Advances in technologies have made possible sequencing of the genomes of various organisms reliably and rapidly and this should be a routine matter soon. The flow of information from the sequencing projects has now shifted the focus to high quality genome annotation/analysis. The first step towards annotating a genome is to separate the genes coding for proteins from non-genes. Although there is no substitute for molecular biology for determining the exact locations of genes and regulatory sequences in a genome, diverse computational methods have been shown

to have reasonably successful predictive power [3, 4]. Most of the available computational methods are knowledge based and use techniques like hidden Markov models or machine learning methods. The accuracies of these models are limited by the availability of samples of experimentally validated genes, and as typically seen in a newly sequenced genome can lead to suboptimal levels of prediction. An alternative to the knowledge based methods for gene prediction is an *ab initio* model. ChemGenome (Fig. 3) www.scfbio-iitd.res.in/chemgenome/chemgenomenew.jsp is an *ab initio* method for gene prediction in prokaryotes. It examines physicochemical properties and geometrical structures of codons [3-7] to ask the fundamental question,

CHEMGENOME 2.0

An ab-initio Gene Prediction Software

Chemgenome is an *ab-initio* gene prediction software, which find genes in prokaryotic genomes in all six reading frames. The methodology follows a physico-chemical approach and has been validated on 372 prokaryotic genomes. [Read more about ChemGenome](#)

Download CHEMGENOME 2.0 for Linux environment from here 

[\[General Info\]](#) [\[Data Set\]](#) [\[Validated Result Set\]](#) [\[Help\]](#) [\[Home\]](#)

Input File No file chosen

OR paste Genome Sequence in FASTA format

Additional Parameters

Threshold Values : Start Codon : ATG CTG GTG TTG

Method : DNA Protein Swissprot

E-mail ID : (Optional)

Figure 3. A front-end of the freely accessible ChemGenome 2.0 software (www.scfbio-iitd.res.in/chemgenome/chemgenomenew.jsp)

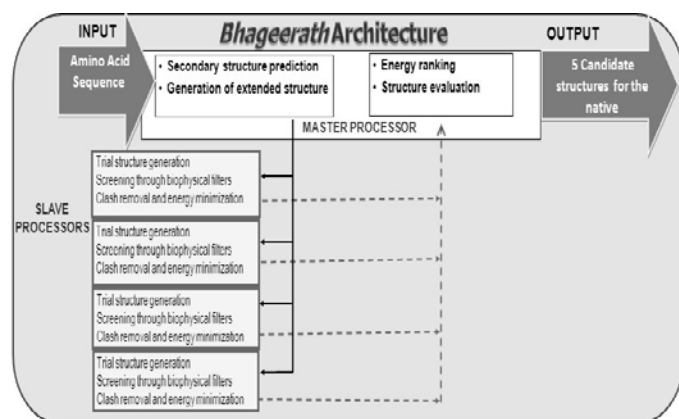


Figure 4. Bhageerath Methodology

“What is a gene?” and extracts an answer from the structural and thermodynamic properties of DNA sequences, more specifically, the hydrogen bond, the stacking and the solvation energies computed from molecular dynamics generated structures. The methodology has been validated on 372 prokaryotic genomes and the sensitivity, specificity and correlation coefficients averaged over 356208 genes and an equal number of frame-shifted genes (non-genes) are 97.5%, 97.20% & 94.25%, respectively. A promoter prediction methodology developed on the same lines is being integrated with ChemGenome to further reduce false positives. The physico-chemical model for gene evaluation and gene prediction for prokaryotic genomes has been web-enabled and is freely accessible at the SCFBio website (Fig. 3).

II. Protein tertiary structure prediction: Protein annotation is the next crucial step in the pipeline after the genome annotation. Human genome is ~3300Mb with ~20,500 protein coding genes and ~3000 non-protein coding RNA genes [8, 9] which is about 2% of the genome. Of these proteins, only a small fraction has an experimentally determined 3D structures and well characterized functional annotation. There are over half a million sequence entries in UniProtKB/Swiss-Prot databases but X-ray and NMR structures are available for only ~92,000 sequence entries in the RCSB (Protein Data Bank).

The increasing gap between sequences and structures makes it simply impossible to solve the structures of all existing proteins experimentally. The knowledge of the 3D structure of a protein can usher in tools for structure based drug discovery. Thus, a reliable computational method for protein tertiary structure prediction is desperately needed. Various computational methodologies have been developed for the prediction of tertiary structures of proteins over the past few years. These include (a) comparative modeling, (b) fold recognition or threading, (c) *ab initio* or *de novo* methods. Comparative modeling and fold recognition methods are database driven and their prediction accuracies depend on the sequence similarities realized in known structures. These methods are extremely popular, reliable and fast for protein tertiary structure prediction when a close sequence homolog exists in the database. *Ab initio* or *de*

novoo methods are used for predicting structure of protein sequences with no close structural homologs. We

Figure 5. Front-end of Bhageerath-H software for protein tertiary structure prediction

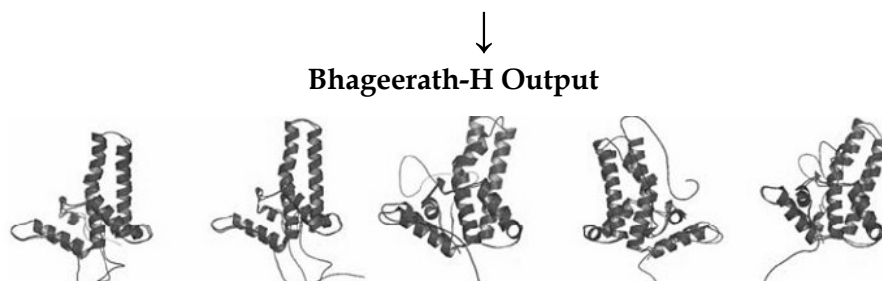


Figure 6. Top five energy ranked structures. The structure shown in red color is the native and that in blue is the predicted structure.

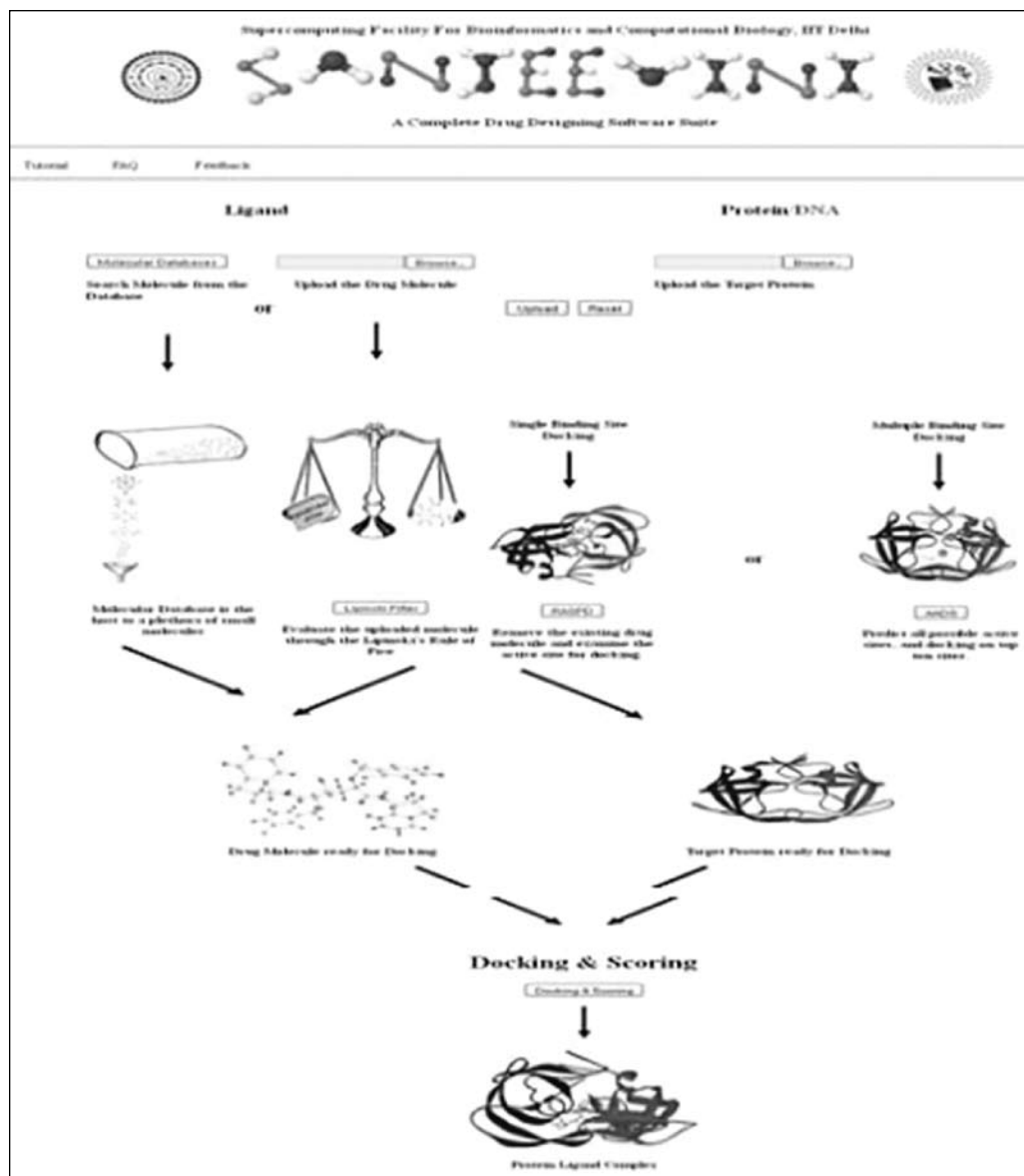


Figure 7. Front-end of SANJEEVINI, an automated drug design software freely accessible at <http://www.scfbio-iitd.res.in/sanjeevini/sanjeevini.jsp>.

have developed two different computational protocols for predicting tertiary structures of soluble proteins. Bhageerath [10] (Fig. 4) is an energy based software suite for predicting tertiary structures of small globular proteins. The protocol comprises eight different modules which use physicochemical properties of proteins and *ab initio* methodology to predict five candidates for the native from the input query sequence. The [10-13] methodology has been validated on 80 small globular proteins with < 100 amino acids. For each of these proteins a structure within 3-7Å RMSD (root mean square deviation) from the native is predicted within few minutes to hours on a 280 processor cluster (~3 Teraflops of computing capacity). Bhageerath-H (Fig. 5) [14-20] is a homology *ab initio* hybrid server for

protein tertiary structure prediction. The protocol identifies regions having local sequence similarity with database to generate 3D fragments which are patched with *ab initio* modeled fragments to put together complete structure of proteins. For sequences with available sequence homologs, Bhageerath-H software predicts a structure within 5 Å RMSD from the native (Fig. 6). Work is in progress to further improve the prediction accuracies of these softwares.

The performance of Bhageerath-H in CASP10 (10th Community Wide Experiment on Critical Assessment of Techniques for Protein Structure Prediction) has significantly improved since CASP9. Post CASP10 (July, 2012 onwards), several innovations incorporated into the methodology - albeit compute intensive - are yielding > 65% accuracies, which makes Bhageerath-H, one of the best servers for protein tertiary structure prediction. The knowledge of tertiary structures of

proteins serves as a basis for structure-based drug design.

III. Structure based drug design: The ability of biomolecules to bind to their substrates in a highly specific manner is an important characteristic in many biological processes. One of the major challenges for the CADD (Computer Aided Drug Design) techniques is to achieve this specificity i.e. specific binding of a small molecule to the biomolecular target *in vivo* at minimum cost and time, while maintaining novelty of the scaffolds and proper ADMET profiles. The two main steps in computer based drug design protocols are target identification and lead optimization. The knowledge of the structure of a biomolecule, such as a protein / nucleic acid assists in

Table1. List of some popular software developed at SCFBio

Sl. No.	Name of Software	Link	Remarks
1.	Melting temperature	http://www.scfbio-iitd.res.in/chemgenome/Tm_predictor.jsp	<i>It predicts the melting temperature of short and long DNA sequences</i>
2.	ProSEE	http://www.scfbio-iitd.res.in/software/utility/teomics/Prosee.jsp	<i>Scoring Function for Protein Structure Evaluation Calculates intramolecular energy of a protein</i>
3.	BAPPL	http://www.scfbio-iitd.res.in/software/drugdesign/bappl.jsp	Computes the binding free energy of a protein-ligand complex
4.	BAPPL-Z	http://www.scfbio-iitd.res.in/software/drugdesign/bapplz.jsp	Computes the binding free energy of a metalloprotein-ligand complex containing zinc.
5.	PREDDICTA	http://www.scfbio-iitd.res.in/software/drugdesign/preddicta.jsp	Calculates the Drug-DNA interaction energy.
6.	PARDOCK	http://www.scfbio-iitd.res.in/dock/pardock.jsp	Predicts the binding mode of the ligand in the target site.
7.	Active Site Prediction	http://www.scfbio-iitd.res.in/dock/ActiveSite_new.jsp	Predicts 10 binding sites in a protein target and docks the uploaded ligand molecule at all 10 sites predicted in an automated mode.
8.	Modified Wiener Index	http://www.scfbio-iitd.res.in/software/drugdesign/raspd2.jsp	Preliminary screening of ligand molecules based on physico-chemical properties of the ligand and the active site of the protein
9.	TPACM4	http://www.scfbio-iitd.res.in/software/drugdesign/charge.jsp	Assigns partial atomic charges to small molecules.
10.	DNADOCK	http://www.scfbio-iitd.res.in/dock/dnadock.jsp	Rigid Docking predicts the binding mode of the ligand in the minor groove of DNA
11.	BAITOC	http://www.scfbio-iitd.res.in/software/drugdesign/baitocnew.jsp	<i>Screens thousands of protein structures against the input organic molecules in a time efficient manner and provides information on proteins</i>

understanding the molecular level mechanism of action of drugs and lead optimization. Currently there are about 218 unique targets available for ~6000 FDA (U.S. Food and Drug Administration) approved drugs. A significant number of these targets are proteins and of the 218 targets, 3D structures are available for only 130.

Structure of the protein target molecule can be determined either experimentally or computationally (as discussed above). The next step after target identification and structure determination is the detection of the ligand binding site. Most of the experimentally determined structures have some information on ligand binding site. In the absence of such information, detection of ligand binding site is required. We have developed in-house a fully automated active site finder program for proteins (http://www.scfbio-iitd.res.in/dock/ActiveSite_new.jsp). The active site finder, taking 3D structure of the protein target as input, detects 10 potential binding sites with 100% accuracy in capturing the actual binding (active) site [21]. The next step in CADD protocol is lead

generation and optimization. A candidate molecule can either be sketched using publicly available drawing tools or searched from the small molecule libraries such as NRDBSM [22] which embeds Lipinski's rules [23] or the one developed by us more recently consisting of one million small molecules (<http://www.scfbio-iitd.res.in/software/nrdbsm/moleculerearchnew.jsp>). For a given biomolecular target, these databases of small molecules can be scanned for identifying hit molecules based on their physico-chemical parameters and functional groups. Assessment of the candidate molecules is performed by calculating the binding energies with the target, one of the major bottlenecks being the computational time. The calculation of binding energy of a small ligand with a protein target using docking and scoring methods can take minutes, which approximates to around 12000 to 15000 hours for a dataset of one million molecules. We have developed an in-house methodology christened RASPD (A rapid identification of hit molecules for target proteins via physico-chemical descriptors: <http://www.scfbio-iitd.res.in/software/drugdesign/raspd.jsp>), for calculation of

binding energy of target protein in significantly reduced amount of time [24]

The protocol screens the million compound library to suggest $\sim 10^2$ to 10^3 molecules within a minute. With the reduced dataset of hit molecules generated using RASPD, one can perform atomic level docking and scoring against the target. We have developed in-house a docking protocol "ParDOCK", an all-atom energy based Monte Carlo algorithm for protein-ligand docking (<http://www.scfbio-iitd.res.in/dock/pardock.jsp>) [25]. ParDOCK uses BAPPL [26] for atomic level scoring of non-metallo protein ligand complexes (<http://www.scfbio-iitd.res.in/software/drugdesign/bappl.jsp>). The accuracy of this scoring function to predict binding free energy is high with ± 1.0 kcal/mol average error and a correlation coefficient of 0.92 between the predicted and experimental binding energies for 161 protein-ligand complexes. For metallo-protein-ligand complexes with zinc metal ions, binding free energy can be calculated using BAPPL-Z (<http://www.scfbio-iitd.res.in/software/drugdesign/bapplz.jsp>) [27] which shows a correlation coefficient of 0.88 for the predicted binding free energy against the experiment on a dataset of 90 zinc containing metalloprotein-ligand complexes. Similarly, Preddicta [28, 29] methodology is used for docking and scoring candidate molecules to DNA. All of the above mentioned modules work in conduit and can be freely accessed from the drug design software christened "SANJEEVINI (Fig. 7) [30-33]. A list of some additional popular softwares developed in-house is provided in Table 1.

Conclusions

The Genome to Drug pathway [34] described here is akin to a country path today which is expected to become a high-way tomorrow. Improvements are warranted in all the three areas. Computational analyses of genomic information must lead to insights into sequence to function signals in DNA. The protein structure prediction, a grand challenge problem, has to attain higher levels of accuracies for lead molecule design. The computational drug design protocols have to deal with the issue of side-effects. Over all, the future of Genome to Drug endeavor looks promising.

References

- Stein, L. Genome annotation: from sequence to biology, *Nature Reviews genetics*, 2001, 2,493-503.
- International Human Genome Sequencing Consortium. Finishing the euchromatic sequence of the human genome, *Nature*, 2004, 431, 931-945.
- Dutta, S., Singhal, P, Agrawal, P, Tomer, R, Kritee, Khurana, E, Jayaram, B. A physicochemical model for analyzing DNA sequences, *J. Chem. Inf. Model.* 2006, 46, 78-85.
- Singhal, P, Jayaram, B., Dixit, S. B., Beveridge, D. L. prokaryotic gene finding based on physicochemical characteristics of codons calculated from Molecular dynamics simulations, *Biophysical J.* 2008, 94, 4173-4183.
- Khandelwal, G, Gupta, J, Jayaram, B. DNA energetics based analyses suggest additional genes in prokaryotes. *J Bio Sc.*, 2012, 37, 433-44.
- Khandelwal G, Jayaram B. A phenomenological model for predicting melting temperatures of DNA sequences. *PLoS ONE*, 2010; 5, e12433.
- Khandelwal, G, Jayaram, B. DNA-water interactions distinguish messenger RNA genes from transfer RNA genes. *J. Am. Chem. Soc.*, 2012, 134, 8814-16.
- Clamp, M, Fry, B, Kamal, M, Xie, X, Cuff, J, Lin, M. F., Kellis, M, Lindblad-Toh, K., Lander, E. S. Distinguishing protein-coding and noncoding genes in the human genome, *PNAS*, 2007, 104, 19428-19433.
- Wright, M. W., Bruford, E. A. Naming 'junk': Human non-protein coding RNA (ncRNA) gene nomenclature, *Human Genomics*, 2011, 5, 90-98.
- Jayaram, B., Bhushan, K. et al., Bhageerath: An energy based web enabled computer software suite for limiting the search space of tertiary structures of small globular proteins, *Nucl. AcidRes.*, 2006, 34, 6195-6204.
- Jayaram B, Dhingra P, Lakhani B, Shekhar S. Bhageerath-targeting the near impossible: pushing the frontiers of atomic models for protein tertiary structure prediction. *J Chem Sci.* 2012, 124, 83-91. doi:10.1007/s12039-011-0189
- Narang P, Bhushan K, Bose S, Jayaram B. A computational pathway for bracketing native-like structures for small alpha helical globular proteins. *Phys Chem Chem Phys.* 2005, 7, 2364-75.
- Narang P, Bhushan K, Bose S, Jayaram B. Protein structure evaluation using an all-atom energy based empirical scoring function. *J Biomol Struct Dyn.* 2006, 23, 385-406.
- Dhingra, P. Jayaram, B. A homology/ab initio hybrid algorithm for sampling near-native protein conformations, *J Comput.Chem.*, 2013, DOI: 10.1002/jcc.23339.
- Mishra, A., Rao, S., Mittal, A., Jayaram, B. Capturing Native/ Native like Structures with a Physico-Chemical Metric (pcSM) in Protein Folding, *BBA - Proteins and Proteomics*, 2013, DOI:10.1016/j.bbapap.2013.04.023.
- Mittal A, Jayaram B, Shenoy S, Bawa TS. A Stoichiometry driven universal spatial organization of backbones of folded proteins: Are there Chargaff's rules for protein folding?. *J Biomol Struct Dyn.*, 2010, 28, 133-42.
- Mittal A, Jayaram B. Backbones of folded proteins reveal novel invariant amino-acid neighborhoods. *J Biomol Struct Dyn.*, 2011, 28, 443-54.
- Mittal A, Jayaram B. The Newest View on Protein Folding: Stoichiometric and Spatial Unity in Structural and Functional Diversity. *J Biomol Struct Dyn.*, 2011, 28, 669-74.
- Shenoy SR, Jayaram B. Proteins: Sequence to Structure and Function-Current Status. *Curr Protein Pept Sci.* 2010, 11, 498-514.
- Jayaram B, Dhingra P. Towards creating complete proteomic structural databases of whole organisms. *Curr Bioinform.*, 2012, 7, 424-35.

21. Singh T, Biswas D, Jayaram B. AADS-an automated active site identification, docking and scoring protocol for protein targets based on physico-chemical descriptors. *J Chem Inf Model.*, 2011, 51, 2515-27.
22. Shaikh, SA, Jain, T., Sandhu, G., Latha, N., Jayaram, B. From drug target to leads- sketching, A physicochemical pathway for lead molecule design in silico, *Curr. Pharma. Des.*, 2007, 13, 3454-3470.
23. Lipinski C A. Lead- and drug-like compounds: the rule-of-five revolution, *Drug Discov. Today: Tech* 2004, 1, 337-341.
24. Mukherjee G, Jayaram B. A rapid scoring methodology based on physico-chemical descriptors of small molecules (RASPD) for identifying hits against a protein target. *Phys Chem Chem Phys.*, 2013, DOI:10.1039/C3CP44697B.
25. Gupta, A. Gandhimathi, A. Sharma, P., Jayaram, B. ParDOCK: An all atom energy based monte carlo docking protocol for protein-ligand complexes, *Protein and Peptide Letters*, 2007, 14, 632-646.
26. Jain, T., Jayaram, B. An all atom energy based computational protocol for predicting binding affinities of protein-ligand complexes, *FEBS Letters*, 2005, 579, 6659-6666.
27. Jain T., Jayaram, B. A computational protocol for predicting the binding affinities of zinc containing metalloprotein-ligand complexes, *PROTEINS: Struct. Funct. Bioinfo.*, 2007, 67, 1167-1178.
28. Shaikh SA, Ahmed SR, Jayaram B. A molecular thermodynamic view of DNA-drug interaction: A case study of 25 minor groove binders. *Arch Biochem Biophys.*, 2004, 429, 81-99.
29. Shaikh SA, Jayaram B. A Swift All-Atom Energy-Based Computational Protocol to Predict DNA-Ligand Binding Affinity and Tm. *J Med Chem.*, 2007, 50, 2240-4.
30. Jayaram B, Latha N, Jain T, Sharma P, Gandhimathi A, Pandey VS. Sanjeevini: A comprehensive active site directed lead design software. *Indian J Chem A*, 2006, 45, 1834-37.
31. Jayaram B, Singh T, Mukherjee G, Mathur A, Shekhar S, and Shekhar V. Sanjeevini: A freely accessible web-server for target directed lead molecule discovery. *BMC Bioinformatics* 2012; 13, S7. doi:10.1186/1471-2105-13-S17-S7
32. Kalra P, Reddy TV, Jayaram B. Free Energy Component Analysis for Drug Design: A Case Study of HIV-1 Protease. Inhibitor Binding. *J Med Chem.*, 2001, 44, 4325-38.
33. Mukherjee G, Patra N, Barua P, Jayaram B. A Fast Empirical GAFF Compatible Partial Atomic Charge Assignment Scheme for Modeling Interactions of Small Molecules with Biomolecular Targets. *J Comput Chem.*, 2011, 3, 893-907.
34. Soni, A., Pandey, KM, Ray, P., Jayaram, B. Genomes to Hits in Silico - A Country Path Today, A Highway Tomorrow: A Case Study of Chikungunya, *Curr. Pharma. Des.*, 2013, 19, 4687-4700 .



Mr. Shashank Shekhar is Director and one of the founding partners of Novo Informatics Pvt. Ltd. He also holds a position of Project Scientist at SCFBio, IIT Delhi for the last seven years. His domain expertise is in the area of High Performance Computing (HPC) for Bioinformatics and Computational Biology along with the development of the Software's and Computational Packages in this field. He has also co-authored many research papers published in the facility during his stint in the lab. Mr. Shekhar has a vast experience in handling the Bioinformatics projects and is involved in various activities in the area of Genomics, Proteomics, Drug Designing and HPC which have taken place in the facility for the last several years. He was also associated with a Grid Computing Project with CBRC, Tokyo (JAPAN), which was an initiative of an Indo-Japan (DST-JST) Collaborative Project. He is one of the core members of the SCFBio's team who has worked in the area for achieving the dream (Gene to Drug) of SCFBio.

At NI, his role is primarily involved in guiding and driving the R&D team to focus in the core technical area for developing novel technologies and also to do all the Insilico related activities which will help the company to achieve and deliver the consultancy/products to the clients.



Prof. Jayaram obtained his Ph.D from City Univ. of New York, USA, followed by Post Doctoral work (1987-88), at the Columbia University, USA and Senior Research Associate (1989-90) in the Wesleyan University, USA. He is currently a Professor of Chemistry, IIT Delhi and Coordinator of Kusuma School of Biological Sciences and Supercomputing Facility for Bioinformatics & Computational Biology, IIT Delhi. He is the recipient of Chemical Research Society of India Medal. He is the member of many national and international committees; National Task Force on Bioinformatics of Department of Biotechnology (DBT), Physical Chemistry Programme Advisory Committee of the Department of Science & Technology (DST), Organic Chemistry Programme Advisory Committee of the DST, working Group on Bioinformatics of Department of Information Technology, Vice President of Indian Biophysical Society, member of FIST Committee of DST for Chemical Sciences, National Committee of IUPAB, Bioinformatics Task Force of Indian Council of Medical Research, Chairman, DBT's committee on promotion and popularization of Biotechnology, Biophysics, Biochemistry & Molecular Biology Programme Advisory Committee of the DST. He has also served as a member of the editorial board of *Journal of Molecular Graphics & Modeling*. He is responsible for projects like developing Chemgenome, Bhageerath & Sanjeevini methods & softwares for genome annotation, protein tertiary structure prediction & computer aided drug design respectively, for setting up a multi-teraflop supercomputing facility for Bioinformatics & Computational Biology at IIT Delhi, and for making the hardware and software freely accessible at (www.scfbio-iitd.res.in) to the global scientific user community. Prof. Jayaram is faculty facilitator/Founder Director for two start-up companies (Leadinvent incubated at IIT, Delhi from 2006-2009 & Novoinformatics, under incubation at IIT Delhi since 2011). He has guided several PhDs (10 completed, 7 in progress); published and presented over 100 papers in national/international journals & conferences. Currently his research interest comprises of Genome Analysis, Protein Structure Prediction and Drug Design.

Mapping the Non-equilibrium processes in Multi-dimensional space onto one dimensional : A Projection Operator Formulation

Aniket Patra[#], Alok Samanta^{*}

[#]Department of Physics and Astronomy Rutgers, The State University of New Jersey, 136 Frelinghuysen Road Piscataway, NJ 08854-8019 USA [#]Email: apatra@physics.rutgers.edu

^{*}Theoretical Chemistry Section, Bhabha Atomic Research Centre, Mumbai-400085, India ^{*}Email:alok@barc.gov.in

The present paper discusses the derivation of a generalized kinetic equation (GKE) for the time evolution of the probability distribution for general microscopic coordinates based on projection operator formalism. To make the equation tractable we have adopted two well known standard approximations, which reduce the exact equation into a Smoluchowski type equation. The new kinetic equation is able to describe the dynamics beyond linear response regime. As illustrative examples, we consider electron transfer reaction and energy diffusion processes under over damped situation. The kinetic equations corresponding to these non equilibrium processes which lie in Multi-dimensional Liouville Space become one dimensional in reaction co-ordinate or phase function space.

1. Introduction

We know that equilibrium statistical mechanics was built on a general and systematic approach, namely the Boltzmann-Gibbs distribution to evaluate the molecular properties at the macroscopic level. However, no such general and simple approach was available based on first principle theory for describing the dynamics of non-equilibrium processes. When the system is close to equilibrium, we are able to describe the relaxation of non equilibrium processes based on linear response theory. The linear response approximation predicts identical time evolution of relaxation from all non equilibrium initial configurations that relax to the same equilibrium state. If the system is created far away from the equilibrium, linear response theory (LRT) breaks down then the LRT prediction fail to describe the time evolution of relaxation pathways. In the case of complex dynamical processes associated with chemical reaction, where the system is prepared in non equilibrium state, diffusion of different kinds of mode that brings the system into the state of critical configuration. Once this critical configuration is reached then reaction does takes place with unit or finite probability. Conventional theory based approaches to describe the dynamics for such extreme non equilibrium cases is severely hindered due to multi-dimensional nature of the dynamical processes. Reduction methods in chemical kinetics are designed to locate the lower dimensional manifolds to achieve a systematic decrease in the size and complexity of the system. Several studies have been concerned with obtaining the transport equations that govern the time evolution of a many body system starting from first principles. Among them, the most important ones are the works of Zwanzig [1] and Mori[2] which made

use of the projection operator technique, first introduced by Zwanzig. In subsequent developments, Garcia-Colin and Rio [3][4] have proposed a unified method for deriving the exact kinetic equations governing the time evolution of the dynamical quantities of many-body systems. Although the exact generalized kinetic equation is used for extracting applications, and most of them have been concerned with physical processes, an attempt has been made recently by us [5] to derive the generalized kinetic equation based on projection operator technique for describing reactions dynamics in solution.

II. Theoretical Formalism

The modified Liouville equation [5] for the reactive system can be written as

$$\frac{\partial \rho(\Gamma, t)}{\partial t} = -[iL + k\delta(A(\Gamma) - a^*)]\rho(\Gamma, t) \quad (1)$$

where 'L' and k represent respectively the Liouville operator and sink strength. Here $\rho(\Gamma, t)$ is the probability density defined in Γ space at time 't'. The kinetic equation for the nonreactive system corresponds to the Eq.(1) with $k = 0$. The formal solution of Eq. (1) can be written as

$$\rho(\Gamma, t) = e^{-i\tilde{L}t} \rho(\Gamma, 0), \quad (2)$$

where $\tilde{L} = L - ik\delta(A(\Gamma) - a^*)$ and $\rho(\Gamma, 0)$ is the initial constrained probability distribution. The average value $\alpha(t)$ of the phase space function $A(\Gamma)$ is defined as

$$\alpha(t) = \int d\Gamma \rho(\Gamma, t) A(\Gamma). \quad (3)$$

Thus, if one knows the time evolution of $\rho(\Gamma, t)$, one can in principle, find $\alpha(t)$. Alternatively one can evaluate $\alpha(t)$ using the following equation

$$\alpha(t) = \int d\Gamma \rho(\Gamma, 0) A(\Gamma, t), \quad (4)$$

where $A(\Gamma, t) = e^{i\tilde{L}t} A(\Gamma, 0)$ and $\tilde{L}^\dagger = L + ik\delta(A(\Gamma) - a^*)$ with \tilde{L}^\dagger as the Hermitian adjoint of \tilde{L} . One of the most important quantities is $p(t)$, which represents the probability of finding the system in the reactant well at time t and is defined as

$$p(t) = \int d\Gamma \rho(\Gamma, t). \quad (5)$$

Here the reaction takes place when $A(\Gamma)$ reaches a critical value a^* and hence it is convenient to find out the distribution $g(a, t)$ of the phase space function $A(\Gamma)$ to have the numerical value a at time t , which is defined as

$$g(a, t) = \int d\Gamma \rho(\Gamma, t) \delta(A(\Gamma) - a), \quad (6)$$

where $G(a, 0) = \delta(A(\Gamma) - a)$. Alternatively, one can define the same quantity as

$$g(a, t) = \int d\Gamma \rho(\Gamma, 0) G(a, t), \quad (7)$$

where $G(a, t) = e^{i\tilde{L}t} G(a, 0)$. Now $p(t)$ can be written in terms of $g(a, t)$ as

$$p(t) = \int da g(a, t). \quad (8)$$

It is clear from Eq. (5) that it involves a multi-dimensional integral, whereas Eq.(8) contains only a one-dimensional integral, leading to much simplification. Thus it is interesting to obtain a kinetic equation for $g(a, t)$. In order to obtain, the generalised kinetic equation for $g(a, t)$ we define the generalised projection operator as defined by Garcia Colin et al [3], which projects a phase space function belonging to $H_g(\omega/\Gamma)$ onto the Hilbert space spanned by $G(b, 0)$ (with $b \in \square$). The latter space is defined as $H_G(\omega/\Gamma)$ and the projection operator is written as

$$P_G \equiv \int db \frac{(\dots, G(b, 0))}{[G(b, 0)]} G(b, 0), \quad (9)$$

where $[G(b, 0)] = \int d\Gamma \omega(\Gamma) G(b, 0)$ and $L\omega(\Gamma) = 0$. Using the following properties

$$(G(a, 0), G(b, 0)) = [G(b, 0)] \delta(a - b) \quad (10)$$

$$P_G^2 = P_G \quad (11)$$

$$P_G G(a, 0) = G(a, 0) \quad (12)$$

$$(A, P_G B) = (P_G A, B). \quad (13)$$

and after some lengthy algebra we arrive at the kinetic equation $g(a, t)$ defined as

$$\frac{\partial g(a, t)}{\partial t} = \int_0^t d\tau \int da \frac{\partial}{\partial a} K(a, a', \tau) V_{eff}(a) \left[\frac{\partial P(a', t a_0, 0)}{V_{eff}(a')} \right] - k\delta(a - a') g(a, t) \quad 14$$

where the memory kernel $K(a, a', t)$ is defined as

$$K(a, a', s) = \frac{(F(a, s), F(a', 0))}{[G(a', 0)]} \quad (15)$$

where $F(c, t) \equiv U(t) \{(1 - P_G) i L G(c, 0)\}$

$$\text{and } U(t) = \exp[(1 - P_G) i L t].$$

Since there is no other variables except ' a ' appears in the kinetic equation defined in Eq.14, so it is an exact equation for the probability distribution in coarse grained ' a ' space that is the reaction coordinate space. In case of non-reactive system ($k = 0$), the second term in the right hand side vanishes identically and we get back the kinetic equation derived by Zwanzig. It is extremely difficult to evaluate the memory kernel $K(a, a', t)$ due to the appearance of the projection operator P_G in the expression of the memory kernel. However the exact generalized kinetic equation can be simplified if the Phase space function $A(\Gamma)$ is symmetric with respect to time inversion and the quantity $\frac{\partial A(\Gamma)}{\partial t}$ is a slowly varying function of time. One thus obtains the simplified equation

$$\frac{\partial g(a, t)}{\partial t} = \frac{\partial}{\partial a} \left[D(a) \frac{\partial P(a, t a_0, 0)}{\partial a} + \frac{\partial \{\beta V_{eff}(a)\}}{\partial a} P(a, t a_0, 0) \right] - k\delta(a - a') g(a, t) \quad 16$$

where

$$D(a) = \int_0^\infty dt \frac{\left\langle \frac{dA(\Gamma, t)}{dt} \left(\frac{dA(\Gamma, t)}{dt} \right)_{t=0} \delta(A(\Gamma, t) - a) \right\rangle}{\langle \delta(A(\Gamma) - a) \rangle} \quad 17$$

$$V_{eff}(a) = \frac{1}{\beta} \ln \langle \delta(A(\Gamma) - a) \rangle \quad (18)$$

This one dimensional equation forms the basis for a unified description of a wide variety of dynamical processes in condensed phase with proper selection of the phase space function $A(\Gamma, t)$

III. Electron-Transfer Reaction: Initial Non-equilibrium State

Electron transfer (ET) reactions in condensed phase have been one of the most thoroughly investigated processes over several decades [6-11]. Recent years have witnessed an upsurge of experimental investigations on ET processes due to wide availability of spectroscopic techniques for dynamical measurements and the synthesis of tailor-made artificial electron donor-acceptor systems which have led to a wealth of new experimental results. In this case of photo chemical electron transfer reaction,

D-A pair embedded in solvent environment shine with an ultra-short laser pulse; electronic excitation of DA pair, leading to the formation of the ion-pair D^+A^- . Thus, the solvent molecules surrounding the ion-pair are completely non-equilibrium configuration and then the system relaxes downwards along the potential energy surface (corresponding D^+A^- pair in solvent molecules) due to the relaxation of the surrounding polar solvent till it meets the potential energy surface of the molecule DA, at which the configuration of the solute and solvent molecules becomes critical i.e. Γ^* , and the back ET takes place at Γ^* with an intrinsic rate constant k . In order to solve the kinetic equation, what is needed the microscopic expression for $A(\Gamma)$ and initial distribution function $g(a, 0)$ in 'a' space. In the following section, we discuss the selection of $A(\Gamma)$

A. Electron Transfer Reaction: Selection of Phase Function $A(\Gamma)$

The electron, which is originally localized at the donor site in the reactant, will be delocalized when the following condition is satisfied [6]

$$V^R(\Gamma^*) = V^P(\Gamma^*) \quad (19)$$

where $V^R(\Gamma)$ and $V^P(\Gamma)$ respectively represent potential energy for reactant and product and Γ^* represents the critical configuration for ET reaction. System can attain this critical configuration Γ^* during its journey from initially prepared Non-equilibrium state or equilibrium state. Therefore, in the case of ET $A(\Gamma) = V^R(\Gamma) - V^P(\Gamma)$ and $a^* = 0$

B. Photo Excitation: Initial Distribution Function $g(a, 0)$ in 'a' space

In the case of photo excitation, the excited electronic state of D-A pair in solvent molecules is created by the absorption of visible radiation with frequency ω . Due to thermal fluctuation, initially the phase space coordinates Γ of the D-A-solvent system are unknown, what is known is their probability distribution $\exp[-\beta H^r[\Gamma]]$, where $H^r[\Gamma]$ corresponds the total Hamiltonian of the reactant in solvent molecules. Therefore, each repetitions of the experiment with identical macroscopic condition i.e. $A(\Gamma, 0) = \hbar\omega = a_0$ different kinds of phase space coordinates are sampled. Before absorption of photon, the system was in thermal equilibrium with distribution function $\exp[-\beta H^r[\Gamma]]$, the initial constraint equilibrium distribution function corresponding to the excited state in Γ space is given by

$$\rho(\Gamma, 0) = \frac{\delta(A(\Gamma, 0) - \hbar\omega) \exp[-\beta H^r[\Gamma]]}{\int d\Gamma \delta(A(\Gamma, 0) - \hbar\omega) \exp[-\beta H^r[\Gamma]]} \quad (20)$$

Now, combining Eq. (6) and Eq. (20), we obtain the initial probability distribution $g(a, 0)$ in 'a' space as

$$g(a, 0) = \int d\Gamma \delta(A(\Gamma, 0) - a) \frac{\delta(A(\Gamma, 0) - \hbar\omega) \exp[-\beta H^r[\Gamma]]}{\int d\Gamma \delta(A(\Gamma, 0) - \hbar\omega) \exp[-\beta H^r[\Gamma]]} = \delta(a - \hbar\omega). \quad (21)$$

IV. Energy Diffusion Equation for Brownian Particle

The escape of particle from a well in the presence of a thermal bath one needs to look at two limiting cases, the over damped limit where the friction is very large and the rate limiting process is spatial diffusion across the barrier top. In the under damped limit, friction is very small and the probability that a particle will gain energy much greater than β is small. So overall rate of diffusion is controlled by energy diffusion processes. The phase function corresponding to the energy diffusion equation is $A(\Gamma) = H^r[\Gamma]$. The kinetic Equation for energy diffusion equation can be written as

$$\frac{\partial g(E, t)}{\partial t} = \frac{\partial}{\partial E} \left[D(E) \frac{\partial g(E, t)}{\partial E} + \frac{\partial \{ \beta V_{eff}(E) \}}{\partial E} g(E, t) \right] \quad (22)$$

Here $g(E, t)$ represents the probability of finding the particle having energy E at time t and $V_{eff}(E)$ corresponds to the effective potential in energy space. Here $D(E)$ represents energy dependent diffusivity.

V. Functional Smoluchowski Equation

We first write the distribution of the microscopic operator $A(\Gamma)$ in the following form

$$\delta(A(X), -\rho) = \prod_{\alpha} \delta(\hat{\rho}(r_{\alpha}) - \rho(r_{\alpha})) \quad (23)$$

where $\hat{\rho}(r_{\alpha})$ and $\rho(r_{\alpha})$ represent respectively microscopic and coarse-grained particle number densities. Now using the transformation

$$\sum_{\alpha} \frac{\partial}{\partial \rho(r_{\alpha})} \rightarrow \int dr \frac{\partial}{\partial \rho(r)} \quad (24)$$

and after some algebra, we obtain functional Smoluchowski equation defined as

$$\frac{\partial g[\rho(r), t]}{\partial t} = D \int dr \frac{\partial}{\partial \rho(r)} \left[\frac{\partial g[\rho(r), t]}{\partial \rho(r)} + \frac{\partial \beta F[\rho(r)]}{\partial \rho(r)} g[\rho(r), t] \right] \quad (25)$$



Here $g[\rho(r), t]$ represents the probability of finding the density profile $\rho(r)$ at time t and $F[\rho(r)]$ corresponds to free energy functional.

VI. Conclusion

It is shown here that a proper selection of phase function $A(\Gamma)$, a generalized unified kinetic equation for its probability distribution is derived for describing a wide class of dynamical phenomena in condensed phase. The corresponding full Liouville space description is much more complicated and also difficult to visualize. On using two successive approximations, we further simplify the kinetic equation to obtain a Smoluchowski type tractable equation with a sink of strength k in 'a' space. As illustrative examples, we here consider e.g. electron transfer, energy diffusion and derive corresponding kinetic equation. Functional Smoluchowski is also derived based on GKE.

References:

1. R. Zwanzig, Phys. Rev. 124 (1961) 983 .
2. H. Mori, H. Fujisaka, and H. Shigematsu, Prog. Theor. Phys. 51 (1974) 109 .
3. L. S. Garcia-Colin and J.L. del Rio, J Stat Phys, 16 (1977) 235 .
4. L. S. Garcia-Colin and J. L. del Rio, J Stat Phys, 19 (1978) 109 .
5. A. Patra, A. K. Samanta and S. K. Ghosh, Phys. Rev. E 83 (2011) 026104.
6. (a) R. A. Marcus, J. Chem. Phys. 24 (1956) 979; (b) R. A. Marcus, Annu. Rev. Phys. Chem. 15 (1964) 155 .
7. (a) D. F.Calef and P.G. Wolynes, J. Phys. Chem. 87 (1983) 3387; (b) D. F.Calef and P.G. Wolynes, J.Chem. Phys. 78 (1983) 470 .
8. A. Yoshimori, T. Kakitani, Y. Enomoto and N. Mataga, J. Phys. Chem. 93 (1989) 8316 .
9. K.Dhole, B.Modak, A.Samanta, S. K. Ghosh, Phys Rev E. 82 (2010) 016110 .
10. K.Dhole, A.Samanta, S. K. Ghosh, J. Phys. Chem A, 112 (2008) 4879 .
11. Scott H. Northrup, and J. T. Hynes, Chem. Phys. Lett, 54 (1978) 244.

	<p><i>Dr. Alok k. Samanta is a Scientific Officer in Theoretical Chemistry Section of Bhabha Atomic Research Centre, Mumbai. After completion of M.Sc. from I.I.T , Kharagpur , He joined BARC through the 30th batch of Training School. He obtained doctoral degree from University of Mumbai and his research interests are Time dependent density functional theory for Quantum and Classical Systems; Dynamics of many particle system in condensed phases; Mode-coupling Theory and Number Theory.</i></p>
	<p><i>Aniket Patra, completed Integrated B.S.-M.S. (Majoring in Physics) from Indian Institute of Science Education and Research (IISER)-Kolkata. He is now graduate student (physics) of the university of Rutgers, USA. His current research interests are non-equilibrium statistical mechanics, phase transition, theoretical condensed matter physics (especially many body theory of strongly correlated systems), atomic and molecular physics, intense laser atom interaction and non-linear optics.</i></p>

Achievements, Honours and Awards received by the SMC members

Name of the member and affiliation	Name of the Honour/ Award	Conferred by
Dr Anjali M. Rahatgaonkar , Associate Professor, Chemistry, Institute of Science, Nagpur	Fellow of the Royal Society of Chemistry, London (FRSC).	Royal Society of Chemistry, (RSC) London.
Dr. A. K. Tyagi Chemistry Division, BARC, Mumbai	ISCB Award for excellence in Chemical Sciences (2013)	Indian Society of Chemists and Biologists (ISCB)
Prof. Anshu Dandia Department of Chemistry, University of Rajasthan, Jaipur)	Best Chemistry Teacher in India award	CII Global Higher Education Summit
Dr. Bhavana Gupta , Indira Gandhi Center for Atomic Research	Inspire Faculty Fellow	Department of Science and Technology.
Dr. Dilip Kumar Mishra Department of Physics, Institute of Technical Education and Research,	Young scientist award	Orissa Bigyan Academy (Science & Technology Department, Government of Odisha), Odisha
Prof. G.P. Das , Dept. of Materials Science, IACS, Kolkata	ACCMS Award 2013	Asian Consortium on Computational Materials Science
Dr. G. M. Malik S. G. University Surat	Fellowship of Institution Of Chemists, Kolkata.	INSTITUTION OF CHEMISTS, Kolkata.
Dr G. K. Nagaraja	Raman Post Doctoral Fellowship	UGC
Kalpana Nagle Assistant professor Gurunanak College of Engineering Dahegaon, Nagpur	Women scientist award (WOS- A)	DST New Delhi
Lagnamayee Mohapatra IMMT, Bhubaneswar, Odisha,India.	DST-DFG Awards for Participation in the Meeting of Nobel Laureates & Student	DST & German Research Foundation.
Dr. P. Sujatha Devi , Principal Scientist, CSIR-CGCRI	Fellow of the West Bengal Academy of Science and Technology (WAST).	West Bengal Academy of Science and Technology (WAST).
P.V. Ananthapadmanabhan Laser & Plasma Technology Division, BARC	Homi Bhabha Science & Technology Award (2011)	Department of Atomic Energy, Government of India
Dr. Rubel Chakravarty Scientific Officer – E, Isotope Applications and Radiopharmaceuticals Division, BARC	Young Scientist Award in Chemical Sciences for 2012-13	The Indian Science Congress Association
Dr. Rubel Chakravarty Scientific Officer – E, Isotope Applications and Radiopharmaceuticals Division, BARC	Fulbright-Nehru Postdoctoral Research Fellowship for 2013-14	J. William Fulbright Foreign Scholarship Board, United States
Dr. Sanjeev Kumar Gupta , Dept. of Physics, M. K. Bhavnagar University, Bhavnagar-364001, Gujarat	Fulbright Post-Doctoral Scholar	J. William Fulbright Foreign Scholarship Board, United States
Dr. Vinod Kumar Tiwari Assistant Professor, Department of Chemistry Banaras Hindu University Varanasi-221005	1. Young Scientist Award-2012 2. Dr. H C Srivastava Award-2012, 3. Dr. Ghanashyam Srivastava Memorial Medal-2012,	1. Chemical Research Society of India (CRSI), 2. Association of Carbohydrate Chemist & Technologist. 3. Indian Chemical Society.

Forthcoming News and Events

1. 9th International Conference on Novel Materials and their Synthesis (NMS-VIII) & 23rd International Symposium on Fine Chemistry and Functional Polymers (FCFP-XXIII) is to be held in Shanghai from 17 to 22 October, 2013 (www.nms-iupac.org).
2. Symposium OO: Solid-State Chemistry of Inorganic Materials, 2013 MRS Fall Meeting & Exhibit December 1-6, 2013, Boston, Massachusetts.
3. 11th International Conference on Solid State Chemistry, July 06 - July 11 2014 Location: Trencianske Teplice, Slovakia Website: <http://www.ssc2014.sav.sk>
4. International Conference on Applied Chemistry 2014, March 05-March 07, 2014. Location: Suva Fiji Website: <http://www.fnu.ac.fj/newsite/images/stories/conference/index.html>
5. XXVth IUPAC Symposium on Photochemistry July 13- July 18 2014. Location: Bordeaux, France, Website: <http://www.photoiupac2014.fr>
6. DAE-BRNS, 2nd National Workshop on Materials Chemistry, NWMC-2013 (CAT-MAT), to be held at BARC, during 22-23 November, 2013.

Printed by:

Ebenezer Printing House

Unit No. 5 & 11, 2nd Floor, Hind Service Industries

Veer Savarkar Marg, Shivaji Park Sea-Face, Dadar (W), Mumbai - 400 028

Tel.: 2446 2632 / 2446 3872 Tel Fax: 2444 9765 E-mail: outworkeph@gmail.com

In this issue

Feature articles	Page No.
1. Organic Molecules Adsorption on Single Layer MoS₂: A Theoretical Study <i>Arkamita Bandyopadhyay and Swapan K Pati</i>	1
2. A theoretical account of the photodetachment spectroscopy of anionic boron clusters <i>S. Rajagopala Reddy and S. Mahapatra</i>	5
3. Methanol in its normal liquid and supercritical states: Changes of polarity and hydrogen bonding from firstprinciples simulations <i>Vivek Kumar Yadav and Amalendu Chandra</i>	15
4. Ab initio Molecular Dynamics and DFT studies on (HF)_n [n= 2 - 10] clusters <i>Sukanta Mondal, Sudip Pan and Pratim Kumar Chattaraj</i>	19
5. First-Principles Studies of Phase Stability and Phase Transforma- tions in Alloys <i>Ashok K. Arya</i>	26
6. Genome to Drug Software Initiatives <i>Shashank Shekhar, B. Jayaram</i>	35
7. Mapping the Non-equilibrium processes in Multi-dimensional space onto one dimensional : A Projection Operator Formulation <i>Aniket Patra and Alok Samanta</i>	44
Honours and Awards	48

Published by

Society for Materials Chemistry

C/o. Chemistry Division Bhabha Atomic Research Centre, Trombay, Mumbai, 400 085 (India)

E-mail: socmatchem@gmail.com,

Tel: +91-22-25592001